INFORMATION TO USERS

This was produced from a copy of a document sent to us for microfilming. While the most advanced technological means to photograph and reproduce this document have been used, the quality is heavily dependent upon the quality of the material submitted.

The following explanation of techniques is provided to help you understand markings or notations which may appear on this reproduction.

1. The sign or "target" for pages apparently lacking from the document photographed is "Missing Page(s)". If it was possible to obtain the missing page(s) or section, they are spliced into the film along with adjacent pages. This may have necessitated cutting through an image and duplicating adjacent pages to assure you of complete continuity.

2. When an image on the film is obliterated with a round black mark it is an indication that the film inspector noticed either blurred copy because of movement during exposure, or duplicate copy. Unless we meant to delete copyrighted materials that should not have been filmed, you will find a good image of the page in the adjacent frame.

3. When a map, drawing or chart, etc., is part of the material being photographed the photographer has followed a definite method in "sectioning" the material. It is customary to begin filming at the upper left hand corner of a large sheet and to continue from left to right in equal sections with small overlaps. If necessary, sectioning is continued again—beginning below the first row and continuing on until complete.

4. For any illustrations that cannot be reproduced satisfactorily by xerography, photographic prints can be purchased at additional cost and tipped into your xerographic copy. Requests can be made to our Dissertations Customer Services Department.

5. Some pages in any document may have indistinct print. In all cases we have filmed the best available copy.

University
Microfilms
International

300 N. ZEEB ROAD, ANN ARBOR, MI 48106
18 BEDFORD ROW, LONDON WC1R 4EJ, ENGLAND

WONICA, DENNIS

BRILLOUIN SCATTERING IN XENON NEAR THE CRITICAL POINT

City University of New York PH.D. 1979

BRILLOUIN SCATTERING IN XENON NEAR THE CRITICAL POINT

by

DENNIS WONICA

A dissertation submitted to the Graduate Faculty in Physics in partial fulfillment of the requirements for the degree of Doctor of Philosophy, The City University of New York.

1979

This manuscript has been read and accepted for the Graduate Faculty in Physics in satisfaction of the dissertation requirement for the degree of Doctor of Philosophy.

5/24/79
date

Harry L. Swinney
Chairman of Examining Committee

7/30/79
date

Frank Martino (RC)
Executive Officer

Klaus J. Lange

Marvin H. Whittaker

Don Eden

Rodney L. Varley
Supervisory Committee

The City University of New York

FOR MOM

Abstract

BRILLOUIN SCATTERING IN XENON

NEAR THE CRITICAL POINT

BY

DENNIS WONICA

The behavior of sound in xenon was investigated along the critical isochore and for temperatures .05°-10°C above a critical temperature of 16.62°C. A laser Brillouin scattering experiment was assembled which used optical heterodyne detection combined with spectrum analysis and signal averaging. New sound velocity and sound attenuation data were obtained for frequencies in the region 1 - 15 MHz. Scattering angles were 0.36°, 0.72°, 1.44°, and 2.69°.

Electronic and optical instrumental effects were very carefully measured and deconvolved from observed spectra. A nonlinear least squares optimization algorithm was implemented using Fortran and used in a curve fitting procedure to accurately extract the Brillouin shift and Brillouin linewidth, from which the sound velocity and attenuation were determined, respectively.

The mode-mode coupling theory of Kawasaki[1], which uses a complex frequency dependent bulk viscosity, $\mathcal{Z}(\omega)$, to account for the sound dispersion and attenuation, and the theory of Mistura[2], which uses a complex frequency dependent specific heat, $\Delta(\omega)$, were examined. Both theories predict a dimensionless dispersion, D, and dimensionless attenuation, A, are given by the integral expressions, $J(\omega^*)$ and $I(\omega^*)$, respectively. $\omega^* = \omega/(2\omega_R)$, and ω_R $(=\lambda/(\rho C_p \xi^2)$, λ is the thermal conductivity, ξ the correlation length) is, from mode coupling calculations, the lowest relaxation frrquency which describes the sound mode.

In contrast to most previous analyses, an absolute comparison of data with theory was made: no thermodynamic parameters were adjusted. J and I were computed to lowest order, for a background λ of zero, and for three density correlation functions: Ornstein-Zernike, Fisher-Burford, and the Fourier transform of $\exp(-r/\xi)/r^{1+\eta}$. D agreed with $J(\omega^*)$ up to $\omega^* \sim 10$, but thereafter D increased monotonically away from J being 2-3 times larger for $100 < \omega^* < 1000$. A agreed fairly well with $I(\omega^*)$ up to $\omega^* \sim 2$, then A increased markedly, being 5-10 times larger for $100 < \omega^* < 1000$. Most importantly, these results were nearly independent of the form of the correlation function.

Additionally, the ratio J/I was separately compared to the ratios $\mathrm{Im}((4/3\,\eta(\omega) + \zeta(\omega))/\rho)/\mathrm{Re}((4/3\,\eta(\omega) + \zeta(\omega))/\rho)$ and $-\mathrm{Re}(\Delta(\omega))/\mathrm{Im}(\Delta(\omega))$, as suggested by Sarid & Cannell (3). When analyzed in this manner, the data were not described by either theory over the entire range of ω^* for any form of the correlation function.

It is concluded that the Kawasaki-Mistura theory does not describe sound behavior in xenon for $\omega^* \gtrsim 10$, and the discrepancies cannot be attributed to either inaccurate knowledge of thermodyanmic quantities or departures from the Ornstein-Zernike form for the density correlation function.

1. K. Kawasaki, Phys. Rev. A 1, 1750 (1970).

2. L. Mistura, in Critical Phenomena, ed. by M. Green (Academic, New York, 1971), p. 563.

3. D. Sarid and D. Cannell, Phys. Rev. A 15, 735 (1977).

Table of Contents

List of Tables

List of Illustrations

INTRODUCTION

A primary reason for studying a critical point is the fact that it is a singularity exhibiting non-analytic mathematical behavior. As the critical temperature is approached, the singular nature manifests itself in the divergence (or convergence to zero) of the macroscopic observables, the transport and thermodynamic coefficients. These are accompanied by dramatic changes in the symmetry of the state (phase). A second motivation is the existence of cooperative effects near phase transitions. A group of atoms or molecules exhibits a collective property that is not simply the sum of the properties of the individual molecules.

The liquid-gas transition is the oldest known and most extensively studied example of a critical point. The isotropic symmetry of the fluid simplifies theoretical calculations. Theory is now highly developed and a detailed comparison with a growing body of experimental data is possible. For fluids, the cooperative effect is the space-time behavior of the density-density correlation function. Through a phenomenological argument, Ornstein and Zernike obtained a form for the long range behavior of the net correlation function in 1914. Their derivation has still not been rigorously proved, and experimental data suggest a breakdown in their results very near the critical temperature. However, there has been no experiment which definitively disproves the Ornstein-Zernike result.

The primary goal of the present work was to test the validity of the Ornstein-Zernike function through measurements

of sound propagation in a simple fluid near the critical point. It has been shown that both the sound velocity and attenuation depend on the temperature derivative of the correlation function. Thus, sound measurements provide a sensitive test of the correlation function.The detailed theories of Kawasaki and Mistura provide explicit equations relating the velocity and attenuation to integrals containg the correlation function derivative. However, auxiliary thermodynamic quantities are needed to make the detailed comparison. Thus, xenon was chosen for study since the auxiliary quantities had been measured and it is the best characterized critical fluid to date. An absolute test of theory could be performed with no parameters adjusted. Secondary goals were to obtain data complementary to exisiting ultrasonic and interferometric data by use of a light beating technique, and to search for possible differences between the Kawasaki and Mistura formalisms.

The first chapter outlines light scattering from a fluid and presents the Rayleigh-Brillouin spectrum. The sound propagation theory of Kawasaki, Mistura, and the recent renormalization group calculations are presented. The second chapter explains why ultrasonic and light scattering experiments are expected to give different results, and details the method of optical heterodyne spectroscopy used in the present work. The actual equipment used to obtain the Brillouin spectrum is described in Chapter III. The following chapter describes measurements performed to determine instrumental effects. These were carefully deconvolved from the observed spectrum. by a curve fitting procedure, which ultimately

extracted the velocity and attenuation. The numerical methods, algorithms, and their implementation are detailed in this data treatment chapter. In the last chapter, the data are compared to theory and conclusions concerning the Ornstein-Zernike function and general validity of the theory are drawn.

CHAPTER I

THEORY OF LIGHT SCATTERING FROM NORMAL & CRITICAL FLUIDS

A concise explanation of the theory relevant to scattering of light by fluids is presented. An expression for the electromagnetic field scattered by gases and liquids away from the critical point is given, then related to the optical spectrum by Fourier transformation of the scattered field correlation function. It is shown that the structure factor depends on the correlations of the particle density, which in turn are related to macroscopic observables. The density-density correlation function is obtained from classical hydrodynamics, and the features of the normal fluid spectrum are displayed.

Next, the changes in the spectrum for a fluid approaching the critical temperature are discussed. A detailed explanation of the Brillouin portion of the spectrum is given in light of the highly developed critical point theories of Kawasaki-Mistura, and the renormalization group calculations. It is shown that the experimentally measurable quantities, the sound velocity, and sound attenuation, can be compared to explicit expressions in the Kawasaki and Mistura approaches, but that the renormalization group approach cannot provide as detailed a comparison. Though Kawasaki considered complex transport coefficients and developed his theory from mode-coupling calculations, and Mistura considered a complex specific heat and energy exchanges between sound waves and density fluctuations, they

arrived at identical expressions, to lowest order.

Finally, consideration is given to the density correlation function as the critical point is approached. The influence of its long range behavior on sound propagation is discussed, from which the motivation for the present experiment follows.

A Normal Fluid

1. General Scattered Field for Dielectric

The theory of scattering from dielectrics is highly developed; only the relevant quantities necessary to describe the present experiment will be assembled here. No attempt is made to be exhaustive or complete.

Consider the electromagnetic plane wave described by,

$$\vec{E}(\vec{r},t) = \vec{E}_0 \exp\left(i(\vec{k}\cdot\vec{r} - \omega t)\right)$$

of polarization $\hat{n}$ ($\vec{E}_0 = \hat{n}E_0$), amplitude E_0, wavelength λ, frequency ω, and wavevector $\vec{k} = (\omega/c)\hat{k}$. $\hat{n}$ and $\hat{k}$ are unit vectors specifying the direction of the electric field and the direction of propagation, respectively. This wave incident on a dielectric of polarizability $\bar{\bar{\alpha}}(\vec{r},t)$ produces an oscillating dipole moment $\vec{P}(\vec{r},t) = \bar{\bar{\alpha}}(\vec{r},t)\cdot\vec{E}(\vec{r},t)$ which in turn produces at a point $\vec{r}$ the scattered field[1]:

$$d\vec{E}_s(\vec{r},t) = \left.\frac{\hat{n}_{R-r}\times(\hat{n}_{R-r}\times\ddot{\vec{P}}(\vec{r},t')\,|d\vec{r}|)}{c^2\,|R-r|}\right|_{t'=t-\frac{n|R-r|}{c}}$$

Writing the polarizability as the sum of a space-time averaged part, and a fluctuating part,

$$\bar{\bar{\alpha}}(\vec{r},t) = \langle\bar{\bar{\alpha}}\rangle + \delta\bar{\bar{\alpha}}(\vec{r},t)$$

and integrating over the illuminated volume, obtain the total

scattered field within the medium of refractive index n:

$$\vec{E}_s(\vec{R},t) = \int \frac{|d\vec{r}|\,\hat{n}_{R-r}\times(\hat{n}_{R-r}\times(\langle\bar{\bar{\alpha}}\rangle+\delta\bar{\bar{\alpha}}(\vec{r},t))\cdot\vec{E}_0)(-\omega^2)e^{i(\vec{K}\cdot\vec{r}-\omega t')}}{c^2|\vec{R}-\vec{r}|}$$

For $\vec{R}$ far from the illuminated volume,

$$|\vec{R}-\vec{r}| \approx R$$

$$\hat{n}_{R-r} \approx \hat{n}_R \equiv \hat{n}_K$$

$$\vec{K}' = \hat{n}_K(\omega m/c)$$

$$m\frac{\omega}{c}|\vec{R}-\vec{r}| \approx (\vec{R}-\vec{r})\cdot\vec{K}'$$

Therefore, the total scattered field is:

$$\vec{E}_s(\vec{R},t) = -\left(\frac{\omega}{c}\right)^2 \frac{e^{i(\vec{K}'\cdot\vec{R}-\omega t)}}{R}\,\hat{n}_K\times(\hat{n}_K\times\int_V |d\vec{r}|\,(\langle\bar{\bar{\alpha}}\rangle+\delta\bar{\bar{\alpha}}(\vec{r},t'))\cdot\vec{E}_0\,e^{i(\vec{K}'-\vec{K})\cdot\vec{r}}$$

Note that if $\delta\bar{\bar{\alpha}} = 0$, $\langle\bar{\bar{\alpha}}\rangle\cdot\vec{E}_0$ integrated over the scattering volume is zero if $V \gg \lambda^3$ except in the forward direction, $\vec{k} = \vec{k}'$. Thus, only fluctuations in the polarizability tensor give rise to scattering. For a static polarizability, $\bar{\bar{\alpha}}(\vec{r},t)$ = constant $\delta\bar{\bar{\alpha}}(\vec{r})$, the scattered field has the same time dependence as the incident field. A general scattering experiment measures the intensity, polarization, frequency, and wave vector of the scattered field. These quantities reflect the cross section, symmetry, temporal, and spatial behavior of $\bar{\bar{\alpha}}$, respectively. The scattered field then fluctuates in the same way as the fluctuating medium.

Consider now scattering by gases and liquids. The fluctuations of interest here are due solely to the translational and pure rotational degrees of freedom of the molecule. Thus, vibration-rotation, and purely vibrational

degrees of freedom are excluded, i.e. the Raman active modes. Collision induced scattering is also excluded. For fluids, this means that the phenomena are described by hydrodynamics, kinetic theory is not applicable. Thus, the region of interest is for times long compared to collision times (~ 0.1 ps) and for probe wavelengths long compared to the mean free path (this excludes essentially rarefied gases). Finally, it is assumed that the probe frequency is not coincident with electronic transitions, i.e., the medium does not absorb any radiation. The scattering of interest is referred to as Rayleigh-Brillouin scattering.

For a pure fluid having spatial isotropy, $\vec{P} = \alpha \vec{E}$. Thus, the polarizability is scalar and the induced dipole moment is always parallel to the electric field. Therefore,

$$\hat{n}_K \times (\hat{n}_K \times (\delta\bar{\alpha} \cdot \vec{E}_0)) = \hat{n}_K \times (\hat{n}_K \times \vec{E}_0)\, \delta\alpha$$

Further, $\hat{n}_K \times (\hat{n}_K \times \vec{E}_0) = \sin\phi\ \hat{n}_\phi$ where ϕ is the angle between $\hat{n}$ and $\hat{n}_K$, and $\delta\alpha = \delta\epsilon/4\pi$. ϵ is the dielectric constant. Therefore,

$$\vec{E}_s(\vec{R},t) = -\left(\frac{\omega}{c}\right)^2 e^{i(\vec{K}'\cdot\vec{R} - \omega t)} \frac{E_0 \sin\phi\ \hat{n}_\phi}{4\pi R} \int |d\vec{r}|\, \delta\epsilon\, e^{i(\vec{K}-\vec{K}')\cdot\vec{r}} \qquad 1.1$$

2 Measurable Quantities

From the scattered field expression, $\vec{E}_s$, the quantities accessible to measurement are[2]:

1.2 a	$I_S = \langle \lvert E_S \rvert^2 \rangle$	Average intensity
1.2 b	$G^{(1)}(\tau) = \langle \vec{E}_S^*(t) \cdot \vec{E}_S(t+\tau) \rangle$	field correlation function
1.2 c	$I(\omega) = \frac{1}{2\pi} \int G^{(1)}(\tau) e^{i\omega\tau} d\tau$	optical spectrum
1.2 d	$G^{(2)}(\tau) = \langle \vec{E}_S^*(t) \cdot \vec{E}_S(t) \vec{E}_S^*(t+\tau) \cdot \vec{E}_S(t+\tau) \rangle$	intensity correlation function
1.2 e	$P(\omega) = \frac{1}{2\pi} \int G^{(2)}(\tau) e^{i\omega\tau} d\tau$	power spectrum

For the present, the field correlation function will be used to determine the optical spectrum. In the following chapter, it will be shown how a power spectrum measurement can yield the optical spectrum when the scattered field is mixed with a coherent local oscillator field (heterodyne method).

The integral over the dielectric constant fluctuations may be written as

$$\delta\epsilon(\vec{q},t) = \int_V |d\vec{r}| \; e^{i(\vec{q}\cdot\vec{r})} \, \delta\epsilon(\vec{r},t)$$

where $\vec{q} = \vec{k} - \vec{k}'$ is the scattered wavevector.

The optical spectrum is, from 1.2 c:

$$I(\vec{q},\omega) = \left(\frac{E_0 \sin\phi}{4\pi R}\right)^2 \left(\frac{\omega}{c}\right)^4 \frac{1}{2\pi} \int_{-\infty}^{\infty} dt \, \langle \delta\epsilon^*(\vec{q},0) \, \delta\epsilon(\vec{q},t) \rangle \, e^{i(\omega-\omega')t}$$

or,

$$I(\vec{q},\omega) = \frac{A}{2\pi} \int_{-\infty}^{\infty} e^{-i\omega t} \langle \delta\epsilon^*(\vec{q},0) \, \delta\epsilon(\vec{q},t) \rangle \, dt \qquad 1.3$$

$$\omega' = 0, \qquad A = \left(\frac{E_0 \sin\phi \, K_s^2}{4\pi R}\right)^2$$

Now the dielectric constant of a pure fluid is in general a function of density and temperature, so that there exists a dielectric equation of state: $\epsilon = \epsilon(\rho, T)$, and to first order in $\delta\rho$, δT:[3]

$$\delta\epsilon(\vec{r},t) = \left(\frac{\partial\epsilon}{\partial\rho}\right)_T \delta\rho(\vec{r},t) + \left(\frac{\partial\epsilon}{\partial T}\right)_\rho \delta T(\vec{r},t) .$$

It is found experimentally that ϵ is only weakly temperature dependent, but is a strong function of density. Then the terms involving δT are neglected and,

$$I(\vec{q},\omega) = A\left(\frac{\partial\epsilon}{\partial\rho}\right)_T^2 S_{\rho\rho}(\vec{q},\omega) \qquad 1.4$$

where

$$S_{\rho\rho}(\vec{q},\omega) = \frac{1}{2\pi}\iint e^{i(\vec{q}\cdot\vec{r}-\omega\tau)}\langle\delta\rho^*(0,0)\,\delta\rho(\vec{r},\tau)\rangle\,|d\vec{r}|\,d\tau \qquad 1.5$$

is the structure factor or dynamic form factor.[4]

From the definition of the Van Hove correlation function,[5] $G(\vec{r},\tau)$:

$$G(\vec{r},t) = \langle\rho(\vec{0},0)\,\rho(\vec{r},\tau)\rangle/\rho$$

$$S(\vec{q},\omega) = \frac{1}{2\pi}\iint e^{i(\vec{q}\cdot\vec{r}-\omega\tau)}\left(G(\vec{r},\tau)-\rho\right)|d\vec{r}|\,d\tau$$

The total intensity is obtained by integrating over ω:

$$I_s(\vec{q}) = A\,S(\vec{q})\left(\frac{\partial\epsilon}{\partial\rho}\right)_T^2$$

$$S(\vec{q}) = 1+\rho\int|d\vec{r}|\,e^{i\vec{q}\cdot\vec{r}}\left(g(r)-1\right)$$

and g(r) is the radial distribution function.[6] g(r) is related to $G(\vec{r},\tau)$ by:[7]

$$G(\vec{r},0) = \delta(\vec{r}) + \rho\,g(\vec{r})$$

For normal fluids, g(r) is short ranged, perhaps 10 or 20 Å, so that if visible light is used as the probe,

$\exp(i\vec{q}.\vec{r}) = 1$ and

$$S(\vec{q}) = 1 + \rho \int |d\vec{r}| \, (g(r) - 1) = \rho k_B T K_T \qquad 1.6$$

from the compressibility theorem [8] (note that from translational invariance, the vector dependence of g may be dropped).

To proceed further, the density-density correlation function must be calculated, and this depends on the particular system investigated and particular model used. There are three means of obtaining correlation functions: use of Onsager's hypothesis[9], the generalized linear response theory of Zwanzig[10][12], or Mori's generalized Langevin equation[11]. In the next section use of Onsager's hypothesis will be used to obtain the linearized hydrodynamic equations from which the density-density correlation function is obtained.

3 Density-Density Correlation Function from Hydrodynamics

One procedure used to derive $S_{\rho\rho}(\vec{q},\omega)$ for a simple, pure fluid is outlined here. It follows the concise, complete treatment of Berne & Pecora[13]. Starting with the relevant conservation equations, and adding the constitutive relations, the basic fluid dynamic equations are derived. Then, Onsager's hypothesis applied to these relaxation equations enables the calculation of correlation functions. Onsager's hypothesis states that spontaneous fluctuations in some macroscopic observable regress to equilibrium according to the same equation that describes the

macroscopic variable in its equilibrium state. Assuming small fluctuations in the thermodynamic variables for the fluid, linearized equations of fluid dynamics are derived. The hydrodynamic approach was first described by Landau & Placzek[14] and then developed by Mountain [15]. Modern theoretical treatments are given by Lallemand[16], using the generalized Langevin equation, and Pike[17], using many body theory and thermodynamic Green's functions.

The variables of fluid menchanics are the conserved densities: number density $\rho(\vec{r},t)$, momentum density $\vec{g}(\vec{r},t)$, and energy density $e(\vec{r},t)$. The conservation equations are the following continuity equations:

$$\frac{\partial \rho(\vec{r},t)}{\partial t} + \vec{\nabla}\cdot\vec{J}(\vec{r},t) = 0$$

$$\frac{\partial \vec{g}(\vec{r},t)}{\partial t} + \vec{\nabla}\cdot\overline{\overline{\tau}}(\vec{r},t) = 0$$

$$\frac{\partial e(\vec{r},t)}{\partial t} + \vec{\nabla}\cdot\vec{J}_e(\vec{r},t) = 0$$

The constitutive relations are:

$$\vec{J}(\vec{r},t) = \rho(\vec{r},t)\,\vec{u}(\vec{r},t)$$

$$\tau_{ij} = m\rho u_i u_j + P\delta_{ij} - \eta(\nabla_i u_j + \nabla_j u_i - \tfrac{2}{3}\vec{\nabla}\cdot\vec{u}\,\delta_{ij}) - \zeta\vec{\nabla}\cdot\vec{u}\,\delta_{ij}$$

$$\vec{J}_e(\vec{r},t) = (\tfrac{1}{2}m\rho u^2 + e')\vec{u} + \vec{u}\cdot\vec{\sigma} - \lambda\vec{\nabla}T$$

$e'(\vec{r},t)$ = local internal energy density

$$\sigma_{ij} = -P\delta_{ij} + \sigma'_{ij}$$

$$\sigma'_{ij} = \eta(\nabla_i u_j + \nabla_j u_i - \tfrac{2}{3}\vec{\nabla}\cdot\vec{u}\,\delta_{ij}) + \zeta\vec{\nabla}\cdot\vec{u}\,\delta_{ij}$$

$\vec{u}(\vec{r},t)$ = velocity $\quad \zeta$ = bulk viscosity $\quad \eta$ = shear viscosity $\quad m$ = mass per particle

There are five nonlinear partial differential equations in the seven unknowns, $(\rho, \vec{g}, e, P, T)$. Expressing two of

(ρ, e, P, T) in terms of the remaining two closes the equations, under the assumption of local thermodynamic equilibrium, and using the equations of state. Because the fluctuations about equilibrium are small, a linear expansion,

$$\rho = \rho_0 + \rho_1$$
$$e = e_0 + e_1$$
$$T = T_0 + T_1$$
$$\vec{q} = \vec{q}_0 + \vec{q}_1$$

can be used to obtain the fluid dynamic equations in linearized form. These become:

$$\frac{\partial \rho_1}{\partial t} + \rho_0 \vec{\nabla} \cdot \vec{u}_1 = 0$$
$$m\rho_0 \, \partial \vec{u}_1 / \partial t = -\vec{\nabla} P_1 + \eta \nabla^2 \vec{u}_1 + (\zeta + 1/3\,\eta) \vec{\nabla} (\vec{\nabla} \cdot \vec{u})$$
$$T_0 \, \partial s_1 / \partial t = \lambda \nabla^2 T_1$$

where the energy equation was transformed to fluctuations in entropy, s_1 [13]. There are still seven variables, $(\rho_1, \vec{u}_1, P_1, T_1, S_1)$, and only five equations. Choosing number density and temperature as independent, the pressure and entropy can be eliminated (the choice (s_1, P_1) is equally valid, see e.g. Chu[18], or Benedek[1], or Landau & Lifshitz[3]). Then

$$\delta S = \left(\frac{\partial S}{\partial \rho}\right)_T \delta\rho + \left(\frac{\partial S}{\partial T}\right)_\rho \delta T = S_1$$
$$\delta P = \left(\frac{\partial P}{\partial \rho}\right)_T \delta\rho + \left(\frac{\partial P}{\partial T}\right)_\rho \delta T = P_1$$
$$\delta T = T_1$$
$$P_1 = -\frac{m\rho_0 c_v}{T_0}\left(\frac{(\gamma - 1)}{\alpha \rho_0} \rho_1 - T_1\right)$$

The final form of the linearized equations is:

$$\frac{\partial \rho_1}{\partial t} + \rho_0 \vec{\nabla} \cdot \vec{u}_1 = 0$$

$$\frac{\partial}{\partial t}\left(\vec{\nabla}\cdot\vec{u}_1\right)+\frac{V_T^2}{\rho_0}\nabla^2\rho_1+\alpha V_T^2\nabla^2 T_1-D_V\nabla^2\left(\vec{\nabla}\cdot\vec{u}_1\right)=0$$

$$\frac{\partial T_1}{\partial t}-\frac{(\gamma-1)}{\alpha\rho_0}\frac{\partial\rho_1}{\partial t}-\gamma D_T\nabla^2 T_1=0$$

where the various quantities are:

K_T = isothermal compressibility

λ = thermal conductivity

ζ = bulk viscosity

η = shear viscosity

$V_T^2=(\partial P/\partial\rho)_T$ = isothermal sound speed

$V_S^2=(\partial P/\partial\rho)_S$ = adiabatic sound speed

$\alpha=-1/\rho\,(\partial\rho/\partial T)_P$ = thermal expansivity

$\gamma=C_P/C_V$ = specific heat ratio

$D_V=(\zeta+4/3\,\eta)/(m\rho_0)$ = longitudinal Kinematic Viscosity

$D_T=\lambda/(m\rho_0 C_P)$ = thermal diffusivity

The equations in the three unknowns (ρ_1, T_1, $\vec{\nabla}\cdot\vec{u}_1$) are to be solved subject to the initial conditions: $\rho_1(\vec{r},0)$, $T_1(\vec{r},0)$, $\vec{\nabla}\cdot\vec{u}\,(\vec{r},0)$. Since this is an initial value problem, Laplace-Fourier transforms are convenient. The density-density correlation function is desired, which is found to be:

$$\frac{\langle\rho_1^*(\vec{q},0)\,\rho_1(\vec{q},t)\rangle}{\langle\rho_1^*(\vec{q},0)\,\rho_1(\vec{q},0)\rangle}=(1-1/\gamma)\,e^{-q^2D_Tt}+1/\gamma\,e^{-q^2\Gamma t}\cos\omega(q)t$$
$$+1/\gamma\,b(q)e^{-q^2\Gamma t}\sin\omega(q)t \qquad 1.7$$

$$b(q)=q(3\Gamma-D_V)/(\gamma V_S)\qquad \Gamma=1/2\left((\gamma-1)D_T+D_V\right)$$

Fourier transforming this, the structure factor is, finally:

$$S_{\rho\rho}(\vec{q},\omega) = \frac{1}{\pi} V \rho^2 k_B T K_T \left[(1 - 1/\gamma) \frac{D_T q^2}{\omega^2 + (D_T q^2)^2} \right.$$

$$+ 1/\gamma \frac{\Gamma q^2}{(\omega \pm \omega(q))^2 + (\Gamma q^2)^2}$$

$$\left. \pm \frac{1}{\gamma} b(q) \frac{\omega \pm \omega(q)}{(\omega \pm \omega(q))^2 + (\Gamma q^2)^2} \right] \qquad 1.8$$

The structure factor was derived under the assumption that the spectral widths are small compared to the frequency shifts.

There are five features to the spectrum:

- Rayleigh line, Lorentzian, unshifted, of width (HWHM) $\Gamma_R = D_T q^2$
- Brillouin doublet, Lorentzian, symmetrically shifted by $\pm\omega_B(q) = \pm v_s q$ from the Rayleigh line, and of width $\Gamma_B(q) = \frac{q^2}{2m\rho}\left[(\zeta + 4/3\,\eta) + \lambda\,(\gamma - 1)/C_p\right]$
- two peaks, non-Lorentzian, at the same shift as the Brillouin lines, which when added to them gives an asymmetric shape; b(q) usually too small to observe.

Physically, the pure fluid has five hydrodynamic modes, three longitudinal and two transverse. The transverse modes are purely diffusive and do not contribute to the light scattering spectrum. This is equivalent to assuming that there is negligible heat conduction by the fluid in the transverse direction to the sound wave propagation direction.

Of the three longitudinal modes, the Rayleigh line represents a purely diffusive mode; hence, it does not propagate. It is the decay of entropy fluctuations at constant pressure. The two Brillouin modes propagate giving rise to frequency shifts. They are the decay of pressure fluctuations at constant entropy. The interpretation follows from choosing the entropy and pressure as independent variables. The two antisymmetric components exist as a consequence of the particular model: a damped harmonic oscillator sound wave driven by thermal fluctuations.

B Critical Fluid

1 Changes in Spectrum

As stated above, the scattered field is a random variable reflecting the space-time fluctuations of the scattering medium. In particular, as the critical point is approached, the spectrum changes in accordance with the changes occurring in the thermodynamic quantities. The changes in the fluid spectrum as T_c (critical temperature) is approached are as well known as the normal fluid spectrum. Again, only a brief summary is presented here. For a complete account of general critical theory, Stanley[19] should be cited.

As $T \to T_c$, the major thermodynamic variables change with temperature along the critical isochore ($\rho = \rho_c$) as follows:[20]

$$\epsilon = (T - T_c)/T_c$$

$$K_T \sim \epsilon^{-\gamma'} \qquad \gamma' = 1.25$$
$$C_p \sim \epsilon^{-\gamma'}$$
$$C_v \sim \epsilon^{-\alpha} \qquad \alpha = 0.08$$
$$\lambda \sim \epsilon^{-\psi} \qquad \psi = 0.6$$
$$V_s \sim \epsilon^{\alpha/2}$$
$$\xi = \xi_0 \epsilon^{-\nu} \qquad \nu = 0.63$$

where ξ is the correlation length, the fundamental scale of the critical system. As $T \rightarrow T_c$, the spectrum is expected to change as follows. The Rayleigh linewidth goes to zero as $\epsilon^{(\gamma' - \psi)}$. The Brillouin shift approaches zero as $\epsilon^{\alpha/2}$, while the linewidth diverges as $\epsilon^{-(\psi - \alpha)}$. The total cross section, proportional to the compressibility, diverges as $\epsilon^{-\gamma'}$.

The xenon Rayleigh spectrum has been studied by many researchers[22] and has been reviewed extensively by Swinney[21] and Swinney & Henry[23]. Nothing further will be said about it in this investigation.

The behavior of the xenon Brillouin spectrum is the subject of this investigation. A review of all experiments to date is presented in the following chapter. For now, the formalism of the theories to account for the sound propagation is presented.

2 Brillouin Spectrum

a Kawasaki Theory

In the mode-mode coupling calculations of Kawasaki, the behavior of the sound velocity and sound attenuation is determined by an anomalous bulk viscosity. Kadanoff & Swift[24]

used mode coupling theory to determine the divergences of the transport coefficients at the transition. The heat diffusion mode (entropy fluctuation) was found to dominate the dynamics of the transition. In particular, by considering all possible couplings of the five modes, they found that, on the critical isochore, and for low values of the relaxation frequency $\omega_R (= \lambda / \rho C_p \xi^2)$, $\lambda \sim \epsilon^{2/3}$, $\eta \sim \epsilon^0$ (perhaps weakly divergent) and $\zeta \sim \epsilon^{-a}$. Building on these results, Kawasaki considered contributions to the attenuation and dispersion of a sound wave arising from the couplings of two heat modes, two sound waves, two viscous modes (shear viscosity), and a viscous mode-heat mode. The transport coefficients were all considered to be complex, frequency dependent quantities,

$$D_V(\omega) = \zeta(\omega) + 4/3\,\eta(\omega), \quad \lambda = \lambda(\omega)$$

which are related to the attenuation $\alpha(\omega)$ and dispersion $v(\omega) - v_o$ as follows:

$$\alpha_\lambda(\omega) = \alpha_\lambda^B(\omega) + \alpha_\lambda^C(\omega) \qquad 1.9\,a$$

$$\alpha_\lambda^C(\omega) = \frac{\pi \omega}{\rho V_0^2} \, Re\, \zeta^C(\omega) \qquad 1.9\,b$$

$$\alpha_\lambda^B(\omega) = \frac{\pi \omega}{\rho V_0^2} \left[4/3\,\eta + \zeta^B + \lambda \left(\frac{1}{c_V} - \frac{1}{c_p} \right) \right] \qquad 1.9\,c$$

$$\frac{V(\omega) - V_0}{V_0} = \frac{\omega}{2\rho V_0^2} \, Im\, \zeta^C(\omega) \qquad 1.9\,d$$

where v_o is the zero frequency sound velocity; the superscripts B & C refer to the background and critical parts of a quantity, respectively. He found the two heat mode contribution to the sound mode to be the dominant contribution. The results were expressed as [25]:

$$\alpha_\lambda^c(\omega) = 2\pi F(T) \int_0^\infty \frac{K_0(x)\,\omega^* x^2\,dx}{(1+x^2)^2\,(\omega^{*2} + K_0^2(x))} \qquad 1.10$$

$$\frac{V(\omega) - V_0}{V_0} = F(T) \int_0^\infty \frac{\omega^* x^2\,dx}{(1+x^2)^2\,(\omega^{*2} + K_0^2(x))} \qquad 1.11$$

$$K_0(x) = 3/4\,(1 + x^2 + (x^3 - 1/x)\,TAN^{-1}x) \qquad 1.12$$

$$F(T) = \frac{k_B T^2}{2\pi^2 \rho c_v \xi}\left(1 - \frac{c_v}{c_p}\right)\left(\frac{\partial \xi^{-1}}{\partial T}\right)_S^2 \qquad 1.13$$

$$\omega^* = \frac{\omega}{2\omega_R} \qquad \omega_R = \frac{\lambda}{\rho c_p \xi^2} \qquad 1.14$$

Note the integralsare functions only of ω^*, i.e., they are independent of q, ω, and the thermodynamic path followed, and good for any pure fluid system.

The relaxation frequency ω_R has the following physical interpretation. $1/\omega_R$ is the time necessary for heat to diffuse the distance of one correlation length. As $T \rightarrow T_c$, ξ becomes exceedingly long while the heat diffusion rate decreases. For a frequency ω, there exists a temperature where heat does not have enough time to diffuse over ξ (critical slowing down) and the entropy mode exchanges energy with the sound mode, resulting in dispersion.

The use of a complex frequency dependent bulk viscosity is not new. Compressible fluids must be described by ζ and for processes slow in restoring equilibrium (long relaxation times) ζ can become large. For sound, ζ depends

on the frequency of the sound wave i.e., there is dispersion. A discussion is found in Landau & Lifshitz[26]

b Mistura Theory

Mistura has considered a complex, frequency dependent heat capacity, $\Delta(\omega)$, to describe the energy transfer mechanism to the sound wave near T_c. Physically, the attenuation and dispersion are similar to structural relaxations. The excess specific heat is related to the sound speed by:

$$V_s^2 = V_T^2 \left(\frac{C_p + \Delta(\omega)}{C_V + \Delta(\omega)} \right) \qquad 1.15$$

The attenuation and dispersion are related to $\Delta(\omega)$ as follows:

$$\alpha_\lambda^c(\omega) = \left(\frac{C_p}{C_V} - 1 \right) \frac{\pi}{C_p} \, Im\, \Delta(\omega) \qquad 1.16\,a$$

$$\frac{V(\omega) - V_0}{V_0} = -\left(\frac{C_p}{C_V} - 1 \right) \frac{1}{2C_p} \, Re\, \Delta(\omega) \qquad 1.16\,b$$

The original Mistura derivation[27] and subsequent work by Eden, et al[28], give results identical to 1.10 and 1.11.

It should be noted that the first use of a complex, frequency dependent heat capacity was by Fixman[29]. He showed that density fluctuation contributions to the heat capacity gave rise to an anomaly in the dispersion and attenuation. More recently, Lallemand[16] has used a frequency dependent heat capacity to model light scattering

from a diatomic gas.

c Renormalization Group Theory

The current approaches to critical phenomena use the critical exponents and scaling functions assumed in the direct solutions of models and then consider how symmetry transformations affect parameters in the model. The set of symmetry transformations is the renormalization group (RG). The direct solution approach is usually very difficult to carry out and RG may considerably simplify the detailed calculations. However, to date the RG is not a substitute for the complete analytical solution. RG applied to critical phenomena is found in Ma[30] and Hohenberg & Halperin[31].

Nolan[32] used RG methods to re-analyze the sound propagation problem. The motivation for this calculation is that there exist perturbative expansion techniques in RG which are non-existant in mode coupling schemes. Higher order terms in the expansions in RG are equivalent to adding more modes and coupling more modes together, and are easier to perform since their origins are rooted in the calculations ab initio. Thus, to lowest order in "ϵ" of RG, Nolan reproduced the earlier mode coupling results of Kawasaki[33] (the RG calculations are carried out for the expansion parameter $d - \epsilon$ where d is the dimensionality of the system; $d > 4, \epsilon > 0$). However, the temperature dependence of ξ was too strong and did not agree with the later Kawasaki-Mistura results of the preceding sections. The calculation was improved by using a 1/n expansion (n is the dimensionality

of the spin vector), but then scaling properties were lost. In order to make a comparison with experiments, and avoid higher order calculations, several ad hoc assumptions were made. Nolan's results for d = 3 were:

$$\alpha_\lambda^c(\omega) = \bar{S} 2\pi \xi \, Re \, \frac{\bar{\nu} I(\bar{\nu})}{1 + \bar{u} n \left(i \bar{\nu} I(\bar{\nu}) + \frac{1}{8\pi} \right)}$$

$$\frac{V(\omega) - V_0}{V_0} = \bar{S} \xi \, Im \, \frac{\bar{\nu} I(\bar{\nu})}{1 + \bar{u} n \left(i \bar{\nu} I(\bar{\nu}) + \frac{1}{8\pi} \right)}$$

$$I(\bar{\nu}) = \int \frac{|d\vec{x}|}{(2\pi)^3} \, \frac{1}{(1+x^2)^2} \, \frac{1}{-i\bar{\nu} + x^2(1+x^2)}$$

$\bar{S}$ is a constant set by experiment, $\bar{u} = 8\pi^2 \epsilon / 9$, and n was set equal to unity. The important point is that the scaled frequency $\bar{\nu}$ is given by:

$$\bar{\nu} = \frac{\omega \xi^4}{2\left(\frac{\lambda}{\rho c_p}\right) \xi^{18\epsilon/19}}$$

which for $\epsilon = 1$ gives a ξ dependence known to disagree with ultrasonic and Brillouin experiments on xenon[27,28,43] (compare $\bar{\nu}$ with ω^*).

These results make an absolute comparison of theory and experiment difficult. No mention is made of how to calculate $\bar{S}$. There is the (admittedly) erroneous ξ dependence, and assumptions were made (regarding the 1/n and perturbation expansions) that are not easily interpreted. Nolan nonetheless attempted to compare his results with the ultrasonic data of Roe & Meyer[34] on He^3 and found his results described the dispersion well and agreed with Fixman-Kawasaki,

but neither his results nor the Fixman-Kawasaki results described the attenuation. $\bar{S}$ was apparently determined by fitting the theory to low $\bar{\nu}$ data and attributing all departures from theory to higher frequency deviations.

Because of the arbitrariness in determing $\bar{S}$, the incorrect dependence on the correlation length, and since Nolan's calculations still show substantial departure from the Roe & Meyer data, this formulation of the sound propagation theory will not be used in a detailed comparison of the data of the present experiment with theory.

C Long Range Behavior of Correlation Function

Returning to the compressibility equation for the normal fluid,

$$S(\vec{q}) \approx S(0) = 1 + \int_0^{r_i} |d\vec{r}| (g(r)-1) = \rho k_B T K_T \quad 1.6$$

and with the asymptotic dependence of K_T near T_c given by, $K_T \sim \epsilon^{-\gamma}$, it is seen that S(q) is modified near the critical point, and that mathematically this is due to the divergence of the integral at its upper limit. The enhanced scattering near T_c is critical opalescence. The divergence implies g(r) becomes long ranged near T_c. Ornstein & Zernike[35] [36] (OZ) provided the earliest explanation of the long range behavior of g(r). The net correlation function, G_{Net}, was determined to be:

$$G_{Net} = (g(r)-1) = \frac{1}{4\pi\rho R^2} \frac{e^{-r/\xi}}{r}, \quad r \to \infty$$

ξ is the usual correlation length, R is a phenomenological parameter. The basic assumption in the derivation is worth noting. It was postulated that

$$G_{Net}(r_{12}) = C(r_{12}) + \rho \int C(r_{13})\, G_{Net}(r_{32})\, |d\vec{r}_3|$$

where $C(r_{12})$ is a direct correlation function directly dependent on the pair potential, and the integral represents the totality of all indirect correlations via intermediate points. Thus, all many body effects are averaged together by this integration. With $R^2 = \xi^2/(\rho\, k_B T K_T)$ [36],

$$S(q) \sim \frac{\rho^2 k_B T K_T}{1 + (q\xi)^2} \qquad 1.18$$

For many different critical systems, including fluids, it is found experimentally that plots of the reciprocal scattered intensity versus q^2 (Ornstein-Zernike-Debye plots) are not strictly linear. As $T \longrightarrow T_c$, downward curvature is displayed[36]. This has been interpreted to mean that the OZ form is invalid very near T_c, though there are a number of equally competitive experimental difficulties, e.g., gravitationally induced density gradients[48] and multiple scattering[48,49].

From 1.18, it is seen that the critical and normal regions for light scattering experiments in fluids depend on $q\xi$:

$q\xi \ll 1$ hydrodynamic region

$q\xi \gg 1$ critical region

When $q\xi \sim 1$, nonlocal effects must be included in a modified

hydrodynamic theory. For $q\xi >> 1$, no complete dynamical description yet exists. Once again the fundamental scale variable is the correlation length. As $T \rightarrow T_c$, ξ becomes comparable to the wavelength of light. It is for this reason that visible light can be used to probe g(r) in the critical region (the short range behavior of g(r) in normal liquids is accessible through x-ray and thermal neutron scattering[37]).

To account for the expected departure of g(r) near T_c, Fisher[38] (F) proposed that,

$$G_{Net} \sim \frac{e^{-r/\xi}}{r^{1+\eta}} \qquad \eta > 0 \qquad 1.19$$

with η an additional critical exponent now called the Fisher correction. Subsequent work by Fisher-Burford[39] (FB &FT), Fisher-Langer[40] (FL), and Ferer, et al[41] has led to the following forms for the scattering function S(q) near the critical point:

$$S_{FT} \sim \frac{\sin((1-\eta)\,\mathrm{TAN}^{-1}(q\xi))}{q\,(\xi^{-2}+q^2)^{(1-\eta)/2}} \qquad 1.20$$

$$S_{FB} \sim \frac{(1+(\phi q\xi)^2)^{\eta/2}}{1+(1+\tfrac{1}{2}\eta\phi^2)(q\xi)^2} \qquad 1.21$$

$$S_{FL} \sim \frac{1}{(q\xi)^{(2-\eta)}}\left(1-\frac{D_1}{(q\xi)^p}-\frac{D_2}{(q\xi)^{1/\nu}}\right) \qquad 1.22$$

$$S_F \sim \frac{1}{(1+(q\xi)^2)^{(1-\eta/2)}} \qquad 1.23$$

The various parameters D_1 , D_2, ϕ, are defined in the respective references. To date, no experiment on any critical system has proven independently that η is greater than zero[44] ($\eta = 0$ is the OZ form). Most scattering experiments have made use of the scaling relation theories of Kadanoff[45] and Fisher[38][46], which predict that $(2 - \eta)\nu = \gamma$, to determine η. Measurements determine ν and γ, η is then calculated; clearly this is not an independent determination of η.

Now the effects of departures from the OZ correlation function for Rayleigh linewidth measurements have been analyzed in detail by Swinney & Saleh[42]. They investigated the forms FT, F, and FB and departures of the linewidth from OZ were calculated to be from 1% to 11% for $0.1 \leq q\xi \leq 10$. While experimental linewidths accurate to 1% are achievable using digital correlation methods, not all measurements have used this technique so that experimental uncertainties are generally $\pm$ 6%[23]. Additionally, other corrections such as a vertex correction (higher order terms in the mode coupling expressions), and a high frequency shear viscosity (nonlocal viscosity) correction, are comparable in magnitude to the correlation function modifications and mask their effect. Even the accurate measurements by Chu, et al[46] on multiple component fluids, where the vertex and viscosity corrections were taken into account, could still not distinguish among the scattering functions above.

For the Brillouin spectrum, sound propagation involves

the temperature derivative of the correlation function; therefore, it should be very sensitive to the functional form of G_{Net} [47]. This is the major motivation for the present experiment: to discern departures from OZ from Brillouin scattering measurements in xenon. A secondary motivation is to test the Kawasaki-Mistura theories, especially in the high frequency region, $\omega^* > 10$.

In particular, the Kawasaki-Mistura integrals for the dispersion and attenuation were displayed previously for OZ. If the correlation function dependence is taken into account, then[43]:

$$J(\omega^*) = \int_0^\infty \frac{(x\,g(x))^2\,\omega^{*2}\,dx}{K_0^2(x) + \omega^{*2}} \qquad 1.24$$

$$I(\omega^*) = \int_0^\infty \frac{(x\,g(x))^2\,\omega^*\,K_0(x)\,dx}{K_0^2(x) + \omega^{*2}} \qquad 1.25$$

$$g(x) = \frac{-1}{2G_{NET}} \left(\frac{\partial G_{NET}}{\partial T}\right)_q \left(\xi \frac{\partial \xi^{-1}}{\partial T}\right)^{-1} \qquad 1.26$$

$$x \equiv q\xi.$$

References for Chapter I

1. The derivation in this section essentially follows G. Benedek, in Statistical Physics, Phase Transitions, Superfluidity Vol.2, ed. by M. Chretien, E.P.Gross and S.Deser (Gordon and Breach, New York,1968), p. 10-18.

2. H. Z. Cummins, in Photon Correlation and Light Beating Spectroscopy, ed. by. H.Z.Cummins and E.R.Pike (Plenum, New York, 1974), p.288.
   Note: Higher order correlations are accessible but for Gaussian fields only the two lowest order correlations are needed to obtain all higher order correlations.

3. L. Landau and E.M. Lifshitz, Electrodynamics of Continuous Media, sec. 94 (Addison-Wesley, Reading, MA.,1960).

4. B. Berne and R. Pecora, Dynamic Light Scattering, p.223 (Wiley, New York, 1976).

5. L. Van Hove, Phys. Rev. 95, 249 (1954).

6. P. Egelstaff, An Introduction to the Liquid State, p.15 (Academic, New York, 1967).

7. Ref. 6, p. 93.

8. Ref. 6, p.21.

9. L. Onsager, Phys. Rev. 37, 405 (1931).
   Phys. Rev. 38,2265 (1931).

10. R. Zwanzig, in Boulder Lectures in Theoretical Physics Vol. VIII (Wiley, New York,1961), p.135-141.

11. H. Mori Prog. in Theor. Phys. 33, 423 (1965).
    Prog. in Theor. Phys. 34, 399 (1965).

12. B. Berne, in Physical Chemistry Vol. VIII B (Academic, New York, 1971), Chap.9.

13. Ref. 4, Chap. 10.

14. L. Landau and G. Placzek, Phys. Zeit. Sow. 5, 172 (1934).

15. R. Mountain, Rev. Mod. Phys. 38, 205 (1966).

16. P. Lallemand, in Ref.2, p. 237.

17. E. Pike, in Ref.2, p. 9.

18. B. Chu, Laser Light Scattering, Sec. 3.4.2 (Academic, New York, 1974).

19. H.E. Stanley, Phase Transitions and Critical Phenomena (Oxford, New York, 1971).

20. H. Cummins, in Critical Phenomena, ed. by M. Green (Academic, New York, 1971), p.407.

21. H. Swinney, in Ref. 2, p. 331.

22. D. Henry, H.L.Swinney and H.Z.Cummins Phys. Rev. Lett. 25, 1170 (1970).
D. Henry, Ph. D. Thesis, Johns Hopkins Univ., 1970 (unpublished).
T.K.Lim, Ph. D. Thesis, Johns Hopkins Univ.,1973 (unpublished).

23. H. L. Swinney and D.L.Henry, Phys. Rev.A 8, 2586 (1973).

24. L. Kadanoff and J. Swift, Phys. Rev. 166, 89 (1968).

25. K. Kawasaki, Phys. Rev. A 1, 1750 (1970).

26. L. Landau, E.M.Lifshitz, Fluid Mechanics sec. 78 (Addison-Wesley, Reading, MA.,1959).

27. L. Mistura, in Ref. 20, p.563.

28. D. Eden, C. Garland and J. Thoen, Phys. Rev. Lett. 28, 726 (1972).

29. M. Fixman, J. Chem. Phys. 33, 1361 (1960).
J. Chem. Phys. 36, 1961 (1962).

30. S. Ma, Modern Theory of Critical Phenomena (Benjamin, Reading, MA., 1976).

31. P. Hohenberg and B. Halperin,Rev. Mod. Phys. 49,435 (1977).

32. M. Nolan, Ph.D. Thesis, Univ. Chicago, 1977.

33. K. Kawasaki and M. Tanaka, Proc. Phys. Soc. 90, 791 (1967).

34. D. Roe and H. Meyer, J. Low Temp. Phys. 30, 91 (1978).

35. L. Ornstein and F. Zernike, Physik.Z. 19, 134 (1918).
Physik.Z. 27, 761 (1926).

36. Ref. 19, Chap. 7; Ref. 20, p.397.

37. Ref. 6, Chap. 6.

38. M. E. Fisher, J. Math. Phys. 5,944 (1964),

39. M. Fisher and R. Burford, Phys. Rev. 156,583 (1967).

40. M. Fisher and J. Langer, Phys. Rev. Lett. 20,665 (1968).

41. M. Ferer, M. Moore and M.Wortis, Phys. Rev. Lett. 22, 940 (1969); 22, 1382 (1969).

42. H. Swinney and B. Saleh, Phys. Rev. A 7, 747 (1973).

43. P. Tartaglia and J. Thoen, Phys. Rev. A 11, 2061 (1975).

44. C. Tracy and B. McCoy, Phys. Rev. B 12, 368 (1975).

45. L. Kadanoff, Physics 2, 263 (1966).
L. Kadanoff, et. al, Rev. Mod. Phys. 39, 395 (1967),

46. B. Chu, S. Lee and W. Tscharnuter, Phys. Rev. A 7,353 (1973).
B.Chu and F. Lin, J. Chem. Phys. 61,5132 (1974).

47. K. Kawasaki, in Phase Transitions and Critical Phenomena Vol. 5A, ed. by C. Domb and M.S.Green (Academic, New York, 1976).

48. M. R. Moldover, J.V.Sengers, R.W. Gammon and R.J.Hocken, Rev. Mod. Phys. 51, 79 (1979).

49. L. Reith and H.L.Swinney, Phys. Rev. A 12, 1094 (1975).

CHAPTER II

REVIEW OF THEORETICAL/EXPERIMENTAL WORK

A. Sound Propagation Experiments in Xenon

On the basis of the frequencies that may be covered, sound propagation measurements divide easily into ultrasonic and light scattering methods.

Ultrasonic methods for critical xenon range from 1 kHz to 7 MHz. At the low frequency end, sample cells or resonators become physically large. At the high frequency end, the attenuation of xenon near T_c becomes so large as to place the detector at its limit of sensitivity.

Light scattering is further divided into interferometric, and light beating methods. Interferometry covers the region from 300 MHz (near T_c) well into the gigahertz regime (far from T_c). The low frequency limit is imposed by the practical difficulty of maintaining two mirrors parallel to fractions of a wavelength over large separations, and by laser frequency stability. The high frequency measurements in xenon have stopped at a few hundred megahertz. This is due to the small sound velocity of xenon, which determines the shift, and to the low intensity signals from gases far from T_c.

The range from 1 - 100 MHz may be covered by light beating in the form of heterodyning with spectrum analysis. At the low frequencies, scattering angles become exceedingly small, $\gtrsim 0.1^{o}$, and are difficult to measure. The high frequency limit is imposed by signal considerations. For

coherent detection, at least two photons per optical bandwidth per measurement time are needed. The Brillouin spectral density diminishes rapidly with increasing scattering angle, since the intensity is approximately constant, but $\Gamma_B \propto q^2$.

These methods will be briefly reviewed in terms of what is measured, advantages/disadvantages, and limitations. Previous sound propagation experiments on critical xenon will be discussed.

1 Ultrasonic Experiments

The probe is a sound wave of fixed frequency forced through the fluid and generated by a piezo-elastic quartz crystal transducer. Velocity is determined from measurements of either displacement and time delay, or frequency and wavelength. Absorption is determined from the amplitude change of a known signal over a known distance, and by comparison with an unattenuated wave derived from the same source. Two instruments have been used, a resonant cell and pulsed interferometer.(1)

The resonant cell is a cavity of known simple shape. It is filled with the sample, then excited externally. The resonance curve for particular modes is determined, and/or the decay of pulsed waveforms from a given source. This method has yielded the lowest frequency sound velocity measurements, and over a wide range of temperature and pressure. Corrections for cavity end effects, complex calibration, difficulty in separating losses in the walls from those in the liquid, and

the short path lengths required for high frequencies are the disadvantages and limitations. Near T_c, high attenuation reduces the strength of the resonance and broadens the resonance peak, making it difficult to determine the center frequency. This is the fundamental limitation.

Kline & Carome[2] used the longitudinal modes of a cylindrical cavity to determine the velocity from the relation, $v = 2df$, where d is the acoustical length, and $6\ \text{kHz} < f < 11\ \text{kHz}$. Density ranged over $.93 < \rho/\rho_c < 1.11$, temperature $-0.1^\circ < \Delta T < 10^\circ C$. Errors in velocity were 1 - 2% near T_c and the attenuation was not determined. Dispersion was evident when their data were compared with the .55 MHz data of Mueller[3].

Garland & Williams[4] measured the resonant frequency of an azimuthal mode in a horizontal annular cavity where $v = 2\pi rf$, r being the radius. The advantages of this geometry over that of Kline & Carome were longer path lengths (lower frequencies), and short vertical height so that gravitational gradient effects were a minimum. No cavity end corrections were needed, and the azimuthal mode was well separated from other modes. Data were determined on the critical isochore for $0^\circ < \Delta T < 2^\circ C$, and for frequencies over $0.6\ \text{kHz} < f < 3\ \text{kHz}$. No dispersion was detected in this region. Results for f = 1 kHz were shown to be the zero frequency limiting values of the velocity, within experimental error. This was an important result since comparisons of data with the Kawaski-Mistura predictions of dispersion ($v(\omega) - v_o$) and attenuation demand accurate values for v_o.

The original pulsed interferometer consists of a sample placed between two transducers, one acting as source, the other as receiver. Velocity is obtained from the time a sound pulse takes to get from source to receiver for a known transducer spacing. The received pulse can be compared to a similar pulse of the same frequency emerging from a calibrated attenuator. The change in attenuation (amplitude) as the path length is varied gives the absorption. Compared with older continuous wave interferometer designs, pickup of input excitations, transducer coupling perturbations, and the low Q of lossy samples are eliminated. However, to achieve signal separation in successive pulses, long path lengths and high frequencies must be used. This causes additional delay and amplitude loss in the pulse. Also, diffration corrections are necessary.

Williamson & Eden[5] improved the pulsed interferometer method by phase comparison of the signal with a coherent reference signal. Phase sensitive detection in a balanced mixer provides linear output and high sensitivity, and boxcar integration improves the signal to noise ratio. Corrections for phase shifts at the transducers are avoided by differential path measurement. Diffraction effects must still be accounted for, and the ultimate limitation is the high attenuation near T_c. Velocity accuracy of $\pm$ 0.2%, and attenuation accuracy of $\pm$ 2.0% have been claimed.

This improved technique was used by Garland, et al[6], and Mueller, et al[3] for frequencies of 0.4, 0.55, 1, 3, 5, and 7 MHz, for $\rho / \rho_c = 1.01$ and $-0.8^{\circ} < \Delta T < 20^{\circ}C$. Thoen & Garland[7]

used the same method at frequencies of 0.6, 1 and 3 MHz, $-0.1^{o} < \Delta T < 0.5^{o}$C in both coexisting phases, and for densities near the critical isochore. In addition, dielectric constant measurements were performed at each point to accurately determine the density in the latter experiment.

It should be mentioned that the earliest investigations of xenon were performed by Chynoweth & Schneider[8]. Velocity data were obtained for $-1.45^{o} \leq \Delta T \leq 2.12^{o}$C and for $0.25 < f < 1.25$ MHz. A 6% dispersion was reported between these frequencies near the transition, while less than 1% experimental error was expected. Attenuation measurements were unreliable, and only reported for .25 MHz, but it was mentioned that attenuation became frequency independent near T_c.

2 Light Scattering Experiments

As presented in Chapter I, the Brillouin spectrum gives the sound velocity from the frequency shift, and the attenuation from the linewidth. The velocity is determined from the relation, $v = f_B \lambda_o / (2n \sin\theta/2)$, where f_B is the frequency shift (Hz), λ_o the incident laser wavelength, n the refractive index, and θ the scattering angle. The attenuation (per wavelength) is $\alpha_\lambda = 2\pi \Gamma_B / \omega_B$ (Γ_B in rad/sec). It is seen that by varying the angle, a different thermal phonon is selected for measurement.

The advantages of light scattering are the resolution achievable with present instrumentation, the higher frequencies attainable (compared to ultrasonics), and the fact that a minimal amount of perturbation of the system is introduced

by the measurement process. From previous determinations of Brillouin shifts and linewidths[45], instrumental resolving powers of 10^{+5} - 10^{+7} and 10^{+7} - 10^{+11} are needed, respectively. The best present day Fabry-Perot interferometers are capable of 10^{+8} - 10^{+9} resolving powers, while light beating methods are capable of 10^{+14}.

a Interferometry

Cummins & Swinney[9] used a piezoelectrically scanned, confocal Fabry-Perot of 5 cm plate separation. The resolving power was 10^{+6} - 10^{+7}, the free spectral range about 1500 MHz, and scattering angles of 40^{o} and 90^{o} gave frequency shifts of 158 - 189 MHz, and 302 - 364 MHz, respectively. Only dispersion data were obtained as the linewidths were not resolvable. The temperature range was $0.5^{o} < \Delta T < 10^{o}$C, along the critical isochore.

The free spectral range of a confocal Fabry-Perot is $\Delta\nu = c/4d$, where d is the plate separation, and c the velocity of light[10]. The resolution (in frequency) is determined by dividing $\Delta\nu$ by the finesse. For a confocal instrument, the finesse is $\pi/(d(1-R))$, where R is the reflectivity coefficient of the plates[10]. A resolution in the area of 10 - 30 MHz would be considered good enough to resolve the linewidths expected. This could be achieved either by having mirrors of high reflectivity and excellent surface quality so that the finesse is large or by decreasing the free spectral range. Mirrors of high reflectivity are easy to obtain, but surface figure will ultimately limit the finesse. Very good

finesses are 50 - 80, with over 100 considered to be exceptional. A decrease in the free spectral range means large plate separation, but it becomes very difficult to maintain the plates within the required parallelism. Also, the laser linewidth enters into the intrumental response, and laser frequency stability better than about 1 - 10 MHz is difficult to achieve at present.

An additional limitation is imposed by the spectrum itself. In interferometry, the complete spectrum is seen, so that the Rayleigh line overwhelms the weaker Brillouin components, the more so as T_c is approached. Instruments of high contrast ($\sim 10^6$) are required.

The only other interferometric measurement was that of Cannell & Bendek[11] who used two pressure swept confocal Fabry-Perots in tandem. Their resolution was 20 MHz, and contrast $\sim 10^8$. Frequency ranged over $436 < f_B < 576$ MHz for $\theta = 170^\circ$, and $0.1^\circ < \Delta T < 20^\circ$C along the critical isochore.

Simultaneously sweeping the transmission functions of two separate instruments while maintaining their relative alignment is very difficult. Slight temperature fluctuations or vibrations can cause the mirrors to drift out of alignment. The great advantages of this approach were the resolution and contrast achievable. The free spectral range was that of the smaller plate separation instrument, while the resolution was better than either separate Fabry-Perot[12]. The contrast was the product of the individual contrasts. Cannell was able to come within 125 MHz of the Rayleigh line and see an additional

non-propagating mode centered at the Rayleigh peak, and extending between it and the Brillouin peaks. Complete Brillouin linewidth data were obtained by accurately deconvolving the instrumental response from the observed spectra[13].

b Light Beating

In light beating, no optical frequency filter is used as in interferometry. Scattered light is imaged directly onto the detector. It is mixed with itself, homodyning, or with a coherent reference, heterodyning. The photo-current spectrum is then analyzed either in the time domain with a correlator, or in the frequency domain using a spectrum analyzer. The heterodyne method was used in this experiment; an extensive discussion is presented in a following section. Here, a brief discussion will be given explaining why heterodyning, as opposed to homodyning, must be used.

Present day correlators are multichannel devices with the fastest sampling times limited to about 10 ns. For a typical 60 channel device, assuming that at least two decay times are spanned (twice the half width), the upper frequency limit is 0.6 MHz. This frequency response is too low for even the lowest scattering angles of interest in Brillouin scattering. On the other hand, spectrum analyzers are available covering frequencies from 1 Hz to 40 GHz[14]. Heterodyning adds a strong local oscillator (LO) to the weak Brillouin signal. Consider an idealized case where the (Stokes only) Brillouin signal is represented by A $\cos \omega_1 t$ and whose width is a delta function in frequency space, and the LO by B $\cos \omega_2 t$. Then the output current of the square law detector, i(t) = (A cos

$\omega_1 t + B \cos \omega_2 t)^2$, will contain an a.c. component, AB cos $(\omega_1 - \omega_2)t$, which is the signal of interest. If $A \ll B$, the power is increased from $A^2/2$ (the d.c. current of the signal alone), to AB, or a factor of 2B/A. This conversion gain is obtained with no increase in noise. If homodyning were used under the same conditions, then the LO is the signal itself but since it is so weak, there is no gain. The combination of relatively high frequency and weak Brillouin signal dictates the use of the heterodyne technique and spectrum analysis.

The only optical heterodyne Brillouin scattering on xenon was done by Eden & Swinney[15,33]. Spectra were obtained for angles of 0.6^o, 1.3^o, 2.5^o, and 5^o in the vapor phase below T_c for $0.2 < T_c - T < 7^oC$ and frequencies in the range $2 < f_B < 24$ MHz on the coexistance curve.

B. A Fundamental Difference between Ultrasonics & Light Scattering

While the two methods above are obviously experimentally different, it is of greater importance to note that they measure physically distinct quantities. In the case of ultrasonics, a travelling wave is forced through the fluid and the wave decays in space as it propagates (spatial absorption). For light scattering, naturally occurring thermally driven waves (thermal fluctuation) decay in time (temporal absorption).

The reason for this dichotomy is easily seen from an examination of the dispersion equation Mountain obtained for the spectrum by solving the hydrodynamic equations:[16]

$$s^3 + (a + D_T) q^2 s^2 + (V_0^2 q^2 + a D_T q^4) s + a V_0^2 q^4 / \gamma = 0 \qquad 2.1$$

where s is the Laplace transform variable, q the wavevector, v_o the zero frequency sound velocity, γ the specific heat ratio (Cp/Cv), a the thermal diffusivity ($\lambda / \rho C_p$), and D_T the longitudinal kinematic viscosity ($(4/3\,\eta + \xi)/\rho$). Both s and q are in general complex, so that there are four unknowns to be determined from this equation, the real and imaginary parts of s and q. By choosing the experiment, two of these quantities are fixed, the remaining two are obtained from those specified. For the ultrasonic experiment, the sound frequency is real, the wavevector complex, and the ultrasonic velocity is:

$$v_u = \omega / (\text{Real } q) \qquad \text{(spatial dispersion)}$$

For light scattering, the wavevector is real, the frequency complex, and the hypersonic velocity is:

$$v_h = (\text{Real } \omega)/q \qquad \text{(temporal dispersion)}$$

For the zero thermal diffusivity case, a = o, exact expressions for v_h and v_u were determined by Mountain[17], and Fleury and Boon[18]:

$$v_u = V_u(\omega) = \pm \frac{\sqrt{2}\, V_o (1 + D_T^2 \omega^2 / V_o^4)^{1/2}}{(1 + (1 + D_T^2 \omega^2 V_o^4)^{1/2})^{1/2}} \qquad 2.2$$

$$V_H = V_H(q) = \pm V_o (1 - D_T^2 q^2/(4 V_o^2))^{1/2} \qquad 2.3$$

Note that the thermal diffusivity is obtained from the Rayleigh linewidth.

The form for Γ_R is:

$$\Gamma_R = aq^2$$

This expression in the critical regime becomes[19],

$$\Gamma_R \sim \epsilon^{\gamma - \psi} q^2 \qquad \gamma - \psi \approx .63$$

which shows the thermal diffusivity becomes very small. Thus

taking a = o in the dispersion equation is a very good approximation near T_c. The phase velocity is seen to have positive dispersion for $v_u(\omega)$, but negative dispersion for $v_h(q)$. Mountain identified Brillouin scattering with temporal dispersion and away from T_c the phase velocity derived was (to q^2 terms)[20]:

$$V_H(q) = V_o\left(1 + \frac{3\Gamma_B^2 + aD_T - 2\Gamma_B(a+D_T)}{2V_o^2}q^2 + \cdots\right)$$

which exhibits negative dispersion.

Now near T_c sound dispersion expressions were presented in Chapter I as derived by Kawasaki and Mistura. These expressions should be used in testing scaling relations and critical phenomena predictions. But features of the spectrum must still be derived from scattering theory which relates observables to the dynamics of the fluid. Predictions for the cross section are derived from explicit models for the fluid. Even away from T_c, the classical hydrodynamic model of Mountain above is inadequate for even a simple fluid such as xenon.

The next simplest model envisions some internal degree of freedom of the fluid that couples to the translational degrees of freedom. There will be coupling between a structural mode and the thermal modes describing the density fluctuations of the fluid. The internal degree of freedom is described by a single relaxation time process appropriate for treating irreversible processes that are slow in restoring equilibrium[21]. Zwanzig[22] showed the single relaxation time model was equivalent to a frequency dependent bulk viscosity and that an explicit determination of the internal relaxation process was not required. One could, for example,

describe the rotational kinetic energy of a relaxing diatomic gas by a relaxing complex specific heat. The real part of the specific heat determines the velocity, and the imaginary part gives the damping. In view of Zwanzig's results, the complex specific heat may be rewritten in terms of a complex bulk viscosity[23]. Recall that Kawasaki's mode coupling expressions are based on just such a relaxing complex bulk viscosity, and Mistura's expression on a similar specific heat.

Mountain[24] later predicted the spectrum for such a model and showed it consisted of the normal Rayleigh-Brillouin peaks plus a fourth non-propagating peak, the Mountain mode. This has a width proportional to the relaxation rate for the bulk viscosity, τ^{-1}, and is usually seen as a broad background centered at $\omega = 0$. It was shown that negative dispersion is present in the same form as in the non-relaxing case. For values of the wavevector appropriate to Brillouin scattering ($q \sim 5000 cm^{-1}$) in liquids, negative dispersion is not usually seen since $D_T q << v_o$ in equation 2.3. Mountain and Litovitz[25] calculated the velocity and separately the negative dispersion, for CCl_4 by numerically solving the dispersion equation. A change of less than -0.2% was expected for the dispersion. The result was that the increase in velocity due to the relaxation in ζ completely overwhelmed that due to temporal absorption resulting in a net positive dispersion. The internal degrees of freedom (rotational) are seen explicitly so that this model is expected to give correct results for CCl_4. In the case of xenon there are no such internal degrees of freedom, a primary reason for choosing it for study initially. However,

the critical theories are built on a complex bulk viscosity and as stated above the exact mechanism for a structural relaxation need not be known. From the analysis of Cummins and Swinney[9] both light scattering and ultrasonic data exhibit positive dispersion, with the light scattering data giving at least +(2 - 3)% dispersion ((v(ω) - Vo)/Vo). It is seen that the anomalous behavior of the bulk viscosity near T_c provides a structural relaxation mechanism so large as to overwhelm the negative dispersion due to Brillouin scattering, resulting in net positive dispersion for the light scattering measurements as well.

Further evidence that the relaxing bulk viscosity model should be used to describe even a simple liquid like xenon was provided by Cannell.[11] He observed the predicted Mountain mode in xenon with $\tau = .3 \times 10^{-9}$ sec (for $\Delta T = 1^{o}C$). Cannell interpreted the Mountain mode as arising from a structural relaxation. Two relaxation times are produced, one is the thermal diffusion time discussed earlier, $\omega_R = (\lambda / (\rho Cp)) \xi^{-2}$, and the second is the time required for a sound wave to cross a correlation length, $\omega_\xi = V / \xi$. Cannell's high resolution measurements enabled the observation of the regime where $\omega_\xi >> \tau^{-1} >> D_T q^2$. The structural relaxation was too slow to affect the Brillouin line, but too rapid to affect the Rayleigh line. The structural rearrangements must occur at constant pressure ($\tau >> \omega_\xi^{-1}$) and constant entropy ($\tau << (D_T q^2)^{-1}$).[26]

Deguent and Boon[27] used generalized hydrodynamics and a generalized regression of fluctuations theory (GRF) to obtain a

more complex dispersion equation than Mountain. The GRF theory is an extension of the single relaxation time hypothesis. However, it is more general since no assumption is made about the duration of the process relaxing toward equilibrium. Transport coefficients become transport functions. The equivalence of the phenomenological GRF theory to the master equation-autocorrelation funtion formalism of Boon and Deguent[28] for generalized hydrodynamics was demonstrated. They also compared the GRF theory with the single relaxation time model of Mountain. The low and high frequency limits were identical, as expected. However, in the intermediate frequency range their expressions yielded better results when compared to data for CCl_4. Assuming that the kernel of the transport equation had a single, simple pole (single characteristic frequency), they derived the bulk viscosity, attenuation, and both v_h and v_u. Their results were:[29]

$$V_H = \pm \frac{V_0}{\sqrt{2}} \left(1 + \frac{\omega \zeta''(\omega)}{\rho V_0^2} + \frac{|c|^2}{V_0^2}\right)^{1/2}$$

$$V_U = \pm \sqrt{2}\, \frac{|c|^2}{V_0} \left(1 + \frac{\omega \zeta''(\omega)}{\rho V_0^2} + \frac{|c|^2}{V_0^2}\right)^{1/2}$$

$$\frac{|c|^2}{V_0^2} = \left[\left(1 + \frac{\omega \zeta''(\omega)}{\rho V_0^2}\right)^2 + \left(\frac{\omega \zeta'(\omega)}{\rho V_0^2}\right)^2\right]^{1/2}$$

$$\zeta(\omega) = \zeta'(\omega) + i\,\zeta''(\omega) = \frac{V_\infty^2 - V_0^2}{1 + \omega\tau}\,\tau\rho$$

Dispersion is positive for <u>both</u> ultrasonic and hypersonic velocities. The ultrasonic velocity was always found to be greater than the hypersonic velocity, and $v_h\, v_u = v_o^2$ ($v_o = \partial P/\partial \rho_s$). In the high frequency limit, $v_u = v_h = v_\infty$ and in

the long wavelength limit, $v_u = v_h = v_o$.

As stated above, Mountain identified the Brillouin frequency as temporal dispersion but it was pointed out by Montrose et al[30] that the peaks were actually thermally driven resonance lines, that is, the scattered light is modulated by the acoustic mode driven in turn by random thermal forces (temperature fluctuations). Therefore, phase velocity is not the Brillouin frequency divided by the wavevector of a temporally damped wave. The Brillouin lines are Lorentzian only for a freely decaying system; the driven system is distinctly non-Lorentzian.

This difference in the Brillouin phase velocity was emphasized by Bhatia and Tong[31] who analyzed algebraically the dispersion equation for a system with complex bulk viscosity. The Brillouin phase velocity, $v_B = \omega_B / q$, must be identified from the expression for the spectrum $S(q,\omega)$ by finding the maximum of $S(q,\omega)$. Mountain's own four peaked spectrum was used to find the extrema. In the limit where $v_o\, q\, \tau \ll 1$,

$$\frac{V_B^2}{V_o^2} \approx 1 - \frac{1}{2}(V_o q \tau)^2 \left(V_\infty^2/V_o^2 - 1\right)\left(V_\infty^2/V_o^2 - 3\right)$$

whereas in the same limit for v_h:

$$\frac{V_h^2}{V_o^2} \approx 1 - \frac{1}{4}(V_o q \tau)^2 \left(V_\infty^2/V_o^2 - 1\right)\left(V_\infty^2/V_o^2 - 5\right)$$

For $v_\infty^2/v_o^2 > 3$ v_B showed negative dispersion. For $3 < v_\infty^2/v_o^2 < 4$ there was a range of $v_o q \tau$ ($v_o q \tau \sim .5$ - $.75$) where there were no Brillouin peaks. For $v_\infty^2/v_o^2 \geq 3$, there is obviously a great difference between v_B and v_h; however, no known

liquid fulfills this requirement. For $v_o q \tau = 0.5$, v_h differed from v_B by + 13.5% and v_u differed from v_B by 28%. Only when the sound absorption per cycle was much smaller than one ($v_\infty^2 / v_o^2 - 1 \ll 1$) were all three velocities comparable.

It is clear that the Brillouin frequency may be viewed as a temporal dispersion process, but not simply a freely decaying wave. The relaxing bulk viscosity model, which leads to the additional Mountain peak, seems to be the most appropriate in view of Cannell's experiment. Care must be taken in determining the sound velocity from the spectrum. When comparing velocity and attenuation with specific models, the Brillouin shift must be identified from the extrema in the cross section, which also depends on boundary conditions. If the four peak model spectrum is to be used to fit data, it is of interest to calculate the changes expected due to the additional central mode (Mountain mode).

The effect of the Mountain mode on the Brillouin peaks is to push them away from the Rayleigh line and introduce additional asymmetry; the low frequency side of the Brillouin peak has greater spectral density than the high frequency side. The expected shift for the Brillouin lines for a bulk viscosity which relaxes in time τ is:[32]

$$\omega_M = \frac{1}{\tau\sqrt{2}}\left[(V_\infty q\tau)^2 - 1 + \left[\left(1-(V_\infty q\tau)^2\right)^2 + (2V_o q\tau)^2\right]^{1/2}\right]^{1/2}$$

while the hypersonic frequency would be simply: $\omega_B = v_h q$.

Using Cannell's data for xenon at $\Delta T = 1.03^\circ C$:[11]

$$v_o = 1.18 \times 10^4 \text{ cm/s}$$
$$v = 1.34 \times 10^4 \text{ cm/s}$$

$$v_h = 1.268 \times 10^4 \text{ cm/s}$$
$$q = 2.25 \times 10^5 \text{ cm}^{-1}$$
$$\tau = 0.35 \times 10^{-9} \text{ s}$$

in the above expressions, obtain for ω_M and ω_B:

$$\omega_M = 2.840 \text{ GHz}$$
$$\omega_B = 2.835 \text{ GHz}$$

The Brillouin line has been shifted away from its expected position by an additional +0.2% due to the presence of the Mountain mode. A similar calculation for data at $\Delta T = 0.1^{\circ}C$ yields a shift of +0.9%. For the present experiment, these changes are less than the experimental uncertainty.

Cannell also noted the intensity of the extra mode increased near T_c and for $\Delta T = 0.1^{\circ}C$, its integrated intensity was twice the integrated intensity of one Brillouin component. This should make a difference in the ratio, $I_R/(2I_B)$, which for low frequencies is the classical Landau Placzek ratio: $C_p/C_v - 1$.

Due to the nature of the spectrum-analyzed heterodyne experiment, the complete Rayleigh-Brillouin spectrum cannot be seen in a single scan of the instrumentation as it can be in interferometry. Either the Rayleigh or Brillouin line can be scanned separately. Additionally, though the local oscillator mixes with both the Stokes and anti-Stokes Brillouin components in the scattering volume, spectrum analysis does not detect "negative" frequencies. Thus, the anti-Stokes and Stokes components are folded together by the post detection signal processing. Typically, the experimental scan range is only six Brillouin halfwidths. Therefore, it is not possible to detect

easily the presence of the Mountain mode by looking for an increase in spectral density between the central component and Brillouin line. It is not at all possible to obtain integrated intensities. For these reasons, and the fact that the Mountain mode induced line center shifts are so small (note also that the Mountain mode width is about 3000 MHz), the four peak model spectrum will not be used to fit the data of the present experiment.

Finally, consider the spectrum presented in equation 1.8. The asymmetric terms bring the Brillouin frequency closer to the Rayleigh line, compared to the original spectrum derived by Mountain[16] that did not include these terms. But these terms are preceded by a factor,

$$b(q) = \frac{q\ (3\ \Gamma_B - D_V)}{(C_p/C_v)\ v_o}$$

Let us now examine this factor near the critical point. The quantities in b(q) become, asymptotically near T_c:[19]

$$\Gamma_B \sim \epsilon^{-(\gamma-\alpha)}$$

$$D_V \sim \epsilon^{-\psi}$$

$$C_p/C_v \sim \epsilon^{-(\gamma-\alpha)} \quad \text{with } \gamma \approx 1.2,\ \alpha \approx 0.1,\ \psi \approx 0.6$$

so that $b(q) \sim (q/v_o)\,\epsilon^{.5}(\epsilon^{.1} - 1)$ which goes to zero near T_c. At $\Delta T = 1^o$ in xenon at the critical density, and for q = 6000 cm^{-1} (largest wavevector of the present experiment), v_0 = 106 m/s and the factor $b(q) = 1.9 \times 10^{-3}$. In addition, it will be shown in a later chapter that the instrumental effects of the present experiment are quite difficult to deconvolve from the observed spectra. It is not expected that the deconvolved spectra will

be accurate enough to show the departures from the simple Lorentzian lineshape when the asymmetric terms are included.

From the discussion in this section, it is concluded that the Brillouin spectra for this experiment will be well represented by a simple Lorentzian lineshape. The Rayleigh-Brillouin spectrum is then that of equation 1.8 with the last two terms discarded, since b(q) is so small. This is in fact the original spectrum derived by Mountain from the simplest hydrodynamic model.[16]

C. The Heterodyne Method

1. Power Spectrum Derivation

The heterodyne photocurrent power spectrum for Brillouin scattering in a liquid will now be derived. Classical coherence functions can be used to describe all optical fields.[34] The fields themselves are complex analytic signals of space and time. Since in an isotropic monatomic liquid the fluctuations in the polarizability tensor are mainly due to density fluctuations, and these contribute no off-diagonal elements to the tensor, the scattered fields will have the same polarization as the incident field. Thus, vector notation will be dropped; the scattered field has the same polarization as the incident laser field. Also, spatial dependence will be disregarded since the fields will be assumed to be completely spatially coherent. The last assumption implicit in the derivation is that the power spectrum measurement takes an infinitely long time so that by the ergodic hypothesis a true ensemble averaged value of the scattered fields is obtained.

If the instantaneous field is E(t), then the intensity I(t) at the photocathode is $\eta E^*(t)E(t)$ where η is the isotropic quantum efficiency. From the field, one defines the first and second order normalized field correlation functions as:(35)

$$g^{(1)}(\tau) = \frac{\langle E^*(t)\, E(t+\tau)\rangle}{\langle E^*(t)\, E(t)\rangle} \qquad 2.4$$

$$g^{(2)}(\tau) = \frac{\langle E^*(t)\, E(t)\, E^*(t+\tau)\, E(t+\tau)\rangle}{\langle E^*(t)\, E(t)\rangle^2} \qquad 2.5$$

where $\langle \ldots \rangle$ denotes a time average: $\langle f(t)\rangle \equiv \lim_{T\to\infty} \frac{1}{T}\int_{-T}^{T} f(t)\,dt.$

The photocurrent, i(t), is simply e E*(t)E(t), where e is the electronic charge. Now the photocurrent correlation function has two parts, one due to the same electron, and the other due to two different electrons detected at times t and $t+\tau$ Thus, the photocurrent correlation function is:(36)

$$\langle i(t)\, i(t+\tau)\rangle = e^2\eta\,\delta(\tau)\langle E^*(t)\, E(t)\rangle + e^2\eta^2\langle E^*(t)\, E(t)\, E^*(t+\tau)\, E(t+\tau)\rangle \qquad 2.6$$

For this heterodyne experiment, the local oscillator field is that of an amplitude stabilized single mode laser that may be represented as:(37)

$$E_{LO}(t) = E_{LO}\exp(-i\omega_{LO}t). \qquad 2.7$$

A factor, $\exp(-i\phi(t))$, has been dropped, since it has been shown that the photocurrent spectrum of the laser exhibits no light beats due to random phase modulation.(38) Now the total field at the photocathode is the LO field plus the scattered field:

$$E(t) = E_{LO}(t) + E_s(t).$$

With this total field, the first term of 2.6 reduces to:

$$e^2\eta\,\delta(\tau)\langle E^*(t)\,E(t)\rangle = \left(\langle I_s\rangle + I_{LO}\right)e^2\eta\,\delta(\tau) = \left(\langle i_s\rangle + i_{LO}\right)e\,\delta(\tau). \quad 2.8$$

The second term of 2.6 reduces to:[39]

$$e^2\eta^2\,\delta(\tau)\Big[I_{LO}\left(e^{i\omega_{LO}\tau}\langle E_s^*(t)\,E_s(t+\tau)\rangle + e^{-i\omega_{LO}\tau}\langle E_s(t)\,E_s^*(t+\tau)\rangle\right)$$

$$+\langle E_s^*(t)\,E_s(t)\,E_s^*(t+\tau)\,E_s(t+\tau)\rangle\Big] + e^2\eta^2\left(I_{LO}^2 + 2\,I_{LO}\langle I_s\rangle\right) \quad 2.9$$

which may be rewritten using 2.4 and 2.5 as:

$$i_{LO}\langle i_s\rangle\left[e^{i\omega_{LO}\tau}\,g_s^{(1)}(\tau) + e^{-i\omega_{LO}\tau}\,g_s^{(1)*}(\tau)\right] + \langle i_s\rangle^2\,g_s^{(2)}(\tau) + i_{LO}^2 + 2\,i_{LO}\langle i_s\rangle.$$

Thus the complete correlation function is:

$$\langle i(t)\,i(t+\tau)\rangle = e\,\delta(\tau)\left(\langle i_s\rangle + i_{LO}\right) + i_{LO}^2 + 2\,i_{LO}\langle i_s\rangle$$

$$+\langle i_s\rangle^2\,g_s^{(2)}(\tau) + i_{LO}\langle i_s\rangle\left[e^{i\omega_{LO}\tau}\,g_s^{(1)}(\tau) + e^{-i\omega_{LO}\tau}\,g_s^{(1)*}(\tau)\right]. \quad 2.10$$

Now the Wiener-Khintchine theorem[40] may be invoked to determine the photocurrent power spectrum:

$$P(\omega) = \frac{1}{2\pi}\int_{-\infty}^{\infty} e^{i\omega\tau}\langle i(t)\,i(t+\tau)\rangle\,d\tau.$$

Substituting 2.10 one obtains:

$$P(\omega) = \frac{e}{2\pi}\left(\langle i_s\rangle + i_{LO}\right) + \left(i_{LO}^2 + 2\,i_{LO}\langle i_s\rangle\right)\delta(\omega)$$

$$+\frac{\langle i_s\rangle^2}{2\pi}\int_{-\infty}^{\infty} g_s^{(2)}(\tau)\,e^{i\omega\tau}\,d\tau \quad 2.11$$

$$+\frac{i_{LO}\langle i_s\rangle}{2\pi}\int_{-\infty}^{\infty} e^{i\omega\tau}\left[e^{i\omega_{LO}\tau}\,g_s^{(1)}(\tau) + e^{-i\omega_{LO}\tau}\,g_s^{(1)*}(\tau)\right]d\tau.$$

The first term is the shot noise term and is an overall background constant. The second term is the d.c. term which will not appear in an a.c. coupled spectrum analyzer. The third term is the homodyne term and the last contains the heterodyne

spectrum.

It was shown in the preceding chapter that the spectrum for a pure monatomic liquid exhibits a Rayleigh line and two Brillouin lines. Now the Rayleigh line acts as a local oscillator in relation to the Brillouin lines. The Rayleigh line is at the same frequency as the laser field. It may be regarded as having negligible width compared to the Brillouin lines. However, its intensity changes by about three orders of magnitude as one approaches the critical point. This intensity will not be small compared to the LO intensity provided by the laser light scattered elastically from the windows of the cell. Thus, although the Rayleigh lineshape will not be seen in the heterodyne power spectrum, it does mix with the Brillouin lines and serves as a second LO. In addition, since $\langle i_s \rangle$ appears in the shot noise term, it is immediately observed that the background constant will increase dramatically as the critical point is approached due to the divergence of the Rayleigh intensity. The weak Brillouin intensity changes little near the transition temperature, so it becomes increasingly difficult to distinguish the Brillouin signal from the background. Ultimately, the fluctuations in the background will limit the achievable detectivity.

The function $g_s^{(1)}(\tau)$ for a pure monatomic liquid was shown by Mountain[16] to be:

$$g_s^{(1)}(\tau) = e^{-i\omega_0\tau}\left(e^{-\Gamma_R\tau}(c_p-c_v)/c_p + c_v/c_p\, e^{-\tau\Gamma_B}\cos\omega_B\tau\right) = e^{-i\omega_0\tau} f(\tau)$$

where Γ_R = Rayleigh linewidth

Γ_B = Brillouin linewidth

ω_B = Brillouin frequency shift

ω_o = incident laser frequency

c_p, c_v = specific heats at constant pressure, volume, respectively

For random Gaussian fields, the second order correlation function is related to the first order correlation function by:[35]

$$g^{(2)}(\tau) = 1 + |g^{(1)}(\tau)|^2$$

Thus the third term of 2.11 becomes, with 2.12, 2.13:

$$\langle i_s\rangle^2/(2\pi)\int_{-\infty}^{\infty} e^{i\omega\tau}\, g_s^{(2)}(\tau)\, d\tau = \frac{\langle i_s\rangle^2}{2\pi}\int_{-\infty}^{\infty} e^{i\omega\tau}(1+|g^{(1)}(\tau)|^2)\,d\tau$$

$$= \langle i_s\rangle^2\delta(\omega) + \frac{\langle i_s\rangle^2}{2\pi}\int_{-\infty}^{\infty}\left(e^{-\Gamma_R\tau}\,\frac{c_p-c_v}{c_p} + \frac{c_v}{c_p}\,e^{-\Gamma_B\tau}\cos\omega_B\tau\right)^2 e^{i\omega\tau}\,d\tau$$

Expanding the last integral term:

$$\frac{\langle i_s\rangle^2}{2\pi}\left\{\int_{-\infty}^{\infty} e^{i\omega\tau}e^{-2\Gamma_R\tau}\left(\frac{c_p-c_v}{c_p}\right)^2 d\tau \right. \qquad 2.14\,a$$

$$+\int_{-\infty}^{\infty} e^{i\omega\tau}e^{-2\Gamma_B\tau}\left(\frac{c_v}{c_p}\right)^2\cos^2\omega_B\tau\,d\tau \qquad 2.14\,b$$

$$\left.+2\int_{-\infty}^{\infty} e^{i\omega\tau}e^{-(\Gamma_R+\Gamma_B)\tau}\left(\frac{c_p-c_v}{c_p}\right)\left(\frac{c_v}{c_p}\right)\cos\omega_B\tau\right\} \qquad 2.14\,c$$

Equation 2.14 a becomes immediately:

$$\langle i_s\rangle^2\left(\frac{c_p-c_v}{c_p}\right)^2 \frac{2\Gamma_R/\pi}{(2\Gamma_R)^2+\omega^2} \qquad 2.15\,a$$

Using the identity, $\cos\theta = \frac{1}{2}(e^{i\theta} + e^{-i\theta})$, equation 2.14 becomes:

$$\frac{\langle i_s\rangle^2}{2\pi}\int_{-\infty}^{\infty}\left(\frac{c_v}{c_p}\right)^2\frac{1}{4}\,e^{i\omega\tau}e^{-2\Gamma_B\tau}\left(2+e^{i2\omega_B\tau}+e^{-i2\omega_B\tau}\right)d\tau$$

$$= \frac{\langle i_s\rangle^2}{2\pi}\left(\frac{c_v}{c_p}\right)^2\frac{1}{4}\left[\frac{2(2\Gamma_B)/\pi}{(2\Gamma_B)^2+\omega^2} + \frac{2\Gamma_B/\pi}{(2\Gamma_B)^2+(\omega\pm 2\omega_B)^2}\right] \qquad 2.15\,b$$

and equation 2.14c becomes:

$$\frac{\langle i_s\rangle^2}{2\pi}\left(\frac{c_p-c_v}{c_p}\right)\left(\frac{c_v}{c_p}\right)\int_{-\infty}^{\infty} e^{i\omega\tau}e^{-(\Gamma_R+\Gamma_B)\tau}\left(e^{i\omega_B\tau}+e^{-i\omega_B\tau}\right)d\tau$$

$$= \langle i_s \rangle^2 \left(\frac{c_p - c_v}{c_p}\right)\left(\frac{c_v}{c_p}\right) \frac{(\Gamma_R + \Gamma_B)/\pi}{(\Gamma_R + \Gamma_B)^2 + (\omega \pm \omega_B)^2} \qquad 2.15\,c$$

The complete third term of 2.11 is, from 2.15a, b, c:

$$\langle i_s \rangle^2 \delta(\omega) + \langle i_s \rangle^2 \left(\frac{c_p - c_v}{c_p}\right)^2 \frac{2\Gamma_R/\pi}{(2\Gamma_R)^2 + \omega^2}$$

$$+ \langle i_s \rangle^2 \left(\frac{c_p}{c_v}\right)^2 \frac{1}{4}\left[\frac{2(2\Gamma_B)/\pi}{(2\Gamma_B)^2 + \omega^2} + \frac{2\Gamma_B/\pi}{(2\Gamma_B)^2 + (\omega \pm 2\omega_B)^2}\right]$$

$$+ \langle i_s \rangle^2 \left(\frac{c_p - c_v}{c_p}\right)\left(\frac{c_v}{c_p}\right)\left[\frac{(\Gamma_R + \Gamma_B)/\pi}{(\Gamma_R + \Gamma_B)^2 + (\omega \pm \omega_B)^2}\right] \qquad 2.16$$

This may be simplified using the following:(41)

$$\Gamma_R \sim \epsilon^{\gamma - \psi}, \qquad \Gamma_B \sim \epsilon^{-(\gamma - \alpha)}$$

$$\psi \approx 0.6 \qquad \gamma \approx 1.2 \qquad \alpha \approx 0.1$$

$$\Gamma_B \gg \Gamma_R \xrightarrow[T \to T_c]{} 0$$

$$c_v/c_p \sim \epsilon^{\gamma - \alpha} < 1 \qquad (c_v/c_p)^2 \ll 1$$

$$\left(\frac{c_p - c_v}{c_p}\right)^2 \Gamma_R \sim \epsilon^{3\gamma - 2\alpha - \psi} \xrightarrow[T \to T_c]{} 0$$

(note: even at $\Delta T = 5^{\circ}C$, for the largest angle of the present experiment, 2.7° (air), Γ_R is only 1.6% of Γ_B).

With these approximations, 2.16 reduces to:

$$\langle i_s \rangle^2 \delta(\omega) + \langle i_s \rangle^2 \left(\frac{c_p - c_v}{c_p}\right)\left(\frac{c_v}{c_p}\right) \frac{\Gamma_B/\pi}{\Gamma_B^2 + (\omega \pm \omega_B)^2} \qquad 2.17$$

Let us now return to 2.11 and examine the last term:

$$\frac{i_{LO}\langle i_s \rangle}{2\pi} \int_{-\infty}^{\infty} e^{i\omega\tau}\left[e^{i\omega_{LO}\tau} g_s^{(1)}(\tau) + e^{-i\omega_{LO}\tau} g_s^{(1)*}(\tau)\right] d\tau$$

which with 2.12 becomes:

$$\frac{i_{LO}\langle i_s \rangle}{2\pi} \int_{-\infty}^{\infty} e^{i\omega\tau}\left[e^{i\omega_{LO}\tau} e^{-i\omega_0\tau} f(\tau) + e^{-i\omega_{LO}\tau} e^{i\omega_0\tau} f(\tau)\right] d\tau$$

$$= \frac{i_{LO}\langle i_s \rangle}{2\pi} \int_{-\infty}^{\infty} e^{i(\omega \pm \omega_{LO} \mp \omega_0)\tau} f(\tau)\, d\tau$$

but $\omega_{LO} = \omega_o$ so the preceding line becomes:

$$\frac{i_{LO}\langle i_s\rangle}{\pi}\int_{-\infty}^{\infty} e^{i\omega\tau}\left(e^{-\Gamma_R\tau}\left(\frac{C_p-C_v}{C_p}\right)+\left(\frac{C_v}{C_p}\right)e^{-\Gamma_B\tau}\cos\omega_B\tau\right)d\tau$$

$$= i_{LO}\langle i_s\rangle\left(\frac{C_p-C_v}{C_p}\right)\frac{\Gamma_R/\pi}{\Gamma_R^2+\omega^2}+\frac{C_v}{C_p}\,i_{LO}\langle i_s\rangle\,\frac{\Gamma_B/\pi}{\Gamma_B^2+(\omega\pm\omega_B)^2}$$

Again, the term containing Γ_R is approximately zero so that there remains only:

$$\frac{C_v}{C_p}\;i_{LO}\langle i_s\rangle\;\frac{\Gamma_B/\pi}{\Gamma_B^2+(\omega\pm\omega_B)^2} \qquad 2.18$$

Putting together 2.17, 2.18 and the remaining terms of 2.11 the complete heterodyne power spectrum is:

$$P(\omega)=\frac{e}{2\pi}\left(\langle i_s\rangle+i_{LO}\right)+\delta(\omega)\left(i_{LO}^2+2i_{LO}\langle i_s\rangle\right)$$
$$+\delta(\omega)\langle i_s\rangle^2+\langle i_s\rangle^2\left(\frac{C_p-C_v}{C_p}\right)\left(\frac{C_v}{C_p}\right)\frac{\Gamma_B/\pi}{\Gamma_B^2+(\omega\pm\omega_B)^2}$$
$$+\frac{C_v}{C_p}\;i_{LO}\langle i_s\rangle\;\frac{\Gamma_B/\pi}{\Gamma_B^2+(\omega\pm\omega_B)^2}$$

Now the spectrum analyzer blocks d.c. and negative frequencies are folded into positive frequency space so that:

$$P(\omega)_{\omega>0}=\frac{e}{\pi}\left(\langle i_s\rangle+i_{LO}\right)+\frac{\Gamma_B/\pi}{\Gamma_B^2+(\omega-\omega_B)^2}\;2\,\frac{C_v}{C_p}\langle i_s\rangle$$
$$\times\left[\langle i_s\rangle\left(\frac{C_p-C_v}{C_p}\right)+i_{LO}\right] \qquad 2.19$$

This is the final expression for the heterodyne power spectrum expected for Brillouin scattering.[41,15]

2. Predetection Factors

The assumptions of the previous section will now be relaxed, and the influence of the measuring apparatus itself, and the properties of the fields, will be taken into account. The "detection" occurs on the photocathode surface the instant the LO and signal photons mix to produce the photoelectrons of the beat current. Anything that influences heterodyning before detection may be grouped into a predetection efficiency factor ,ϵ. In this category are polarization, spatial coherence of the fields over the photosurface, wavevector misalignment, field phase front mismatch, non-uniform quantum efficiency, and aberrations of optical components. After detection, factors affecting the power spectrum measurement are usually expressed in a signal to noise ratio (SNR). These factors include inherent detector noises (shot, thermal, dark, and background), gain of the detector, and the effect of finite time averages and signal enhancement.

In the following, each factor will be isolated from all others, and its influence on the heterodyne process will be considered assuming the remaining factors optimized.

a. Polarization

It is easy to deal with polarization effects. If the quantum efficiency of the photodetector is isotropic, η = constant, then the signal may be resolved into polarization components parallel, and perpendicular to, the LO field. Only the parallel signal component mixes with the LO. More generally, if the quantum efficiency is anisotropic, then the

signal is still resolvable into components parallel, and perpendicular to the vector product of the quantum efficiency tensor times the LO polarization. In such cases, it is possible for two orthogonal fields to beat together.[42] For isotropic quantum efficiency, the polarization efficiency factor varies as $\epsilon_{pol} = \cos\theta$ (2.20) $(0 \leq \theta \leq \pi/2)$ where θ is the angle between $\vec{E}_{LO}$ and $\vec{E}_s$. It is maximum for completely parallel fields, and zero for orthogonal fields. For anisotropic η, the efficiency must be computed point by point over the detector area.

b. Spatial Coherence

Consider now signal spatial correlation effects. Previously, the fields were taken to be completely spatially coherent, and all position variables were dropped. The correlation function expression (2.10) neglecting the shot noise and d.c. terms, and assuming that the LO intensity is much greater than the signal intensity so that $g_s^{(2)}(\tau)$ may also be neglected, is:

$$e^2\eta^2 I_{LO}\left(e^{-i\omega_{LO}\tau}\langle E_s(t)E_s^*(t+\tau)\rangle + \text{complex conjugate}\right)$$

Now recall that the current from the detector is the current density integrated over the surface area of the detector, and putting back the spatial dependences obtain:

$$e^2\eta^2\iint\langle E_{LO}(\vec{r}+\vec{\rho})\,E_{LO}(\vec{r})\left[e^{-i\omega_{LO}\tau}\langle E_s(\vec{r},t)E_s^*(\vec{r}+\vec{\rho},t+\tau)\rangle + c.c.\right]d\vec{r}\,d\vec{\rho}$$

where $\vec{\rho}$ is the position vector relative to the fixed reference point $\vec{r}$ on the detector surface. Generally $\langle E_s(\vec{r},t)E^*_s(\vec{r}+\vec{\rho},t+\tau)$ cannot be factored into separate time and spatial parts. However, if the largest dimension of the photocathode surface is

small compared to the wavelength of the beat signal, then the small time delay between the arrival of a given signal phase front at $\vec{r}$ and $\vec{r}+\vec{\rho}$ can be ignored. This condition is satisfied for the Brillouin signal of interest. The Brillouin frequency shifts (beat frequencies) are in the range of 1 - 100 MHz, thus wavelengths are 3 - 300 meters. The photocathode surface is only 2 inches in diameter. With this approximation, the two point, two time function may be factored into:[43]

$$\langle E_s(\vec{r},t)\, E_s^*(\vec{r}+\vec{\rho},t+\tau)\rangle = \mathcal{J}_s(\vec{r},\vec{\rho})\langle E_s^*(\vec{r},t+\tau)\, E_s(\vec{r},t)\rangle \qquad 2.21a$$

$$\mathcal{J}(\vec{r},\vec{\rho}) = \frac{\langle E^*(\vec{r}+\vec{\rho},t)\, E(\vec{r},t)\rangle}{\langle |E(\vec{r},t)|^2\rangle^{1/2}\langle |E(\vec{r}+\vec{\rho},t)|^2\rangle^{1/2}} \qquad 2.21b$$

$\mathcal{J}(\vec{r},\vec{\rho})$ is the complex degree of spatial coherence[44]; its modulus, $|\mathcal{J}(\vec{r},\vec{\rho})|$, is the degree of coherence which varies between zero (complete incoherence) and one (complete spatial coherence). Note that for the LO field of 2.7 the spatial coherence function is $I_{LO}\mathcal{J}_{LO}(\vec{r},\vec{\rho}) = \langle E_{LO}^*(\vec{r}+\vec{\rho})E_{LO}(\vec{r})\rangle$.

The spatial coherence efficiency factor may be defined as:

$$\epsilon'_{coh} = \int_A\int_A \mathcal{J}_{LO}(\vec{r},\vec{\rho})\,\mathcal{J}_s(\vec{r},\vec{\rho})\, d\vec{r}\, d\vec{\rho}$$

Since $\vec{r}$ is the position vector of a point on the detector with respect to the source as origin, both the LO and signal fields will be independent of $\vec{r}$ on the detector area, A, and:

$$\epsilon'_{coh} = A\int_A \mathcal{J}_{LO}(\vec{r},\vec{\rho})\,\mathcal{J}_s(\vec{r},\vec{\rho})\, d\vec{\rho}$$

This expression now depends only on the (lateral) spatial coherence of the LO and signal fields across A. For the moment, assume $|\mathcal{J}_{LO}(\vec{r},\vec{\rho})| = 1$. The remaining integral was

defined by Lastovka[45] as the coherence area:

$$A_{coh} = \int_{\vec{\rho}} \gamma_s(\vec{r}, \vec{\rho})\, d\vec{\rho} \qquad 2.22$$

It is the equivalent area around a given point on the photosurface over which the current densities produced by the beat signal are completely in phase. It is possible that $|\gamma_{LO}| < |\gamma_s|$ in which case γ_{LO} should replace γ_s in A_{coh} and $|\gamma_s| = 1$. The limiting forms for ϵ'_{coh} are:

$$\epsilon'_{coh} = \begin{cases} A\, A_{coh} & A \gg A_{coh} \\ A^2 & A \ll A_{coh} \end{cases}$$

The expression for A_{coh} may be difficult to evaluate. Siegman showed the heterodyne receiver could be considered as an antenna and as such had an effective capture cross section. He showed the integrated effective aperture to be:[46]

$$\int A(\vec{\Omega})\, d\vec{\Omega} \approx \lambda^2$$

where $A(\vec{\Omega})$ is an expression for the geometry of the area in spherical coordinates. For constant photosurface area, $A(\vec{\Omega})$ = A and if the aperture is integrated over all possible arrival directions from the source, then:

$$A\,\Omega \approx \lambda^2 \qquad 2.23$$

If Ω_{coh} is taken to be the angle subtended by the source at the heterodyne receiver, then the optimal area is $A_{coh} \approx \lambda^2/\Omega_{coh}$. This is the same expression originally employed by Forrester[47] and used by Cummins and Swinney[36] to calculate the number of coherence areas.

A normalized efficiency may be obtained by dividing ϵ'_{coh}

by A^2:

$$\epsilon_{coh} = \begin{cases} 1 & A \ll A_{coh} \\ A_{coh}/A & A \gg A_{coh} \end{cases} \qquad A_{coh} \approx \lambda^2/\Omega_{coh} \qquad 2.24$$

c. Angular Misalignment

Consider the LO and signal fields to be plane waves with the LO wavevector incident normally to the detector surface, and the signal wavevector inclined at some angle ϕ to the surface normal. Then interference fringes between the two fields are formed on the detector with phase variation of the form $\exp(i\phi kx)$ at position x. The periodicity is λ/ϕ and the number of fringes is about $\phi L/\lambda$ where L is a characteristic detector size. Then over the detector the beat signal must vary in amplitude by:[48]

$$\left| \frac{1}{L} \int_0^L e^{ik\phi x}\, dx \right| = \frac{\sin \pi \phi L/\lambda}{\pi \phi L/\lambda}$$

This function has zeroes at multiples of $\pi/2$. A useful criterion for angular misalignment is:

$$-\pi/2 \le \frac{\pi \phi L}{\lambda} \le \pi/2 \qquad 2.25$$

$$|\phi| \le \lambda/(4L)$$

From this requirement, the misalignment factor can be written as:

$$\epsilon_{Align} = \frac{\sin(KL \sin\phi)}{KL \sin\phi} \qquad 2.26$$

d. Wavefront Radius Mismatch

Lastovka[66] has analyzed this effect in detail. Even though the LO and signal wavevectors may be exactly collinear,

the phase fronts at the detector surface might not coincide due to a difference in radii of curvature. The efficiency factor again takes the form of sinx/x:

$$\epsilon_{RAD} = \frac{\sin X}{X} \qquad X = \frac{\pi}{4\lambda}\left(\frac{R_S - R_{LO}}{R_S R_{LO}}\right) L^2 \qquad 2.27$$

where R_{LO}, R_s are the radii of curvature of the LO and signal, and L is again the characteristic dimension of the detector. This function is optimal when:

$$X \leq \lambda/(8L)$$

$$|R_{LO} - R_S| \leq \lambda (R_{LO} R_S) L^2 \qquad 2.28$$

e. Optical Losses

It is not necessary that the receiver aperture and detector surface coincide. All analysis is the same when the receiver aperture is imaged on the photosurface by mirrors or lenses, provided significant wavefront distortion is not introduced by these elements. Less obvious is the result of Mandel & Wolf[48] that a detector at the focal plane of an optical system differs only by a phase factor and multiplicative constant from the case of the receiver and aperture coinciding. This is due to the conjugate Fourier transform relation between the fields at the aperture and detector surface.

For distinct optical elements the optical efficiency factor is again a sinx/x function. The wavefront distortion introduced by any single element is given by:[67]

$$\epsilon_{DIST} = \frac{\sin 2\pi \lambda^*/\lambda}{2\pi \lambda^*/\lambda} \qquad 2.29$$

where λ^* is the wavefront distortion over the detector length L. This leads to a surface figure tolerance of:

$$-\pi/2 \leq \frac{2\pi\lambda^*}{\lambda} \leq \pi/2 \quad \text{or} \quad |\lambda^*| \leq \lambda/8 \qquad 2.30$$

Becker et al[49] found a 5 - 10 db decrease in the beat signal of a heterodyne interferometer due to wavefront distortion introduced by an optical attenuator. High quality optics must be used in these and laser anemometer configurations using many components.

f. Effect of Field Distribution

In the analysis of spatial coherence, the fields of the LO and signal were assumed uniform across the detector surface. This is achieved when the beam cross sectional areas are infinitely large, or in practice, with beams large compared to the detector area. For finite beam cross sections, the electric field spatial distribution functions of the LO and signal will affect the heterodyne efficiency.

The interesting case of Gaussian LO and signal electric fields was analyzed by Lathi.[50] The ϵ of the photocurrent depended on the cross sections of the LO and signal beams, their coherence areas, and of course the detector area. Parameters called effective coherence area and effective cross sectional area were defined as:

$$a_{eff} = \frac{a_s a_{LO}}{a_s + a_{LO}} \qquad A_{eff} = \frac{A_s A_{LO}}{A_s + A_{LO}}$$

where a_s, a_{LO} and A_s, A_{LO} are the coherence areas and beam cross sections associated with the signal and LO. For imper-

fect spatial coherence the optimum ϵ was obtained by making:

$$A_{LO} = \frac{A_s}{(1 + 4A_s/a_{eff})^{\frac{1}{2}}} \qquad = A_s Q \qquad (Q < 1)$$

and ϵ depended on the receiver area A as:

$$\epsilon = \frac{(2Q)^2}{(1+Q)^2} \; A_s \; (1 - \exp(-A/(A_s Q)))$$

The general criteria for best heterodyne efficiency for partially coherent fields are: $A_{LO} = A_s Q$, $a_{LO} \gg a_s$, and A should be as large as possible. It is assumed that the spatial characteristics are known and not adjustable, but the LO parameters are variable. If $A_{LO} > A_s Q$, ϵ was found to degrade in general. This arises if the LO characteristics cannot be varied, and in such cases A should be adjusted to optimize the efficiency. For $A_{LO} > A_s Q$, the best A could be found from the numerical solution of:

$$\frac{\exp(A/A_{LO}) - 1}{\exp(A/(2A_{eff})) - 1} = \frac{A_{eff}}{A_{LO}}$$

For $a_{eff} = A_s = A_{LO}$ the optimum detector area was $A \simeq 2A_s$ whereas for $a_{eff} = 5A_s$, optimum $A \simeq 5.2A_s$.

These results can be understood by considering the case of perfect spatial coherence. Then $a_s = a_{LO} \to \infty$, $a_{eff} \to \infty$, and the optimum $A_{LO} = A_s$. Thus the radial distribution functions of the fields should match in amplitude and spatial phase. If $A_{LO} > A_s$, then the portion of A_{LO} outside of A_s adds incoherently to the signal, noise is greater, and the SNR degrades.

The partial coherence results express the conditions for maximum overlap given A_s.

Fink[51] considered the LO and signal radial distributions to be matched Airy functions incident on a circular detector. The efficiency was a monotonically increasing function of the detector area,

$$\epsilon = 1 - J_o^2(x) - J_1^2(x) \qquad E_{LO}(r) = C_{LO} 2J_1(x)/x$$

$$X = \pi r/(F\lambda) \qquad E_s(r) = C_s\, 2J_1(x)/x$$

where J_o, J_1 are Bessel functions, r the field radius, and F the f/# of the optical system. For a detector the same size as the Airy spot size, $\epsilon = 0.84$, and the efficiency approaches unity as $r_{det} \to \infty$.

Fink[51] also considered a uniform LO and Airy function signal and,

$$\epsilon = 4(1 - J_o(x))^2/x^2$$

which has a maximum value for x = 2.75 corresponding to a detector radius only 72% of the Airy spot radius (radius of Airy spot = $1.22\lambda F$). If the detector size increased to the Airy spot size, $\epsilon = .54$.

Degnan & Klein[52] and Cohen[53] both considered a Gaussian LO and Airy signal:

$$E_s(r) = C_s J_1(x)/X$$

$$E_{LO}(r) = C_{LO}\int_o^{x_o} \exp(-z^2) \qquad z = r/w$$

where w is the (1/e) waist radius. The efficiency is a complicated function which must be evaluated numerically:

$$\epsilon = 2\left[\frac{2Z/X_o \int_o^{X_o} J_1(X)\, J_o(2F\phi X)\, e^{-(X^2/X_o^2)Z^2}\, dX}{(1 - e^{-2Z^2})}\right]^2$$

with ϕ the misalignment angle. For perfect alignment, $x_o, z \to \infty$ such that x_o/z remains finite:

$$\epsilon = \frac{8}{x_o^2} Z^2 \left[1 - e^{-x_o^2/(2Z)^2} \right]^2$$

which has a maximum for $w/F = .71\lambda$ and for which $\epsilon_{max} = .82$.

Mandel & Wolf[48] chose a uniform LO and spherical signal wave:

$$E_s(r) = C_s \frac{e^{iK(r^2+Z^2)^{1/2}}}{(r^2+Z^2)^{1/2}} Z$$

The evaluation of the efficiency for points far from the detector, $Z >> L$ showed that:

$$\epsilon = \sin x/x \qquad x = \tfrac{1}{4}kL^2/Z$$

with the first maximum occurring for $kL = 0.68$ when $Z = 10^9/k$.

It is clear that there is no simple expression for the heterodyne efficiency when the LO and signal radial field distribution functions are not the same; each case must be examined separately. These mixed field results are particularly important in Laser Doppler Anemometry, heterodyne interferometry, and heterodyning in astronomy where the LO and signal fields are definitely known to be different but where one or both cannot be varied to maximize the efficiency.

An interesting theoretical result for an active heterodyne receiver was derived by Fink and Vodopia[54]. They considered an array detector where individual detectors were small enough such that the fields of the LO and signal and their spatial phase difference Φ, were effectively constant across each detector. If each detector had its own IF

amplification $G_j = GE_j$ and phase shift ψ_j which could be varied, then the efficiency could be maximized if:

$$\left| \frac{E_s}{E_{LO}} \right| = E_j \text{ and } \psi_j = \text{constant} - \Phi$$

Advantages include matching the LO field distribution to the signal, compensation for misalignment, optical distortions, wavefront radius mismatch, and provision for a variable detector area. The efficiency could be optimized for each signal.

g. Nonuniform η

Only Cohen[53] has considered the effect of nonuniform quantum efficiency. The form,

$$\eta(r) = \eta_0 \left(\alpha - \beta (r/r_0)^2\right)$$

where r_o is a reference point on a circular detector, and α, β are constants was considered. Varying α, β for Airy signal and uniform LO, the best value for the detector radius varied as much as 30% from a detector with η constant. For uniform signal and Gaussian LO, ϵ was always higher for $\alpha = \beta = 1$ than for constant η. Generally, nonuniform should be avoided unless each field distribution is known and the detector geometry is simple. When both fields are uniform, ϵ is just the geometrically averaged η.

h. Overall Heterodyne Efficiency

The total efficiency is the product of the individual efficiencies:

$$\epsilon_{tot} = \prod_{i=1}^{6} \epsilon_i$$

and includes: 1) polarization, 2) coherence area, 3) misalignment, 4) wavefront radius mismatch, 5) optical losses, and 6) field distributions. If η is nonuniform, then the fields must be averaged over the detector geometry, with $\eta(x,y)$ a weighting factor.

The signal term in the power spectrum expression should be multiplied by this total factor. Thus, for the Brillouin beating power spectrum, eqn 2.19 : 2.31

$$P(\omega) \underset{\omega>0}{=} \frac{e}{\pi}\left(\langle i_s\rangle + i_{LO}\right) + \frac{2\Gamma_B/\pi}{\Gamma_B^2+(\omega-\omega_B)^2}\,\frac{C_v}{C_p}\langle i_s\rangle\left[\frac{C_p-C_v}{C_p}\langle i_s\rangle\epsilon_1 + i_{LO}\epsilon_2\right]$$

Since there are effectively two local oscillators, there should be two efficiencies.

3. Postdetection Factors

a Shot Noise Domination

The detector used in the present experiment was a photomultiplier tube (PMT) and its inherent noise sources are dark current, radiation background noise, internal thermal noise, and the shot noises from the signal and local oscillator. Dark current, background, and shot noise are all Poisson distributed events. They are all due to fluctuation in the photoelectron rate, in the thermionic emission from the photocathode. These four noise sources all follow the shot noise formula:(55)

$$i^2_{noise} = 2\,Bie$$

where e is the electronic charge, B is the bandwidth of the detector, i the current, and i^2_{noise} the mean square noise current. Thermal noise follows Nyquist's mean square noise

voltage expression; the power is:[56]

$$P_{thermal} = kTB$$

where k is Boltzmann's constant, and T the absolute temperature.

The ratio of signal power to signal plus noise power (SNR) becomes:

$$SNR = \frac{i_s^2 R}{kTB + 2eBR(i_d + i_b + i_s + i_{LO}) + i_s^2 R}$$

where i_s, i_d, i_b, i_{LO} are the signal, dark, background, and LO currents. This SNR is for the case of no internal gain. For a power gain of G, one has $i^2 = G(i')^2$ where the prime indicates the quantum efficiency limited photoelectron emission. For gain G,

$$SNR = \frac{(i'_s)^2 R}{kTB/G + 2eBR(i'_d + i'_b + k'_s + i'_{LO}) + (i'_s)^2 R}$$

The gain does not affect the thermal noise current. Since gains of order of 10^6 are typical in a PMT, the thermal noise contribution becomes negligible compared to the shot noises, and greater sensitivity is achieved.

Now in light mixing, the addition of the LO to the signal achieves correlation within the detector. Since the LO amplitude can be made quite large (usually), it provides sufficient conversion gain so that the shot noise from it dominates all other noise sources. However, because of the shot noise generated by the LO, the LO power should be the minimum

necessary to achieve this domination. Since thermal noise is already negligible for the PMT with power gain, the requirement on the LO power is that it be large enough so that its shot noise is greater than either dark current or background noise.

Consider the signal to background ratio only:

$$i_s^2/i_b^2 = \frac{i_{LO}\, i_s}{i_b^2} = \frac{\eta e P_{LO}\, i_s/(h\nu)}{2 e B\, i_b} = \frac{\eta e P_{LO}\, i_s/(h\nu)}{2 e B \eta e P_b/(h\nu)}$$

$$= (P_{LO}/P_b)\; i_s/(2eB)$$

which, since $i_s = 2eB$ at least, gives

$$i_s^2/i_b^2 = P_{LO}/P_b$$

If the output signal power is to be considerably greater than the background power, then for example:

$$i_s^2/i_b^2 = P_{LO}/P_b > 100$$

Note that η does not enter because the LO and background input powers influence the LO and background output powers in a square root dependence.

The thermal background noise power for a receiver of area A and collection angle Ω is:[57]

$$P_b = \frac{\Omega A}{\lambda^2} \frac{h B \nu}{\exp(h\nu/kT) - 1}$$

where B is again the bandwidth, and which for $A\Omega \approx \lambda^2$ and $h\nu \gg kT$, becomes:

$$P_b = h\nu B \exp(-h\nu/kT)$$

For B = 500 kHz, T = 300°K, and optical frequencies (10^{14} Hz), $P_b = 3.9 \times 10^{-21}$ W, a condition easily fulfilled using a laser source. The SNR for LO powers that cannot fulfill this

condition has been considered by Abbas et al[58] for use in IR heterodyne detection of astronomical sources.

Now consider the signal to dark current ratio only:

$$\frac{i_s}{i_d^2} = \frac{i_{LO}\, i_s}{2eB\, i_d} = \frac{i_{LO}}{i_d} > 100$$

Thus, $P_{LO} \geq h\nu/(\eta e)\ 100\ i_d$, and the required power depends on the quantum efficiency. For optical frequencies, $\eta = 0.1$, and $i_d = 3\text{X}10^{-9}$A (typical values for actual PMT used), $P_{LO} \geq 1.2\text{x}10^{-6}$W.

Thus, the dark, background, and thermal noise can all be neglected compared to the LO shot noise provided the LO power is greater than about 1 μW. In the discussion to follow, only the signal and LO shot noises will be included.

b. Effects of Signal Processing

The SNR neglecting all noise sources other than the shot noise from the LO and signal itself is:

$$SNR = \frac{(i_s')^2 R}{2eBR(i_s' + i_{LO}') + (i_s')^2 R} = \frac{P_s(\omega)}{P_s(\omega) + P_{SHOT}}$$

where now the frequency dependence of the signal is displayed explicitly To proceed further, one must describe the signal processing electronics following the PMT. Briefly these were a spectrum analyzer with variable IF filter and detector, an RC integrating filter, analog-to-digital converter (A-D conv.), multi-channel scaler (MCA), and finally computer. A block diagram is shown in figure 2.1.

Detailed analyses[45,36] of similar processing electronics showed that the most important quantities were the IF

Figure 2.1: Block diagram of signal processing electronics.

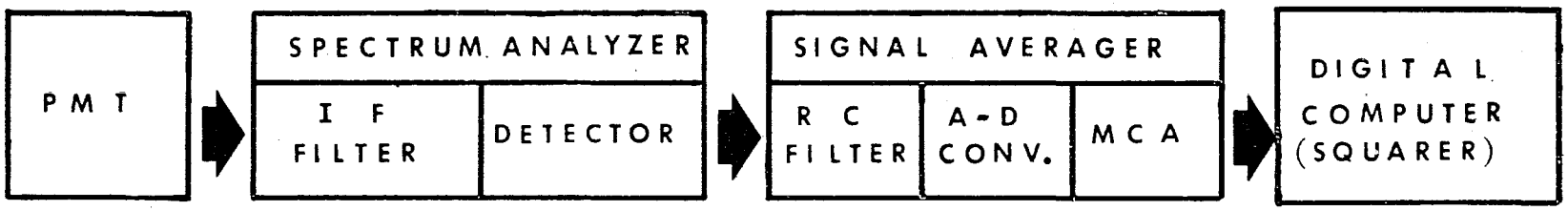

SIGNAL PROCESSING ELECTRONICS

filter width, and the width of the RC filter, but not their lineshapes. The basic reason for this is the fact that measurements are performed in finite time intervals, not in the infinitely long (ensemble) averages of theoretical predictions. Since the observed spectrum always exhibits fluctuations, limitations in the precision with which the signal can be determined are imposed. Only the filter time constants influence the SNR. The lineshapes of the filters will influence the determination of the signal linewidth, however.

For the configuration of figure 2.1 the following points should be noted. The spectrum analyzer has a number of IF filters. A detailed analysis of the lineshapes of these filters showed them to be well fitted by Voigt functions (Chapter IV). However, this Voigt function is, in each case, mostly Gaussian in character. To good approximation, the total width can be taken to be the Gaussian width. In addition, one should note that at this stage of processing, one is making a random noise measurement. Noise is usually specified by the noise power bandwidth. It is defined as the ideal rectangular filter bandwidth with the same power response as the actual IF filter.[59] For Gaussian shaped filters, the noise power bandwidth is approximately 1.2 times the 3db bandwidth. Thus, the noise power bandwidth can be used to simplify calculations since it is a rectangular function; the actual numerical value used for the width will be 1.2 times the Gaussian width (FWHM).

The detector in the spectrum analyzer produces a voltage (not voltage squared) versus frequency. However, a

computer is used to square the voltage digitally to give the power spectrum. Though the squaring takes place at a later stage, the result is equivalent to detection and squaring together. The stages of processing described here are convolution operations, and convolution is a distributive operation. Thus, the configuration described here is equivalent to the other analyses,[36,45] except for the addition of signal averaging.

The A/D converter makes the averaging and numerical squaring possible. The digitizing noise introduced will be neglected, since this was only 0.2% (9 bits), which is much less than other noise sources. Squaring in the computer is noise free.

Signal averaging is easy to account for. In view of the statistics of the measurement, the SNR will be enhanced by the square root of the number of sweep cycles.

c. IF Filter

In circuit analysis, the passage of a signal through a linear element is described by:[60]

$$P_{OUT}(\omega) = |H(\omega)|^2 \, P_{IN}(\omega) \qquad 2.32$$

where $P(\omega)$ is the power spectral density and $H(\omega)$ is the transfer function. The impulse response $h(\tau)$ is related to $H(\omega)$ by Fourier transformation:[61]

$$h(\tau) = \frac{1}{2\pi} \int_{-\infty}^{\infty} H(\omega) \, e^{i\omega\tau} \, d\omega \qquad 2.33$$

If the output for the PMT is represented simply as $P(\omega) = P_s(\omega) + P_{shot}$, then for the noise power bandwidth δ of the spectrum analyzer:

$$P_{IF}(\omega) = \begin{cases} P_S(\omega) + P_{SHOT} & -\delta/2 \le \omega \le \delta/2 \\ 0 & \text{otherwise} \end{cases} \qquad 2.34$$

d. Detector and Squarer

The detector in the spectrum analyzer is usually a diode whose instantaneous voltage is given by $V_D(t) = Ki_D^2(t)$, where K is a transfer constant. For a square law device, the output power spectrum, $P_o(\omega)$ for an input power spectrum $P_I(\omega)$ can be shown to be:[62]

$$P_o(\omega) = K^2 \int_{-\infty}^{\infty} P_I(\omega')\left(P_I(\omega'+\omega) + P_I(\omega'-\omega)\right) d\omega' + \langle V_o(t)\rangle^2 \delta(\omega) + \frac{e}{2\pi}\langle V_o(t)\rangle \qquad 2.35$$

where the convolution integral is the a.c. term, and the remaining terms are the d.c. and shot noise terms, respectively. Using 2.34 and neglecting the d.c. and shot noise, obtain from 2.35:

$$P(\omega) = 2K^2\left(P_S(\omega) + P_{SHOT}\right)^2(\delta - \omega) \qquad 2.36$$

e. RC Filter

Passing this power spectrum (2.36) through a simple RC filter which has a transfer function:[63]

$$\left|H_{RC}(\omega)\right|^2 = \frac{(1/\tau)^2}{\omega^2 + 1/\tau^2} \qquad \tau = RC$$

and using 2.32, we obtain:

$$P(\omega) = 2K^2\left(P_S(\omega) + P_{SHOT}\right)^2(\delta - \omega)\,\frac{1/\tau^2}{1/\tau^2 + \omega^2} \qquad 2.37$$

One can now obtain the SNR at the output of the integrating filter, but before signal averaging. At this point the signal is still analog so that:

$$SNR = \frac{\langle V(t)\rangle}{\langle |V(t)_{Ac}|^2\rangle^{1/2}}, \quad \langle |V(t)_{Ac}|^2\rangle = \langle |V(t) - \langle V(t)\rangle|^2\rangle$$

Further, using Parseval's theorem[64], we obtain:

$$\int_{-\infty}^{\infty} P(\omega)\, d\omega = \langle |V_{AC}(t)|^2 \rangle \qquad 2.38$$

which relates the power spectral density to the mean square fluctuations in the total voltage output. With 2.36, 2.37 becomes:

$$\langle |V(t)|^2 \rangle = 2K^2 \left(P_S(\omega) + P_{SHOT}\right)^2 (\delta/\tau)\, TAN^{-1}(\delta\tau) - (\delta\tau)^2 \ln(1+(\delta\tau)^2)$$

For $1/\tau \ll \delta$

$$\langle |V(t)|^2 \rangle \approx K^2 \left(P_S(\omega) + P_{SHOT}\right)^2 (\delta/\tau)\, \pi$$

$$\langle V(t) \rangle = K\left(P_S(\omega) + P_{SHOT}\right)\delta \quad \langle V(t) \rangle_{signal} = K P_S(\omega)\, \delta$$

$$SNR = \frac{K P_S(\omega)\, \delta}{\pi^{1/2} K \left(P_S(\omega) + P_{SHOT}\right)\left(\frac{\delta}{\tau}\right)^{1/2}} = \frac{P_S(\omega)}{P_S(\omega) + P_{SHOT}} \left(\frac{\delta\tau}{\pi}\right)^{1/2}$$

Now $P_s(\omega)/P_{shot}$ was found earlier. Examining 2.19 find,

$$\frac{P_S(\omega)}{P_{SHOT}} = \left(\frac{C_V}{C_P}\right) \langle i_S \rangle \frac{2\Gamma_B/\pi}{\Gamma_B^2 + (\omega - \omega_B)^2} \left(\langle i_S \rangle \epsilon_1 \frac{C_P - C_V}{C_P} + \epsilon_2 i_{LO} \right) \Big/ \frac{e}{\pi}\left(\langle i_S \rangle + i_{LO}\right)$$

which includes the overall heterodyne efficiency factors, ϵ_1, ϵ_2. This may be simplified, since $(C_p - C_v)/C_p \approx 1$, and if $\epsilon_1 = \epsilon_2 = \epsilon$ to:

$$\frac{P_S(\omega = \omega_B)}{P_{SHOT}} \approx 2\epsilon \frac{C_V}{C_P} \frac{\langle i_S \rangle}{e\Gamma_B}$$

Therefore,

$$SNR_{MAX} = \left(\frac{\delta\tau}{\pi}\right)^{1/2} 2\epsilon \frac{C_V}{C_P} \frac{\langle i_S \rangle}{e\Gamma_B} \Big/ \left(1 + \frac{C_V}{C_P} \frac{2\epsilon \langle i_S \rangle}{e\Gamma_B}\right) \qquad 2.39$$

since the maximum value of $P_S(\omega)$ occurs at $\omega = \omega_B$.

f. Signal Averaging

Signal averaging consists of sampling a repetitive signal at fixed time intervals, A/D conversion, and storing the sampled values in separate locations of memory. Signals which are not repetitive or are continuous, can be made repetitive by using an accurate synchronizing signal to start each sampling period. This is usually provided by the averager itself. The sampling theorem[65] requires that the sampling rate be at least greater than twice the highest frequency of interest. During a sampling sweep, each value is stored in memory with each location corresponding to a definite sample time. After a given number of sweeps, the sum stored in each location is equal to the number of repetitions times the average of the samples at that point of the signal waveform. The averager passes all frequencies in phase so that the original waveform is extracted. Noise adds randomly at each sample point, but the signal adds constantly. The SNR is enhanced since after M sweeps, the signal content is M times the single sweep signal, but the noise is only $M^{\frac{1}{2}}$ times the single sweep noise. Thus, a gain of $M^{\frac{1}{2}}$ in SNR is achieved. The signal averager is a digital device where $M = 2^n$ with $0 \leq n \leq 19$ typically.

Thus the last expression for the SNR 2.39 should be multiplied by $M^{\frac{1}{2}}$:

$$SNR_{MAX} = \sqrt{\frac{\delta\tau}{\pi}} \left[\frac{2\epsilon \frac{c_v}{c_p} \langle i_s \rangle / (T_B e)}{1 + 2\epsilon \frac{c_v}{c_p} \langle i_s \rangle / (T_B e)} \right] \sqrt{m} \qquad 2.40$$

ϵ = overall heterodyne efficiency
δ = IF Filter bandwidth
τ = RC Filter time constant
T_B = Brillouin Linewidth
e = electronic charge
$\langle i_s \rangle$ = mean photocurrent due to total signal from sample
m = number sweeps of signal averager

The total average current is i_{LO} plus $\langle i_s \rangle$. In fluids far from T_c, $i_{LO} > \langle i_s \rangle$, while near T_c, $\langle i_s \rangle$ becomes comparable to or even greater than i_{LO} because of the enhanced Rayleigh scattering. Note further that the specific heat ratio becomes much greater than unity near T_c, so that:

$$\frac{P_s(\omega = \omega_B)}{P_{SHOT}} = 2\epsilon \left(\frac{C_v}{C_p}\right) \frac{\langle i_s \rangle}{e T_B}$$

becomes small and SNR_{max} is approximately,

$$SNR_{MAX} = \sqrt{\frac{\delta \tau m}{\pi}} \quad \frac{2\epsilon \langle i_s \rangle}{e T_B} \quad \frac{C_v}{C_p} \qquad 2.41$$

An estimate of ϵ and SNR for the present experiment will be given in the next chapter.

References for Chapter II

1. D. Sette, in Physics of Simple Liquids (North Holland, Amsterdam, 1968), p. 325.

2. J. L. Kline and E. F. Carome, J. Chem. Phys. 58, 4962 (1973).

3. P.E. Mueller, D. Eden, C.W. Garland and R.C. Williamson, Phys. Rev. A 6, 2272.

4. C.W. Garland and R.D. Williams, Phys. Rev. A 10, 1328 (1974).

5. R.C. Williamson and D. Eden, J. Acous. Soc. Am. 47, 1278 (1970).

6. C.W. Garland, D. Eden and L. Mistura, Phys. Rev. Lett. 25, 1161 (1970).

7. J. Thoen and C. W. Garland, Phys. Rev. A10, 1311 (1974).

8. A.G. Chynoweth and W.G. Schneider, J. Chem. Phys. 20, 1777 (1952).

9. H.Z. Cummins and H.L. Swinney, Phys. Rev. Lett. 25, 1165 (1970).

10. M. Hercher, Appl. Opt. 7, 951 (1968).

11. D.S. Cannell and G. Benedek, Phys. Rev. Lett. 25, 1157 (1970).

12. M. Born and E. Wolf, Principles of Optics 4th Ed., p.363 (Pergamon, London, 1970).

13. D.S. Cannell, Ph. D. Thesis, M.I.T., 1970 (unpublished).

14. Hewlett Packard 1978 Electronic Instruments and Systems, (Hewlett Packard, Palo Alto, CA., 1978).

15. D. Eden and H.L. Swinney, Opt. Comm. 10, 191 (1974).

16. R.D. Mountain, Rev. Mod. Phys. 38,205 (1966).

17. Ref. 16, p. 213.

18. P. A. Fleury and J.P. Boon, in Advances in Chemical Physics vol. XXIV (Wiley, New York, 1973), p. 21.

19. H.L. Swinney, in Photon Correlation and Light Beating Spectroscopy, ed. by H.Z Cummins and E.R. Pike (Plenum, New York, 1974), p. 345.

20. Ref. 16, p. 208.

21. L. D. Landau and E.M. Lifschitz, Fluid Mechanics, sec. 78 (Addison-Wesley, Reading, 1959).

22. R. Zwanzig, J. Chem. Phys. 43, 714 (1965).

23. P. Lallemand, in Ref. 19, p. 251.

24. R.D. Mountain, J. Res. NBS 70 A, 207 (1966).

25. R.D. Mountain and T. A. Litovitz, J. Acous. Soc. Am. 42, 516 (1967).

26. N. Ostrowsky, in Ref. 19, p. 543.

27. P. Deguent and J.P. Boon, J. Chem. Phys. 54, 4443 (1971).

28. J.P. Boon and P. Deguent, Phys. Rev. A 2, 2542 (1970).

29. Ref. 18, p. 22.

30. C.J. Montrose, V.A. Solovyev and T.A. Litovitz, J. Acous. Soc. Am. 43, 117 (1968).

31. A.B. Bhatia and E. Tong, Can. J. Phys. 47, 361 (1969).

32. Ref. 24, p. 216; Ref. 18, p. 14.

33. Ref. 19, p. 372.

34. L. Mandel and E. Wolf, Rev. Mod. Phys. 37, 231 (1965).

35. H.Z. Cummins, in Ref. 19, p. 231.

36. H.Z. Cummins and H.L. Swinney, in Progress in Optics Vol. VIII (North Holland, Amsterdam, 1970), p. 133.

37. F.T. Arecchi, Phys. Rev. Lett. 15, 912 (1965).

38. Ref. 36, p. 145.

39. Ref. 36, p. 146.

40. C. Kittel, Elementary Statistical Physics, p. 133 (Wiley, New York, 1958).

41. Ref. 19, p. 373.

42. R.L. Smith, Appl. Opt. 3, 709 (1964).
A.J. Bahr, Proc. IEEE (Correspondence) 53, 513 (1965).

43. E. Jakeman, in Ref. 19, p. 111; Ref. 34.

44. O. Svelto, Principles of Lasers, p. 254 (Plenum, New York, 1976).

45. J.B. Lastovka, Ph. D. Thesis, M.I.T., 1967, p. 189.

46. A. E. Siegman, Appl. Opt. 5, 1588 (1966).

47. A.T. Forrester, R.A. Gudmundsen and P.O. Johnson, Phys. Rev. 99, 1691 (1955).

48. L. Mandel and E. Wolf, J.O.S.A. 65, 413 (1975).

49. R.A. Becker, S.W.C. Chang and M.W. Muller, Appl. Opt. 16, 1810 (1977); also J.N. Lathi, Appl. Opt. 8,1815 (1969).

50. J.N. Lathi and C.M. Nagel,Jr., Appl. Opt. 9, 115 (1970).

51. D. Fink, Appl. Opt. 14, 689 (1975).

52. J.J. Degnan and B.J. Klein, Appl. Opt. 13, 2397 (1974).

53. S.C. Cohen, Appl. Opt. 14, 1953 (1975).

54. D. Fink and S.N. Vodopia, Appl. Opt. 15, 453 (1976).

55. M. Ross, Laser Receivers, p. 55 (Wiley, New York, 1966).

56. Ref. 55, p. 57.

57. Ref. 55, p. 254.

58. M.M. Abbas, M.J. Mumma, T. Kostiuk and D. Buhl, Appl. Opt. 15, 427 (1976).

59. Hewlett Packard Appl. Note 150-4, p.7 (Hewlett Packard, Palo Alto, CA., 1974).

60. E.B. Magrab and D.S. Blomquist, Measurement of Time Varying Phenomena, p. 57 (Wiley, New York, 1971).

61. Ref. 60, p. 52-53.

62. Ref. 45, p.205.

63. Ref. 60, p.69.

64. Ref. 40, p.138.

65. Ref. 60, p.233.

66. Ref. 45, p.555.

67. Ref. 45, p.235.

CHAPTER III

EXPERIMENTAL INSTRUMENTATION

A block diagram of the entire laser Brillouin scattering experiment is shown in figure 3.1. Briefly, the xenon cell was placed in a precisely regulated heat bath and the temperature decreased from $10^{o}K$ above the critical temperature to $0.05^{o}K$ above the transition. A laser beam was sent through the single, gaseous-like phase which was scattered by the xenon and elastically scattered from the cell windows. Both the elastically scattered light and the Rayleigh line served as local oscillators for heterodyning. All the scattered light was collected by a lens and focussed on a photomultiplier. The photoelectric current was Fourier analyzed by a spectrum analyzer and accumulated in a signal averager.

Figure 3.1: Block diagram of experimental apparatus.

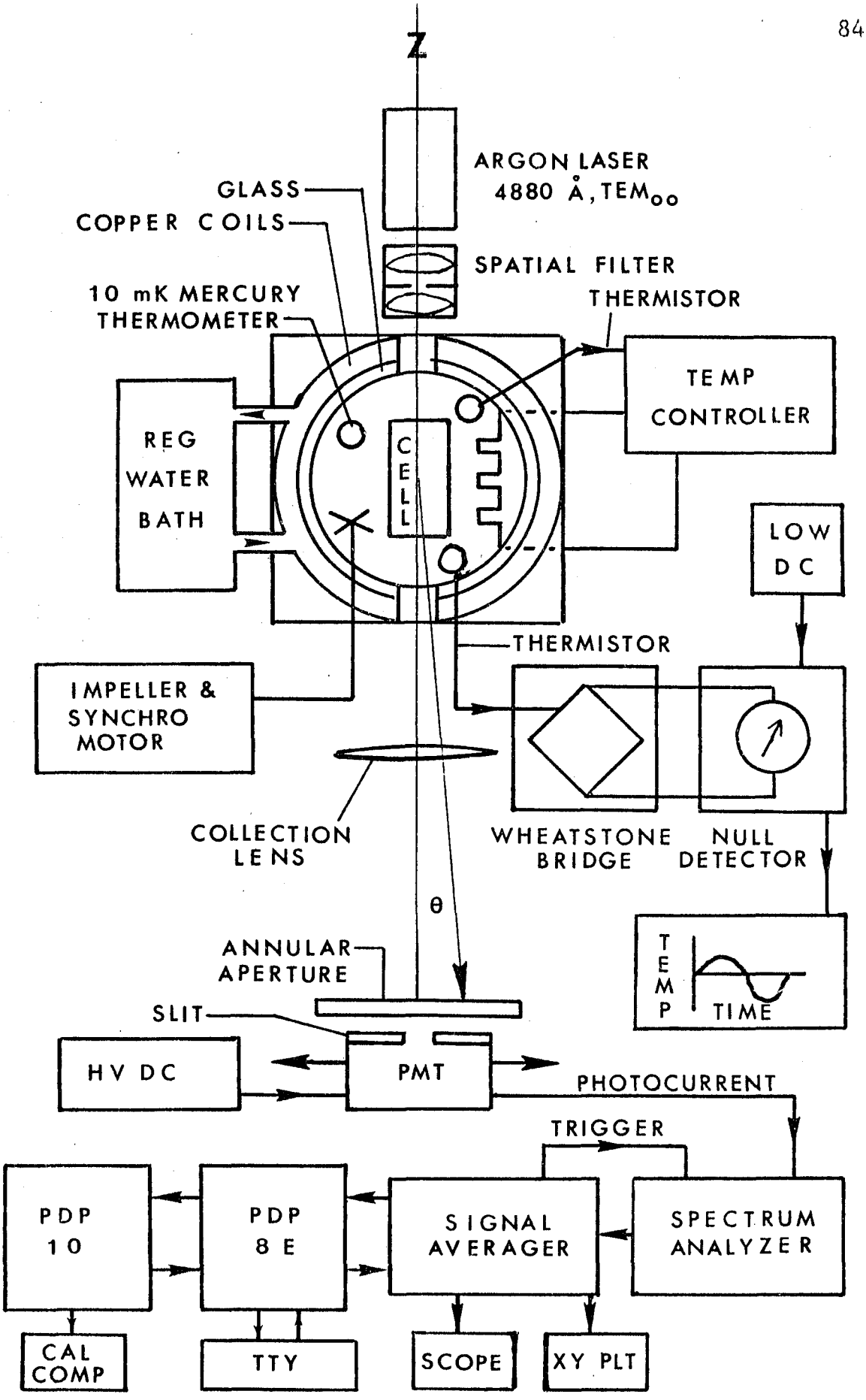
Z
ARGON LASER
4880 Å, TEM$_{oo}$
GLASS
COPPER COILS
SPATIAL FILTER
10 mK MERCURY
THERMOMETER
THERMISTOR
TEMP
CONTROLLER
REG
WATER
BATH
CELL
LOW
DC
THERMISTOR
IMPELLER &
SYNCHRO
MOTOR
COLLECTION
LENS
WHEATSTONE
BRIDGE
NULL
DETECTOR
θ
ANNULAR
APERTURE
TEMP
TIME
SLIT
HV DC
PMT
PHOTOCURRENT
TRIGGER
PDP
10
PDP
8 E
SIGNAL
AVERAGER
SPECTRUM
ANALYZER
CAL
COMP
TTY
SCOPE
XY PLT

A Sample And Cell

A cell was constructed from a stainless steel block of 2¼" square cross section, 3" long. A 3/4" diameter hole, bored through the length, was polished to insure good reflectivity. Two 1.5" diameter optical quality flats were held on opposite sides of the bore by gasketed rings. Stainless steel tubing connected the cell to a five degree of freedom manipulator. Elastically scattered light from these flats served as a local oscillator in the light beating process. The cell could be translated in the plane perpendicular to the optic axis; the remaining three movements were angular. Thus, the cell was easily aligned to the optic axis, which shifted slightly from day to day. It was necessary at times to purposely misalign the cell to eliminate intracavity reflections that modulated the Brillouin beating signal.[1]

Research grade xenon gas from Matheson Co. containing less than 25 PPM total impurities filled the cell to within +(.08-.61)% of the critical density of 1.11 gm/cm^3.[2] The critical temperature[3] was determined to be (16.620 $\pm$ 0.0025)^{o}C from visual observation of the appearance of the meniscus that separates the two distinct phases.

B Bath, Temperature Control, Monitor

The sample cell was immersed in a dual bath thermostat. The outer bath consisted of coils of copper tubing connected to a Forma bath and circulator (model 2095), pumping water at about 1 gal/min. The water temperature was regulated to

$\pm$ 0.02^{o}C. Bronze wool, packed among the coils, and in contact with the inner bath, improved thermal conduction. The entire coil assembly and inner bath was insulated from room environment by a wood and styrofoam box.

The inner bath was a glass battery jar filled with two gallons of ethanol that was filtered once through a 0.6μ millipore polyvic filter to eliminate large dust particles. The cell was in direct contact with the ethanol. Two optical flats of the same glass as used on the cell were held in 3-point contact, 0-ring mounts which were expoxied to the glass jar 180^{o} apart. The mounts allowed the windows to be rendered parallel to one another and perpendicular to the incident laser beam. No index matching of bath fluid to glass was needed; Snell's law was used to correct the refractive index mismatch between xenon and air.

The alcohol bath was finely regulated by a Tronac model 40 precision temperature controller. It has a sensitivity of 0.05 mK, drifts less than $\pm$ 0.2 mK/hr, and less than $\pm$ 0.3 mK/week. Its regulated 100V output was stepped down by a 5:1 transformer and put through a heater in direct contact with the ethanol. The heater was one continuous length of 31 AWG nichrome wire (total resistance $\sim$100Ω) wrapped a number of times around four insulating posts. This assembly sat on the bottom of the battery jar around the cell. Response was very rapid and heating efficiency very high with this configuration. A Fenwal glass bead thermistor was used as a sensor for the Tronac's

bridge.

Convective temperature gradients in the alcohol were eliminated using an impeller stirrer driven by a 1/100 HP 600 RPM hysteresis synchronous motor. The impeller eliminates splashing at the air-alcohol interface. The synchronous motor operates with minimal frequency variation which could otherwise impose temperature variations in the alcohol via Joule heating.

Temperature was determined to an absolute accuracy of 10 mK using two mercury thermometers to cover the range of $9^{o}C$ - $31^{o}C$ (Brooklyn Thermometer Co.). Fluctuations were monitored with a second thermistor probe of 1 KΩ (@ room temperature) resistance. Calibration of the thermistor against the mercury thermometers over the range $16^{o}C$ - $26^{o}C$ yielded a coefficient of $40\Omega/^{o}C$. Continuous monitoring of the temperature fluctuations in the ethanol was effected using a Wheatstone bridge, null detector, power supply and strip chart recorder. The bridge could detect changes in the resistance of the thermistor as small as 0.01Ω. The null detector had 40 nV sensitivity and drifted less than $0.2\mu V$/day. Only 50 mV was used in the bridge circuit, to avoid self heating[4] of the thermistor (12 mK/mW). Using this monitoring system it was determined that maximum temperature fluctuations were $\pm$.25 mK/hr and drifts about 2 mK/day.

C Laser

The source was a Spectra-Physics model 165-00 argon

ion laser mounted on a shelf suspended below a Modern Optics air suspension table. Two experimental considerations dictated its mode of operation. Since the Brillouin cross section is so low ($\sim 10^{-5} cm^{-1}$), maximum output power is desired. The second consideration is that the spatial distribution of the intensity of the output beam be known exactly, since the intrinsic beam divergence broadens the linewidth. Thus, the laser was operated at 4880Å at maximum power achieveable in TEMoo mode, which had a Gaussian radial intensity distribution.(5)

No attempt was made to achieve single longitudinal mode operation since this generally reduced the power by half. However, this was unimportant for two reasons. The longitudinal intermode beats were 143 MHz apart, out of the range of the spectrum analyzer. Secondly, the phase fluctuations of any mode, which are responsible for the linewidth of the laser in the optical spectrum, are absent in the light beating spectrum.(6)

The laser was operated half an hour before the output power was maximized through tuning of the rear reflector. Next, a check was made for TEMoo operation by expanding the output beam with a simple lens and visually examining the projected image for the well known circular intensity pattern for this mode.(7) The intra-cavity aperture was then reduced until a drop in output power was noted on a solar cell detector. Decreasing the aperture decreases the Fresnel number.(8) Higher order transverse modes are

eliminated because diffraction losses are too large for the resonator to overcome.

Lastly, the laser had built in intensity stabilization. A portion of the output beam was sampled, and a feedback loop controlled the current supplied to the plasma tube to compensate for any intensity variation. In this mode intensity fluctuations were at most $\pm .3\%$ per hour. Now small amplitude fluctuations can contribute additional terms to the photocurrent power spectrum.[9] But, these terms are of the order of the intensity fluctuation squared, which were too small to be a factor for this stability.

In the intensity stabilized mode, at 31 amps of current (less than maximum possible) the magnetic field was increased to its maximum value ($\sim$1 kG) and generally 1.2 watts of power was delivered at 4880Å for TEMoo into the sample.

D Optics

The focussing optics consisted of dielectric mirrors to route the laser beam, and a spatial filter to provide a well defined incident wavevector.

The collection optics consisted of a wide angle, large diameter lens for gathering scattered and unscattered light, optical railing for collinear mounting of components, a photo-aperture glass plate, and a simple rectangular slit over the photomultiplier tube. A Wood's horn intercepted the focussed, direct laser beam before it reached the photo-aperture. All components were on the air suspension table.

1 Focussing Optics

A Coherent Optics model 827 spatial filter was used to eliminate off-axis wavevectors that arose from reflections from mirrors and scattering in air as the laser beam was routed to the cell. It was placed as close as possible to the input window of the ethanol bath. The filter consisted of a diffraction limited 12 mm focal length, F/4 lens followed by a 10μ diameter pinhole, followed by a second diffraction limited F/4 lens of 8 mm focal length. The pinhole was at the focal point of the input lens and was slightly larger than the spot size, $6\mu(1/e^2)$. It blocked wavevectors that were at some angle to the optic axis and preferentially passed wavevectors parallel to the optic axis. The second lens recollimated the focussed beam.

The brightness (etendue) of the instrument is invariant[10]; thus, the power per area per solid angle is constant. If D_{IN}, θ_{IN} are the diameter and divergence of the input beam respectively, and F_{IN}, (F_{OUT}) are the input (output) lens local length then:[11]

$$D_{OUT} = D_{IN}\, F_{OUT}/F_{IN} = 2/3\ D_{IN}$$

$$\theta_{OUT} = \theta_{IN}\, F_{IN}\, /F_{OUT} = 3/2\ \theta_{IN}$$

Thus, the incident beam was shrunk to 2/3 its diameter with corresponding increase in intensity, but the divergence increased by 3/2. The Gaussian radial intensity distribution was preserved, and the beam incident on the sample had a very well defined unit wavevector.

The intrinsic beam divergence is difficult to measure, but for a Gaussian beam may be determined from a measurement of the beam waist radius, w, from:[12]

$$\theta_{DIV} = \lambda/(\pi w) \text{ (half angle)}$$

A separate experiment yielded a beam waist radius of $(1.23 \pm .05)$ mm (e^{-2}) at the output of the spatial filter so that $\theta_{DIV} = 0.126$ mrad.

2 Collection Optics

The sample scattered light, elastically scattered light, and direct laser beam were collected by a lens placed 14 cm from the exit window of the ethanol bath. This lens was a Zenith Optical F/6.0, aerial camera Tessar type I of 613 mm EFL. The direct laser beam defined the $\hat{Z}$ axis in this cylindrical geometry. At the focal plane of the lens was placed a photographic machined glass plate (3" x 3" x .064") that had been exposed through a mask and developed and fixed as a negative. This plate served as a precision aperture and directly determined the scattering angle. The mask consisted of five annuli concentric about a square pinhole 28μ on a side. The radii of the annuli were precisely known and all five were 39μ wide. The current from a tiny photodiode positioned behind the pinhole was fed into a Keithley 153 Nanoammeter. The photo-aperture was mounted on an X-Y stage so that the diode could locate the position of the intensity maximum of the focussed, direct laser beam. Having set the photo-aperture concentrically about, and perpendicular to, the direct beam, and since the radii of

the annuli and focal length of the lens were known, the scattering geometry was established. Appendix A gives the scattering angles used in the experiment. This arrangement allowed one to realign quickly should the laser beam move so that the scattering geometry was precisely the same from experiment to experiment.

The collection lens was chosen for its large field of view (44^{o} total), long focal length, and triplet design. Since scattering angles as large as 10^{o} were considered, the lens had to be free of off axis aberrations. The Tessar[13] is an anastigmat, with flat field, small spherical abberation, and little field curvature. The depth of focus had to be large, to allow positioning the photomultiplier tube (PMT) behind the photo-aperture. The depth of focus for a point source at infinity is:[14]

$$\text{depth of focus} \approx 2F^2\lambda$$

where F is the ratio of focal length to aperture diameter. Now the effective diameter is that of the laser beam, which was 2.4 mm. Thus, the depth of focus was about 2½".

The PMT was mounted on a micrometer translation stage whose motion was perpendicular to the $\hat{Z}$ axis so that precise positioning behind each annulus was possible. A coarse motion was allowed in the second perpendicular direction. To limit further the collection aperture, two orthogonal slits were fixed to the PMT housing, ahead of the photocathode. This means that the same portion of the large photocathode surface (14.2 cm^2) was always used, so

that the quantum efficiency had no spatial dependence. The annuli determined the slit width (39μ) and the height was determined by one of the slits on the PMT (635μ or 305μ).

3 Heterodyne Efficiency

The two factors most important in optical heterodyning are phase front alignment between signal and local oscillator fields, and the coherence solid angle.[16] It can be shown[15] that the beating term in the photocurrent spectrum will be reduced to half, if the misalignment is only $.15^{o}$ - $.2^{o}$. Now the local oscillator was provided by both the Rayleigh peak and the elastically scattered light from the cell wall. Since these originate from the same scattering volume as the Brillouin signal, the phase fronts were aligned, and their radii of curvature matched also. Both local oscillators were polarized parallel to the Brillouin signal. Thus, the remaining factors affecting the heterodyne efficiency to be considered are the quantum efficiency of the PMT, which was .135 at 4880 Å, the optical losses, the field distributions, and the coherence area requirement.

The camera collection lens was flat to at least 1/8 wave so that from eqn. 2.29, the efficiency of this component is about 0.9.

Regarding the fields, the Rayleigh local oscillator and Brillouin signal have the same distribution (spherically scattered wave). The elastically scattered beam is Gaussian. In the far field zone, the difference between the Gaussian and spherical waves will be small, and both approximately

plane. Thus, the field distributions for both local oscillators will be taken to be the same, resulting in both efficiencies near unity.

Only the coherence area requirement remains. Now (A = area),

$$\epsilon_{coh} = \frac{A_{coh}}{A_{collection}} = \frac{\Omega_{coh}}{\Omega_{col}}$$

$$\Omega_{coh} = \lambda^2 / A_{source}$$

$$\Omega_{col} = A_{detector} / f^2$$

f = focal length of lens

$$\therefore \epsilon_{coh} = \lambda^2 f^2 / (A_{source} A_{det})$$

For the small angles of the present experiment, the source is roughly circular, $A_{source} = \pi r^2 / n^2$, where r is the incident beam radius, n the refractive index of xenon. With

$f = 61.3$ cm

$\lambda_o = 4880$ Å

$r = .12$ cm

$n = 1.13$ (@ 4880 Å)

$A_{det} = 39 \times 10^{-4} \times 305 \times 10^{-4}$ cm^2

the coherence heterodyne efficiency is about 2.15. The complete heterodyne efficiency is:

$$\epsilon_{total} = \epsilon_{coh}\, \epsilon_{optical}\, \epsilon_{q.e.} = (2.15)\ (.9)\ (.135) = 0.26$$

all other efficiencies being unity.

E Electronics

The photomultiplier tube used was an RCA 7326 head-on

type, having S-20 spectral response and a quantum efficiency of 13.5% at 4880Å.[17] Its risetime leads to an intrinsic cutoff frequency of 72 MHz. However, the effective cutoff frequency is determined by the transfer function of the RC components in the socket, load and coaxial cable. The transfer function was accurately determined over the range of 1-100 MHz using the spectrum analyzer-frequency synthesizer-signal averager. Assuming a simple RC low pass filter, the cutoff frequency was 52.5 MHz, still well above the maximum Brillouin frequency examined, 25 MHz.

In spectrum analysis of light beating spectra, the photocurrent should be maximized. The current is responsible for the power spectrum; as much gain as possible should be developed at the detector stage (rather than post-amplification of signal voltage). The dynode chain resistance was chosen as small as possible to develop a large current gain per stage. Typical currents drawn from the PMT were 400μA (1 m A is maximum rating). Attempts to develop a larger current using smaller dynode resistances caused overheating of the tube, operated at ambient temperature. A high current supply (Hamner N-4035) was necessary; operating voltage was -1750 VDC. The tube had a focussing grid and the voltage to it could be varied using a potentiometer. The pot was fixed to maximize typical currents and thereafter left alone. Now with 400μA currents, and since the spectrum analyzer had 0.1μV sensitivity, no amplication was necessary. A 47Ω load resistor was used

to match the 50 Ω input resistance of the spectrum analyzer. The tube was in an RF shielded housing (Pacific Photometric) but was not cooled. Since the shot noise was about 750 times greater than the thermal noise, no significant gain in overall noise reduction would have been obtained through cooling.

An Exact (model 801) frequency synthesizer having 10 PPM frequency accuracy was used to calibrate frequencies measured with a Hewlett-Packard 8552A/8553L spectrum analyzer. This combination allowed precise frequency calibration and ease in adjusting the spectrum analyzer for each experiment. The spectrum analyzer's range was effectively .1-100 MHz. Five IF bandpass filters having nominal widths (FWHM) of 3, 10, 30, 100, and 300 kHz were used. Exact determination of the transfer functions of these filters was made, since these contribute to the instrumental linewidth. The spectrum analyzer was operated in a linear amplitude mode, so that a voltage vs. frequency spectrum was obtained. These spectra were later normalized by the transfer function of the circuitry then squared to give the power spectrum (done in a digital computer). The center frequency was set using the frequency synthesizer; sweep widths were set by the spectrum analyzer. The scan time was fixed at 2 seconds/sweep and allowed to free run but was triggered by the signal averager at the start of the averager's measurement cycle.

The signal averager was a Nicolet model 1072 Fabritek having 1K of magnetic memory and 18 bits per channel capacity. The swept output of the spectrum analyzer was DC coupled to

a 9 bit A/D converter plug-in module (SD-72/2A) of the Fabritek. The module allowed DC offset to be nulled for each experiment, and provided switch selectable RC filtering of the input. The filter time constant was chosen in accordance with the rule: (18)

$\tau_{RC} = (1/4)\frac{BW_{IF}}{SW} T$ where BW_{IF} is the bandwidth of the IF section of the spectrum analyzer, SW is the sweep width, and T the sweep time of the spectrum analyzer. The factor of 4 allows the filter to respond to abrupt changes in signal level (high frequency components). A second plug-in module (SW-71A) controlled the Fabritek sweep time, set at 2.56 seconds. Because of the difference in sweep times between the spectrum analyzer and Fabritek, 195 channels comprised a spectrum. The Fabritek provided a gated output at the start of each measurement cycle to trigger the spectrum analyzer. The number of sweeps (averaging time) was selectable on the Fabritek. Depending on the noise in the beating signal, total averaging times ranged from 11-175 minutes.

The Fabritek supported an X-Y plotter and scope, the latter providing a continuous view of the updated signal. Lastly, the Fabritek was interfaced to a PDP8/E minicomputer which could control operation of the averager and accept data for storage.

F Computer Interface

A Digital Equipment Corp. PDP8/E (8) minicomputer controlled data transfer from the Fabritek. It also served

as a timeshared link to a DEC PDP - 10. The Fabritek was used in a stand alone mode without computer control. At the end of an experiment, it was linked to the 8 for data transfer via programmed control. Generally, data were not stored in the 8 but immediately transferred to the 10. All data reduction, analysis, and ultimate storage was done on the 10 which supported a line printer, Calcomp plotter, magnetic tape, and high level (Fortran) languages. The 8 supported a scope and X-Y plotter and was accessed through a switch register, or via Decwriter (TTY).

A block diagram of the interface between the Fabritek and the PDP-8/E is shown in figs.3.2,3.3. Three bits of the 12 memory data (MD) lines were converted into positive I/O pulses (BIOP) by a DEC KA8-E Positive I/O Bus Interface. An additional six bits were converted (BMB03-08) to carry the device selection code. This interface also linked the accumulator (AC) to the Fabritek on one set of lines, and the memory buffer register of the Fabritek to the AC on another set of lines.

The Fabritek interface had a flag flip flop. A programmed I/O transfer (IOT) instruction from the 8 was used to check its status. The program waited in a loop until the device was ready. When the flag was set, an IOT asserted the SKIP bus. Program control was then transferred to a subroutine which then communicated with the device (data transfer, etc.). The Fabritek interface contained a device selector which monitored the BMB lines, and an IOT generator.

Figure 3.2: Data flow between PDP - 8 minicomputer and Nicolet 1072 Fabritek signal averager. INST REG is the instruction register of the PDP - 8. The interface is detailed in Fig. 3.3.

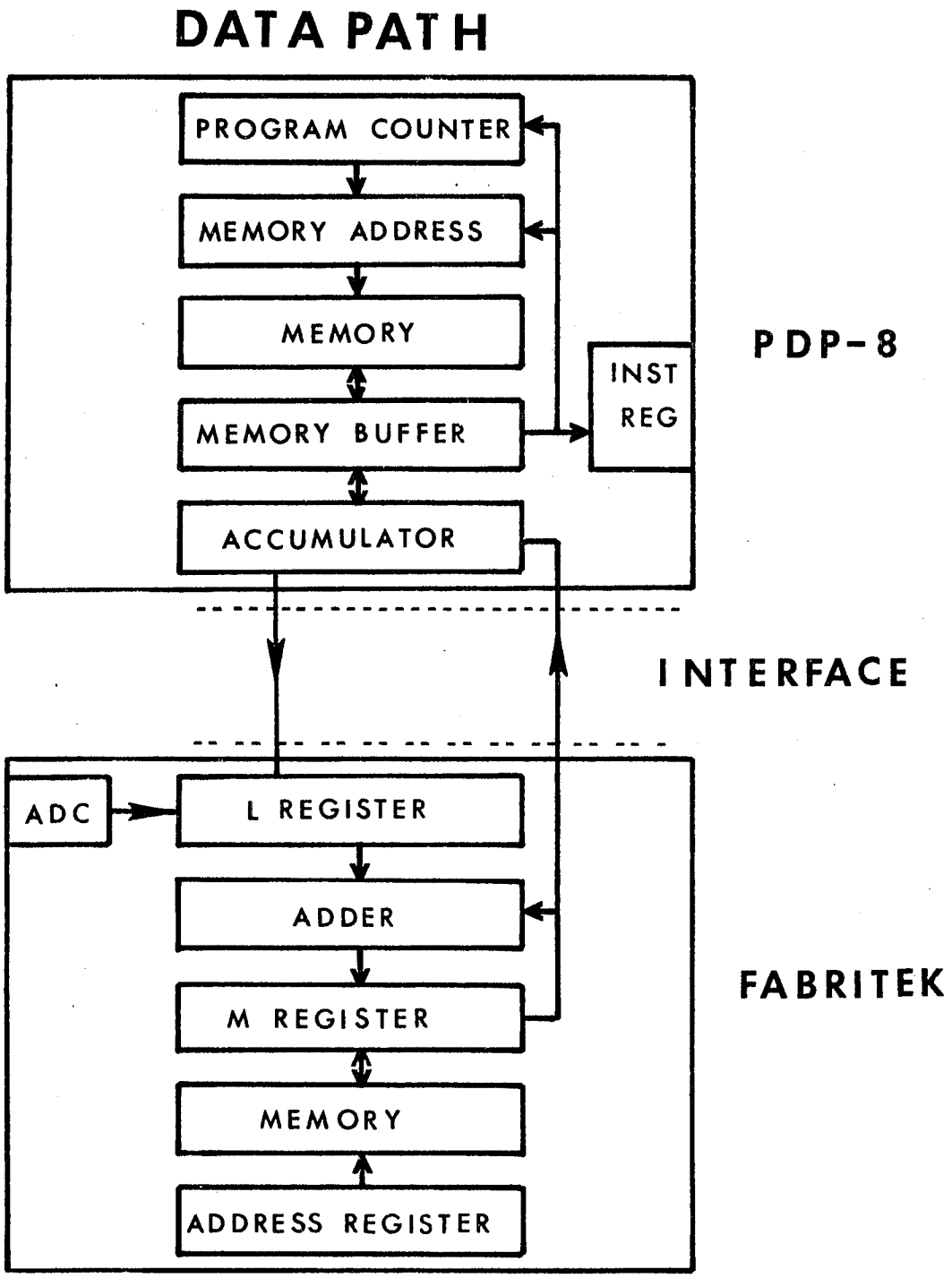
DATA PATH
PROGRAM COUNTER
MEMORY ADDRESS
MEMORY
MEMORY BUFFER
ACCUMULATOR
INST REG
PDP-8
INTERFACE
ADC
L REGISTER
ADDER
M REGISTER
MEMORY
ADDRESS REGISTER
FABRITEK

Figure 3.3: DEC KA8 - E positive input - output bus interface used to link Fabritek to PDP - 8.

POSITIVE I-O BUS INTERFACE

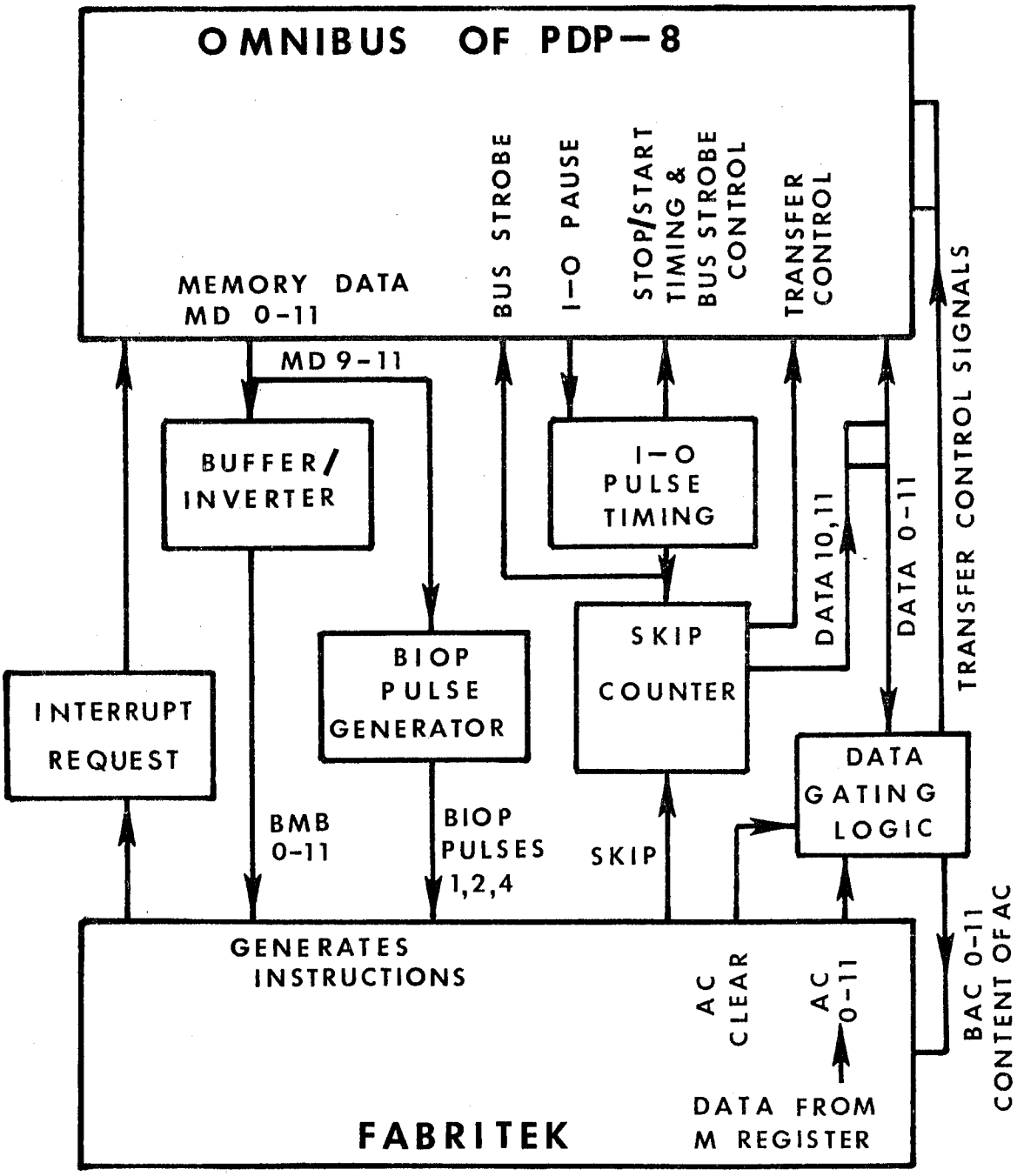

When an IOT instruction was given, BMB03-08 carried the operation code which was decoded, sent to the IOT generator and used with the BIOP pulses to carry out the operations indicated by the instructions. The BIOP pulses were applied to the IOT generator where they were regenerated as IOT pulses. Specific pulses performed specific operations such as clearing the AC, reading, loading, and clearing buffers, and sampling, skipping, and setting flags.

In this programmed I/O transfer mode of operation, all 1024 channels of the Fabritek could be transferred to the 8 in a few hundred microseconds.

G SNR

The maximum value of the signal to noise ratio, SNR_{max}, may be estimated from eqn. 2.41:

$$SNR_{MAX} = \left(\frac{\delta \tau M}{\pi}\right)^{1/2} \frac{2\epsilon}{e}\left(\frac{1}{\mathcal{F}}\right) \frac{\langle i_s \rangle}{T_B}$$

The SNR will be calculated using real data obtained at a scattering angle of 0.7^{o} (air), at the extremes of temperature, $\Delta T = 10^{o}K$ and $0.05^{o}K$.

The specific heat ratio is obtained from Appendix C. The mean photocurrent can be estimated as follows,

$$\langle i_s \rangle = e\left(\frac{1}{V}\frac{d\sigma}{d\Omega}\right) V \Omega_{coh}\left(\frac{P_L}{\pi r^2}\right)$$

where $\frac{1}{V}\frac{d\sigma}{d\Omega} = R$ = Rayleigh Ratio = 1×10^{-6} cm^{-1}

e = 1.6×10^{-19} Coulomb

V = scattering volume = $r^2 l$

P_1 = incident laser power = 2.5×10^{18} photons/s @ 4880Å

r = incident beam radius = .12 cm

l = length of scattering volume = 5 cm

$$\Omega_{coh} = \lambda_o^2/(n^2 A_{soure}) = \lambda_o^2/(n^2 \pi r^2)$$

$$\langle i_s \rangle = \frac{e R l \lambda_o^2 P_L}{n^2 \pi r^2} = 8.25 \times 10^{-14} \text{ Amp}$$

The remaining parameters needed are:

$\Delta T = 10^{\circ}K$	$\Delta T = 0.05^{\circ}K$
$1/\gamma = .907$	$1/\gamma = 5 \times 10^{-4}$
$\Gamma_B = 1.1 \times 10^4$ Hz	$\Gamma_B = 9 \times 10^4$ Hz
$\delta = 3 \times 10^3$ Hz	$\delta = 10^5$ Hz
$\tau = 10^{-2}$S	$\tau = 4 \times 10^{-2}$S
M = 512	M = 1024

and ϵ_{total} was found to be 0.26 in this chapter.

If the single sweep (M=1) SNR is calculated, then:

$SNR_{max} = 68$	$\Delta T = 10^{\circ}K$
$SNR_{max} = .05$	$\Delta T = 0.05^{\circ}K$

It is seen that about 1.8×10^6 sweeps at $.05^{\circ}K$ are needed to achieve the same SNR as a single sweep at $10^{\circ}K$, emphasizing the difficulty of measurements as T_c is approached.

References for Chapter III

1. B. Chu, Laser Light Scattering, p.166 (Academic Press, New York, 1974).

2. H.W.Habgood and W.G.Schneider, Can. J.Chem. 32,98 (1954).

3. The accepted critical temperature of Xenon is 16.59°C (ref 2.); in critical theory, it is ΔT that is important in the scaling laws, not the absolute value of T. For the present measurements, ΔT is known to $\pm$ .0025°C.

4. T.K.Lim, Ph.D. Thesis, Johns Hopkins Univ., 1973.

5. O.Svelto, Principles of Lasers, p.109 (Plenum, New York, 1976).

6. H.Z.Cummins and H.L.Swinney, in Progress in Optics, Vol. VIII (North Holland, Amsterdam,1970), p.145.

7. Spectra Physics Model 165 Laser Operating Manual, Mountain View, CA.

8. The Fresnel number is $a^2/(d\lambda)$ where a is the radial dimension of the cavity, d the cavity length; ref. 5, p.98,111.

9. Ref. 6,p.170.

10. Ref. 5, p.269.

11. H.Weichel and L.S.Pedrotti, Electro-Optic System Design July, 22(1976).

12. Ref. 5, p.264.

13. L.P.Clerc, Photography Theory and Practice, p.130 (Focal Press, New York,1970).

14. L.Levi, Applied Optics, p.468 (Wiley,New York,1968).

15. M.Ross, Laser Receivers, p.118 (Wiley,New York,1966).

16. Ref. 6,p.166.

17. RCA Photomultiplier Tube Manual (RCA,Lancaster,PA.,1970).

18. E.Magrab and D.Blomquist, Measurement of Time Varying Phenomena, p.79 (Wiley,New York,1971).

CHAPTER IV

DATA REDUCTION & ANALYSIS/RESULTS

The analytical methods used to separate instrumental effects from the observed spectra are detailed in this chapter. First the overall problem is defined and mathematically specified as a convolution operation.

Instrumental effects are divided into two categories, electronic and optical. Electronic effects influence spectral lineshapes due to the frequency response of the overall processing instrumentation, and due to the IF filters of the spectrum analyzer. The overall frequency response is measured independently of the scattering experiments, standardized, and represented mathematically as a series of interpolation polynomials. The IF filters directly broaden any spectral feature, thus their lineshape must be known exactly. It is shown that a Voigt function represents the filter shapes very well. The general curve fitting procedure is outlined, a specific optimization algorithm detailed, then applied to the determination of the Voigt parameters.

The optical effects are diffraction limited broadening due to the intrinsic beam divergence, and aperture broadening. These are represented mathematically by a Gaussian and a rectangular function, respectively. A separate measurement is described, by which a parameter needed to characterize the diffraction broadening was determined.

Next, the function used to describe the complete observed spectrum is built up from its five component parts. It is

the convolution of a Voigt and a rectangular function, with a multiplicative constant and an additive constant. A very general nonlinear optimization algorithm is described, then used to fit the expected functional form to the observed spectra, from which the two quantities of interest, the sound velocity and attenuation, are extracted.

Results of the deconvolution process are displayed step by step in a series of graphs for a single spectrum, and a plot of three spectra at the same scattering angle for three temperatures summarizes the whole experiment. The Brillouin sound velocity and attenuation data are given in Appendix B.

A. The Total Spectrum-General

The predicted Brillouin power spectrum was shown to be Lorentzian in chapter II. This lineshape sits on a background determined by the average shot noise. However, the spectrum is modified by the measurement process which mathematically consists of the convolution of the instrumental response with the Brillouin Lorentzian shape:

$$I_{OBS}(\nu) = \left[I_B(\nu) * I_{INST}(\nu)\right] + \text{BACKGROUND}$$

$I_{OBS}(\nu)$ = observed power spectrum

$I_B(\nu)$ = Brillouin lineshape (Lorentzian)

$I_{INST}(\nu)$ = instrumental response

Background = shot noise

$*$ = convolution operation

The instrumental response is itself the convolution of the optical, $I_{OPT}(\nu)$ and electronic $I_{ELEC}(\nu)$ instrumental

responses so that:

$$I_{OBS}(\nu) = I_B(\nu) * [I_{OPT}(\nu) * I_{ELEC}(\nu)] + B \qquad 4.1$$

Now the optical instrumental response consists of two effects: diffraction broadening and aperture broadening. Diffraction broadening arises from the finite divergence of the laser beam. Though the divergence is typically only of the order of a milliradian, it introduces uncertainty in the value of the momentum transfer vector which in turn implicitly influences the power spectrum. At the smallest scattering angle of this experiment, diffraction broadening is as much as 88% of the total observed half width. Aperture broadening, due to the finite width of the collection aperture, also influences the determination of the momentum transfer vector since it spatially averages the collected scattered light over a small but finite range of scattering angle. The equation, $\omega = |\vec{q}|\,|\vec{v}|$, provides the scaling relation between the spatial uncertainty in $\vec{q}$ and frequency uncertainty in the power spectrum for both diffraction and aperture broadening.

The electronic response influences the overall spectrum shape since the transfer function of the PMT and following electronics will modify the shape of any spectral line. Also, the IF filters of the spectrum analyzer directly broaden the Brillouin Lorentzian function.

Note that the RC filter of the signal averager acts as an integrator which smoothes the noisy spectrum by not passing rapidly varying high frequencies. By suitable choice of the time constant (T = RC) in accordance with the sampling

theorem, the broadening of the observed lineshape due to the transfer function of this filter can be made negligible.

It should be noted that, in light beating spectroscopy, there is no simple means of determining instrumental response as there is using an interferometer or a grating spectrometer. In these optical filter methods, a source whose linewidth is known to be much less than the linewidth of the sample to be studied is observed, and the resulting lineshape function is taken to be the instrumental response. The linewidth is taken to be the limit of resolution of the overall instrumentation. In light beating, there is in principle no limit to the resolution achievable, so that each experiment must be analyzed for the specific instrumental effects on the particular scattering sample.

B. Electronic Instrumental Response

1. Measurement of Transfer Function of Circuitry

The constant shot noise level in each spectrum is modified by the transfer function of the electronics preceding the spectrum analyzer. This circuitry was simply the PMT itself, the resistance and capacitance of the PMT load circuit, and the resistance, capacitance of the BNC cable. No preamp or amp was used; the signal was delivered directly into the spectrum analyzer. Now the intrinsic risetime of the RCA 7326 is 2.2 ns, which implies a minimum cutoff frequency (assuming simple filtering) of :

$$f_{cutoff} = 1/(2\pi T) = 72 \text{ MHz}.$$

The actual frequency response was determined using the spectrum analyzer - signal averager and a white light source.

Cummins and Swinney[1] point out that the signal spectrum of such a source is entirely negligible compared to the shot noise it generates so that the white light serves as a shot noise generator for the PMT. The intensity of the source was adjusted to produce the same average photocurrent as that produced by the Brillouin signal (to assure the electronics operated in the same regime), and the frequency response was accurately calibrated. Assuming the transfer function is that of an RC filter,[2]

$$|H(\omega)|^2 = 1/\ (1+(\omega T)^2) \qquad T=RC$$

then when $\omega = 1/T$, $|H(\omega)|$ has fallen to $1/\sqrt{2}$ of its maximum value. The cutoff frequency over a measurement range of 0-100 MHz was determined to be 52.5 MHz at $1/\sqrt{2}$ of $|H(\omega)|_{max}$ using the EXACT frequency synthesizer and a 10 MHz frequency comb generator for precise calibration.

2 Reduction of Background To A Constant - Quadratic Interpolation

The background is present in every spectrum and cannot be taken to be a simple additive constant. Bevington[3] suggests a quadratic or higher order polynomial should be used to account for the background, and that the lineshape function and background should be fitted simultaneously over the entire region of the spectrum. However, the total number of free parameters to be determined would then be large, seven or eight. To reduce the number of parameters, thereby saving much computing time in analyzing each spectrum, the electronic response was measured over the range of interest using the

same procedure as in chapter III, then fitted piecewise to a series of quadratic collocation polynomials. The response at any given frequency could be computed from these polynomials, then divided into the observed spectrum to reduce this part of the electronic transfer function to a single additive constant.

Since the transfer function was smoothly varying, a rather coarse mesh of equally spaced 0.5 MHz points over the range 0.5 - 24.0 MHz was used. Numbers of precise determinations of the transfer function were averaged together so that the response at any given 0.5 MHz point was in error by no more than 0.2%. The results were arbitrarily normalized to a response of unity at 6.000 MHz. Every three successive points were then fitted to a quadratic to obtain the interpolation polynomial. Now the interpolating polynomial is unique no matter how determined.[4] The most direct method for finding it is that of undetermined coefficients.[5] For points (x_i, y_i) the condition that the collocation polynomial $P_n(x_i)$ pass exactly through each point is:

$$P_n(x_i) = y_i = \sum_{j=0}^{n} a_j x^j$$

Thus, a quadratic having three undetermined coefficients requires three equations to uniquely determine these coefficients. The determinant of the unknown coefficients, a_j, is the Vandermonde determinant[6] whose matrix satisfies the equation:

$$\begin{pmatrix} y_1 \\ y_2 \\ y_3 \end{pmatrix} = \begin{pmatrix} 1 & x_1 & x_1^2 \\ 1 & x_2 & x_2^2 \\ 1 & x_3 & x_3^2 \end{pmatrix} \begin{pmatrix} a_1 \\ a_2 \\ a_3 \end{pmatrix}$$

This matrix equation was solved for the a_j using the matrix

inversion Fortran subroutine of the IBM Scientific Subroutine Package.[7] A quadratic polynomial was now assigned to every 0.5 MHz reference point, so that the response at an intermediate frequency was computed from the collocation polynomial whose reference frequency was closest to the arbitrary frequency. The range of each reference frequency, ν_R, was taken to be $\left[\nu_R - 0.249999 \leq \nu \leq \nu_R + 0.250000\right]$ MHz. There were 46 such polynomials to cover the range of 0.5 - 24.0 MHz.

Figure 4.1 shows the averaged transfer function over the range 0.5 - 24.0 MHz normalized to unity at 6.00 MHz.

3 Partial Reduction of Spectrum

For every spectrum, three calibration frequencies were experimentally determined as follows. After the completion of a spectrum, the settings of the spectrum analyzer and signal averager were left alone, and a precise calibration signal from the frequency synthesizer was fed into the spectrum analyzer and averaged in a separate portion of the FABRITEK'S memory. After a few sweeps, the location of the maximum of this frequency (one is reproducing the IF bandpass filter shape of the spectrum analyzer under given conditions) was determined using the FABRITEK'S address selection mode which gave the address and decimal content of any channel. The three frequencies were chosen to be left, right, and near the center of the Brillouin signal. With the calibration frequencies, the entire spectrum could be assessed a frequency value (MHz) per point. This was done using linear interpolation with two scales derived from the three reference frequencies (the spectrum analyzer is quite linear; the

Figure 4.1: Transfer function of PMT electronics. The range 0.5 - 24.0 MHz has been arbitrarily normalized to a response of unity at 6 MHz.

ELECTRONIC TRANSFER FUNCTION

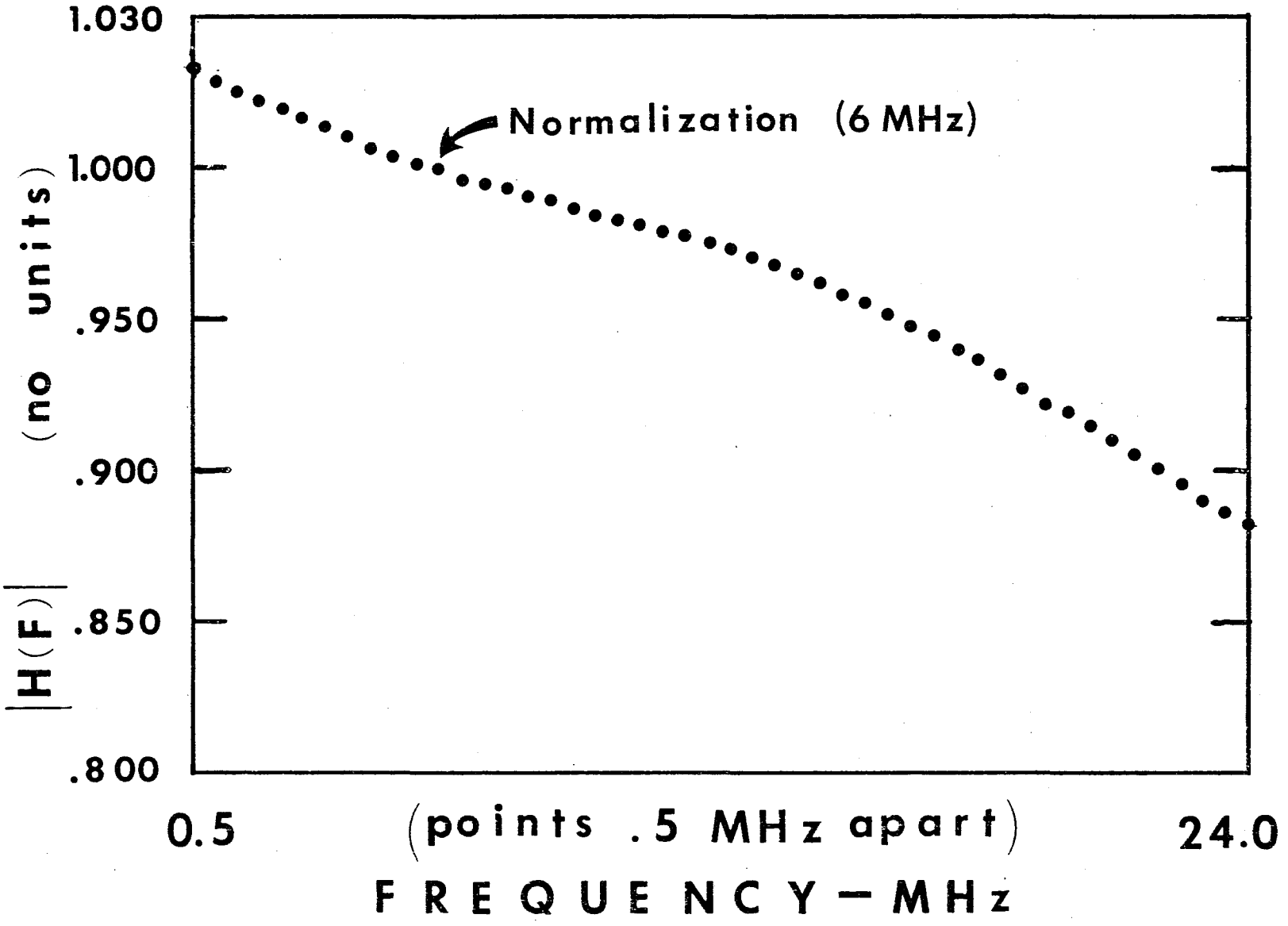

frequency response is rated at $\pm$ 0.5 dB over the range 1 kHz - 100 MHz, with fine grain flatness better than $\pm$ 0.1 dB per MHz). The calibration point nearest a given point was selected for the interpolation. Since the spectral range of any spectrum was generally only six halfwidths, linear interpolation over this small a range was very accurate ($\sim$ 0.1% of any frequency value).

For every frequency, the nearest 0.5 MHz reference frequency for the electronic response was determined by comparison with a table. The response at the particular frequency was computed from the coefficients of the collocation polynomial, then divided into the observed response and the result squared. The result was the power spectrum normalized to the PMT electronic transfer function response, with the background effectively reduced to the additive constant associated with the shot noise level.

Figures 4.2, 4.3 show two spectra. Figure 4.2 is a "raw" spectrum showing the voltage spectrum versus channel number as it comes out of the signal averager. Figure 4.3 shows the same spectrum after calibration of the frequency axis, normalization to the electronic response, and squaring, to give the power spectrum. Note how the severe background slope is levelled off by the normalization.

4 IF Filters

a Transfer Function Measurement

Since the IF bandpass filters of the spectrum analyzer directly broaden the

observed lineshape function, the transfer functions of these

Figure 4.2: Raw data - voltage spectrum. Typical spectrum as it appears in signal averager after 34 minutes of averaging. $\Delta T = .05^{o}K, \theta = 0.7^{o}$.

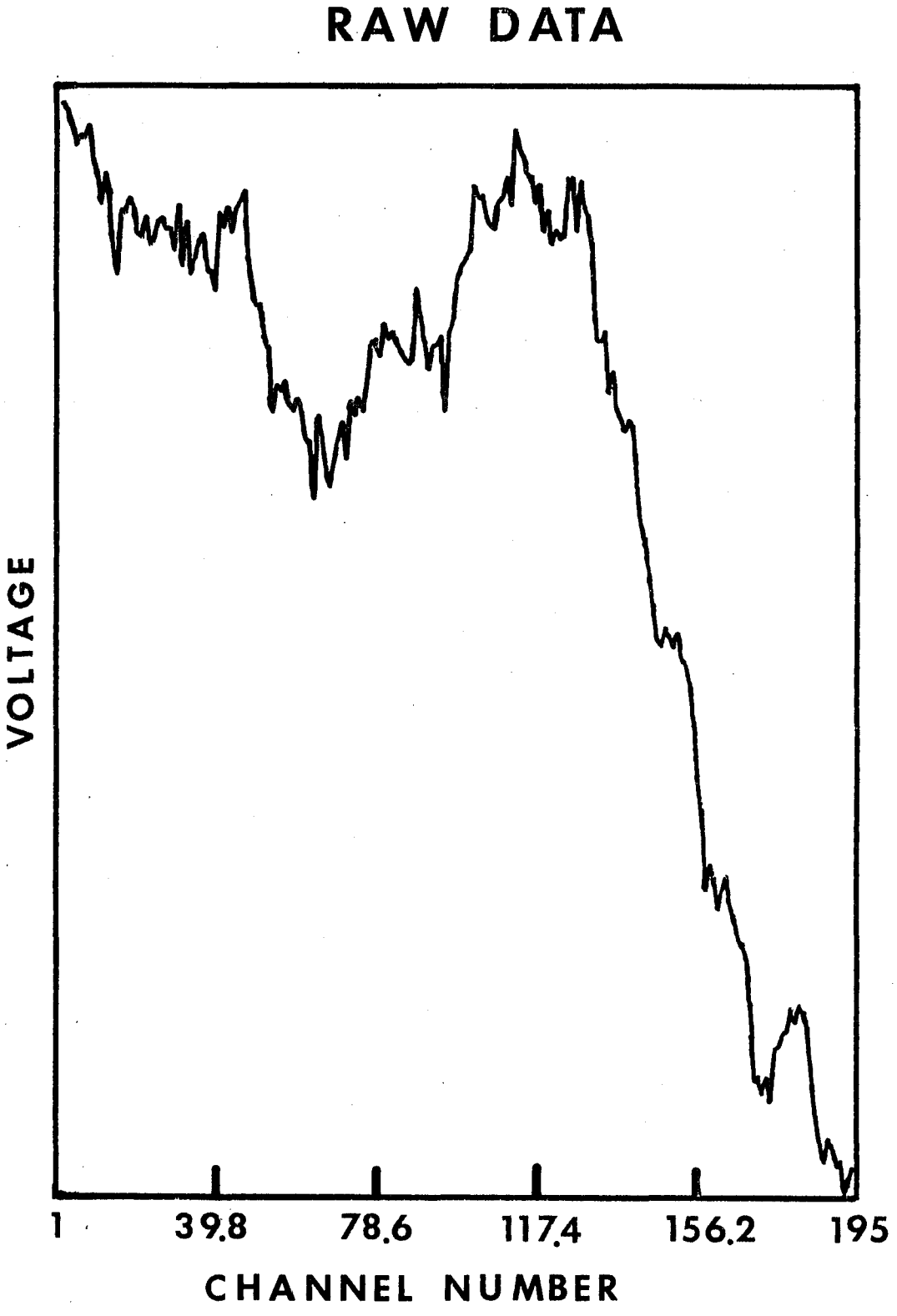
RAW DATA
VOLTAGE
1
39.8
78.6
117.4
156.2
195
CHANNEL NUMBER

Figure 4.3: Normalized power spectrum. The data of fig. 4.2 after division by the transfer function of fig. 4.1, squaring to obtain power, and scaling to obtain frequency. Note how the severe background slope has been leveled off to effectively a simple constant.

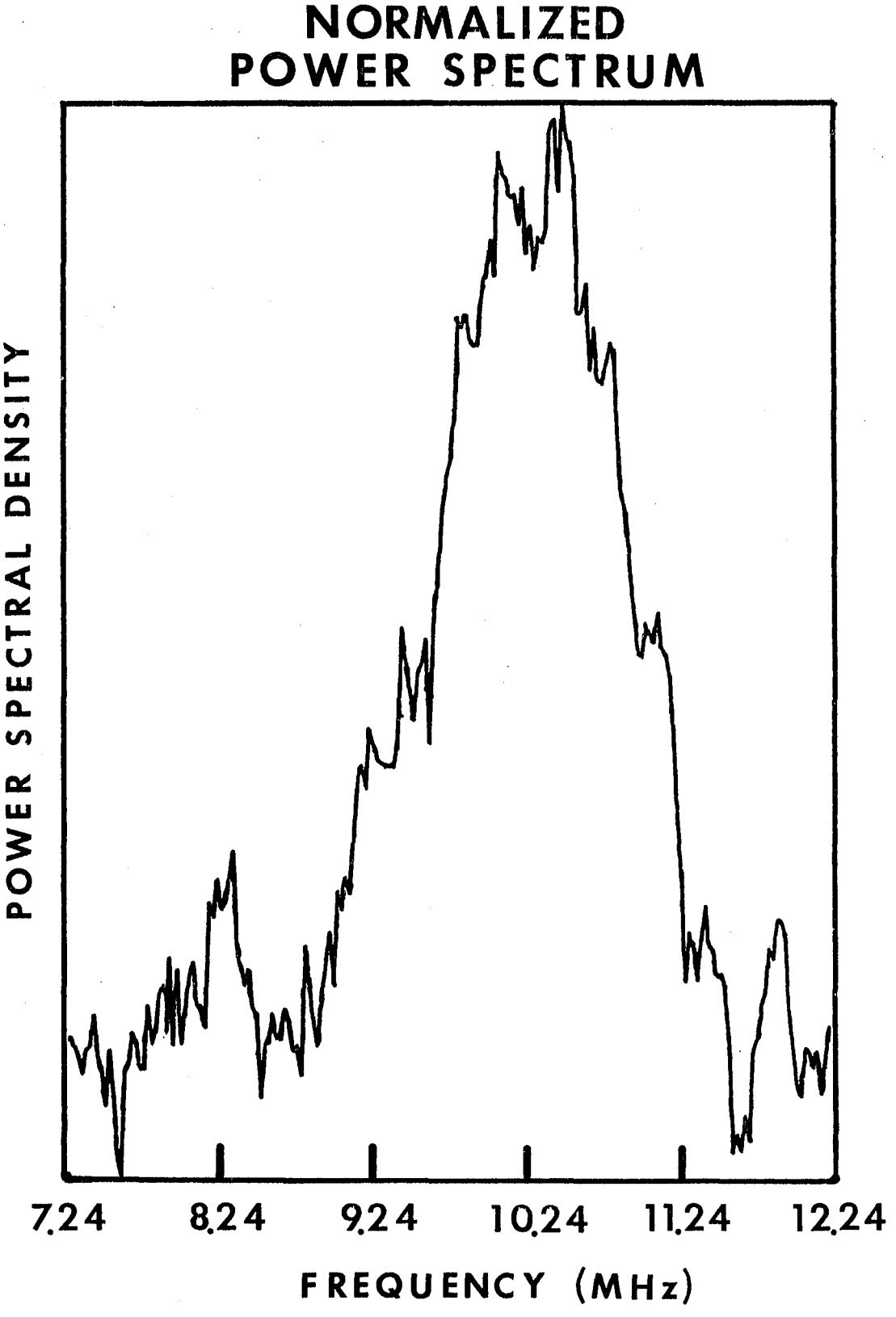
NORMALIZED
POWER SPECTRUM
POWER SPECTRAL DENSITY
7.24
8.24
9.24
10.24
11.24
12.24
FREQUENCY (MHz)

filters had to be determined precisely.

A linear, stationary filter transforms an input signal, $S_{IN}(t)$, via its impulse response function $h(\tau)$:[8]

$$S_{OUT}(t) = \int_{-\infty}^{\infty} h(\tau) S_{IN}(t - \tau)\, d\tau$$

The transfer function is:

$$H(\omega) = \int_{-\infty}^{\infty} h(\tau) \exp(i\omega\tau)\, d\tau$$

Thus, if $S_{IN} = e^{-i\omega t}$, then $S_{OUT} = H(\omega)\, e^{-i\omega t}$ which shows that the filter's response is specified by its sinusoidal steady state behavior.

For each of five filters used, the transfer function was determined by inputting a pure sinewave to the spectrum analyzer, using again the EXACT synthesizer. The transfer functions were determined under the same operating conditions (sweep speed, etc.) as used to determine spectra, then averaged and stored in the FABRITEK. The background level was electronically nulled so only the filter lineshape itself needed to be fitted. It was found, contrary to the manufacturer's specifications, that the lineshapes were not strictly Gaussian but had a small Lorentzian component, which gave overall a Voigt transfer function.

The general curve fitting procedure will next be described, then applied to these bandpass filter lineshapes.

b Curve Fitting-General

The goodness of fit of a functional form $y(x_i)$ to measured data points (x_i, y_i) is obtained from the χ^2

characteristic[9]:

$$\chi^2 \equiv \sum_{i=1}^{N} W_i \left(Y_i - Y(X_i)\right)^2 \qquad 4.2$$

where W_i = weighting factor per point, i

$= 1/\sigma_i^2$ = standard deviation per point

Y_i = measured dependent variable

X_i = measured independent variable

$Y(X_i)$ = fitting function

In general, $Y(X_i)$ will depend on a number of parameters, P_j. According to the least squares method, the optimum values of parameters P_j used to characterize the function $Y(X_i)$ are obtained by minimizing χ^2 with respect to each parameter simultaneously:

$$\frac{\partial \chi^2}{\partial P_j} = \frac{\partial}{\partial P_j} \sum_{i=1}^{N} W_i \left(Y_i - Y(X_i)\right)^2 = 0$$

$$j = 1, \ldots m$$

It is seen that the general procedure has three main features: proper choice of fitting function, choice of weighting factor, and an algorithm to effect the minimization. There are two large classes into which algorithms fall, depending on whether $Y(X_i)$ is linear or nonlinear in its dependence on the parameters. In all curve fitting for this experiment, the dependence is nonlinear.

c Fitting Function

For the IF filters, both Gaussian and Lorentzian lineshapes were assumed for the fitting function, and attempts at fitting these forms (by a method to be described) to the data showed them both to be inadequate. Next, a Voigt lineshape was assumed. This function is defined as the convolution of a Gaussian and Lorentzian:[10]

$$V(\beta(L),\beta(G),\nu) \equiv \int_{-\infty}^{\infty} \frac{\beta(L)/\pi}{\beta(L)^2+(\nu-\nu')^2} \frac{e^{-(\nu'/\beta(G))^2}}{\sqrt{\pi}\ \beta(G)}\, d\nu' \qquad 4.3a$$

where $\dfrac{e^{-(\nu'/\beta(G))^2}}{\sqrt{\pi}\ (\beta(G))}$ is a Gaussian lineshape 4.3b

$\dfrac{\beta(L)/\pi}{\beta(L)^2+(\nu-\nu')}$ is a Lorentzian lineshape 4.3c

$\beta(L)$ = HWHM of Lorentzian

$\beta(G)$ = ($1/e$) width of Gaussian

The constant factors normalize V to unit area. This has no closed form analytic expression; it must be approximated or numerically generated. A good approximation to this function was found by Kielkopf:[10]

$$U(\eta,x) = V/I = (1-\eta)G(x) + \eta L(x) + \eta(1-\eta)E(x)(G(x)-L(x))$$

$x = (\nu-\nu_0)/\beta$

$G(x) = \exp(-(\ln 2)x^2)$

$L(x) = 1/(1+x^2)$ 4.4

η = pure number $\quad 0 \le \eta \le 1$

$E(x) = \dfrac{.8029 - .4207x^2}{1+.2030x^2+.07335x^4}$

I = constant proportional to intensity

β = Voigt HWHM

ν_0 = center frequency

$U(\eta, X)$ as defined is a normalized (to unity) dimensionless lineshape function. It approximates the Voigt function by taking a linear combination of Gaussian and Lorentzian component parts, with η the weighting factor of the Lorentzian component. The function E(X) is a rational fraction correction. The accuracy claimed by using this approximant to the Voigt is .0001 of the peak value of the function.

The fitting function was then taken to be $Y = IU(\eta, X)$, with $U(\eta, X)$ as given above. The number of free parameters that describes this function is four: I, η, β and γ_0 which are the peak intensity, weighting fraction, Voigt HWHM, and center frequency, respectively.

Once these four parameters were determined, the two quantities of interest, β (L) and β (G), could be derived from relations given by Kielkopf as follows. From η, a quantity μ was determined from:

$$\mu(\eta) = \frac{1 + .2820\eta - 1.602\eta^2 + .6413\eta^3 - .1873\eta^4}{.8211 + 1.017\eta - 1.315\eta^2 + .5266\eta^3 - .1538\eta^4} \frac{\eta}{1-\eta} \quad 4.5$$

Next, μ and β were used to determine β (L) and β(G) from:

$$\beta(L) = \frac{2\beta}{1 + .099\ln 2 + \left((1 - .099\ln 2)^2 + 4\ln 2/\mu^2\right)^{1/2}} \quad 4.6$$

and $\beta(G) = \beta(L)/\mu$ 4.7.

Finally, β (G) was converted to the HWHM from the relation[11]:

$$\Gamma(HWHM) = \beta(G)\ \frac{2.354}{2\sqrt{2}} = \beta(G)\,(.8325) \quad 4.8$$

d Weighting Factor

The data for the transfer functions were accumulated

with almost no electronic noise. However, there is digitizing noise associated with the ADC of the FABRITEK. All data were accumulated at 9 bits resolution. The FABRITEK allows positive and negative inputs, while the data were all positive. Thus, the resolution per sweep was 1/256, with the amplitude adjusted to be full scale.

The error should be the same for any single point. However, the averager has the effect of increasing the vertical resolution above that of the ADC. Since the noise after M sweeps is:

noise (M sweeps) = noise (1 sweep) $\sqrt{m}$ then $\sigma(m)$ = $\sqrt{m}\ \sigma(1) = \sqrt{m}\ n_{MAX}(1/256)$ where n_{MAX} is the maximum counts in any channel. Further, the desired quantity was the power, not the voltage, so that the voltage count data, n, should be transformed as[12]:

$$f(n) = n^2$$

which induces the transformation on σ:

$$\sigma_{Power} = \sigma_{voltage} \frac{\partial f}{\partial n} = \sigma_{Voltage}\ 2n$$

Therefore,

$$W_{Power} = \frac{1}{\sigma^2_{Power}} = \frac{1}{\sigma^2_{Voltage}} \frac{1}{(2n)^2}$$

The relative weighting factors are expected to be equal, so that W_{Power} should be a constant for all channels. Thus,

$$W_{Pi} = \frac{1}{\sigma^2_{Voltage}\ (2n_{MAX})^2}$$

$$i = 1, \ldots N$$

$$W_{p_i} = \frac{1}{\sqrt{M}\,(3.90625 \times 10^{-3}\, n_{MAX})^2} \quad \frac{1}{(2\, n_{MAX})^2}$$

$$= \frac{1}{4\, M\, (3.90625 \times 10^{-3})^2\, n_{MAX}^2}$$

where M is the number of sweeps.

e Optimization Algorithm

For a function of a single variable, Powell[13] suggested fitting a quadratic polynomial to the function by interpolation, then using the polynomial to predict the minimum. The advantage is that a possibly complex function is replaced by a very simple one, the minimum of which is known analytically. Implicit is the assumption that the approximated function is smooth and unimodal (single maximum/minimum) over the range of the parameter.

Powell's original algorithm has two bad features: the predicted minimum could be a maximum, and the iterative stepsize to the minimum could be too long, so that convergence is slow. A modification of the algorithm suggested by Box, et al[14] was found to be more reliable and will be presented here. An implementation is found in Bevington.[15]

To use this univariate method to optimize χ^2, a multivariate function, it is assumed that the variation of χ^2 with a single parameter is independent of the optimization of the remaining parameters, so that the optimum values are found by minimizing χ^2 with respect to each parameter separately.

The algorithm proceeds as follows: The parameters are designated P^i (i = 1,2,3,4) while different values of a particular parameter are labelled P^i_j (j = 1,2,3).

1. initial estimates for P^i, and the increment size ΔP^i are made; χ^2_{OLD} is computed from the initial estimates of all parameters P^i_1

2. Compute $P^i_2 = P^i_1 + \Delta P^i_1$; compute $\chi^2(P^i_2)$

3. if $\chi^2(P^i_2) = \chi^2(P^i_1)$, repeat step 2
   if $\chi^2(P^i_2) < \chi^2(P^i_1)$, continue to step 4
   if $\chi^2(P^i_2) > \chi^2(P^i_1)$, take $\chi^2(P^i_1) = \chi^2(P^i_2)$

   $\chi^2(P^i_2) = \chi^2(P^i_1)$

   reverse direction of search, $\Delta P^i = -\Delta P^i$

   compute $\chi^2(P^i_1 + \Delta P^i)$ then go to step 2

4. compute $P^i_3 = P^i_2 + \Delta P^i = P^i_1 + 2\Delta P^i$ compute $\chi^2(P^i_3)$

5. if $\chi^2(P^i_3) < \chi^2(P)$ take $\chi^2(P^i_1) = \chi^2(P^i_2)$
   $\chi^2(P^i_2) = \chi^2(P^i_3)$

   go to step 4

   if $\chi^2(P^i_3) \geq \chi^2(P^i_2)$ continue to step 6

6. using the last three points obtained, $(\chi^2(P^i_j), P^i_j)$ $j = 1,2,3$ where $\chi^2_2 < \chi^2_1, \chi^2_3$ $\Delta P^i = |P^i_1 - P^i_2| = |P^i_2 - P^i_3|$
   the predicted minimum is:

$$P^i_{MIN} = P^i_3 - \Delta P^i \left(\frac{\chi^2(P^i_3) - \chi^2(P^i_2)}{\chi^2(P^i_3) - 2\chi^2(P^i_2) - \chi^2(P^i_1)} + \frac{1}{2} \right)$$

7. the error associated with determining the parameters P^i is

$$\sigma_P^2 = \frac{2(\Delta P^i)^2}{\chi^2(P_1^i) - 2\chi^2(P_2^i) + \chi^2(P_3^i)}$$

8. steps 2 - 7 are repeated for each parameter P^i in turn

9. from the estimates of P^i_{MIN} for all parameters, compute

$\chi^2_{NEW} = \chi^2(P^i_{MIN})$ $i = 1, \ldots N$

if $\left| \frac{\chi^2_{New} - \chi^2_{Old}}{\chi^2_{Old}} \right| \leq \epsilon$ convergence

if " $> \epsilon$ use P^i_{MIN} as new initial estimates, decrease ΔP^i, go to step 1

f Discussion of Algorithm

The disadvantages of this method are that if the parameters are not all independent, convergence may be slow or not at all. The convergence criterion used in step 9 seeks a small relative percentage error in successive changes of χ^2. As the requirement for accuracy increases, the computational cost of repeated polynomial calculation becomes larger, and for three or more parameters, this method is not recommended. If the initial estimates for the parameters are far from the true minima, convergence to reasonable accuracy ($\simeq$ 5%) in the parameters will be very difficult to achieve. Noisy data can only increase computation time, and in many cases, the parameters assume unreasonable values. Note that the method implicitly assumes unconstrained conditions, so that all parameters range from $-\infty$ to $+\infty$. If the parameters are

definitely known to lie within certain bounds, this information should be used to keep the parameters from wandering far from their respective minima.(16)

The error calculated in step 7 follows directly from the expression for the error matrix given by Bevington.(17)

g. Results Of Fitting IF Filters To Voigt Function

The preceding algorithm was applied to the transfer function data to determine the optimum values of the parameters in the Voigt function approximant, 4.4. It was expected that the method would work well in spite of the number of parameters involved since the data were smooth and noise free and excellent guesses for I and ν_o were known. Also, η was a simple constant that varied from zero to one so an initial value of 0.5 was readily assumed.

All four parameters were allowed to vary since this gave a better fit (smaller χ^2) than fixing I and ν_o and allowing η and β to vary. Since errors could be obtained for β and η via step 7 of the algorithm, and $\beta(L)$ and $\beta(G)$ depended on them through equations 4.6, 4.7, errors in $\beta(L)$ and $\beta(G)$ could be determined from a standard propagation of error analysis. However, since a number of transfer functions for each filter was obtained (at different frequencies), the results for $\beta(L)$ and $\beta(G)$ for each determination were simply averaged and an error assigned according to standard definitions:

$$\bar{X} = \sum_{i=1}^{N} X_i/N \qquad \text{mean}$$

$$\sigma^2 = (1/(N-1)) \sum_{i=1}^{N} (X_i - \bar{X})^2 \qquad \text{deviation} \qquad 4.9$$

Table 4.1 lists the results of the optimization algorithm which gave the best fit Voigt function with parameters $\beta(L)$ and $\beta(G)$ to the IF filter transfer functions of the Hewlett-Packard 8553L IF section of the spectrum analyzer.

Figure 4.4 shows the nominal 100 kHz IF filter transfer function. The points were experimentally determined according to the procedure in section B.4a. The curve shows that best fit Voigt function. Note that the actual FWHM was 98 kHz, which is greater than either the Gaussian (92 kHz) or Lorentzian (11 kHz) component, but less than the sum of these components. This is a useful general rule for a function which is the result of a convolution of two other functions. There is no simple or analytic means of determining the total linewidth from known values of the component widths. The convolution must be done explicitly and the linewidth of the resultant determined graphically or by numerical methods. Stated for the Voigt function, the rule for the linewidths is: (18)

$$\left.\begin{matrix}\Gamma(\text{GAUSSIAN}) \\ \text{or} \\ \Gamma(\text{LORENTZIAN})\end{matrix}\right\} < \Gamma(\text{VOIGT}) < \Gamma(\text{GAUSSIAN}) + \Gamma(\text{LORENTZIAN})$$

TABLE 4.1

GAUSSIAN AND LORENTZIAN COMPONENTS OF VOIGT FUNCTION FIT TO IF BAND PASS FILTERS OF SPECTRUM ANALYZER.

NOMINAL BANDWIDTH	GAUSSIAN FWHM (kHz)	LORENTZIAN FWHM (kHz)
3	2.645 ± .036	0.622 ± .016
10	8.871 ± .006	2.008 ± .011
30	27.862 ± .146	5.784 ± .036
100	92.327 ± .269	10.980 ± .011
300	247.331 ± .719	19.628 ± .148

Figure 4.4: 100 kHz IF filter. The circles are the measured transfer function - normalized power vs. frequency. The solid curve is the best Voigt function fit - eqn. 4.3a.

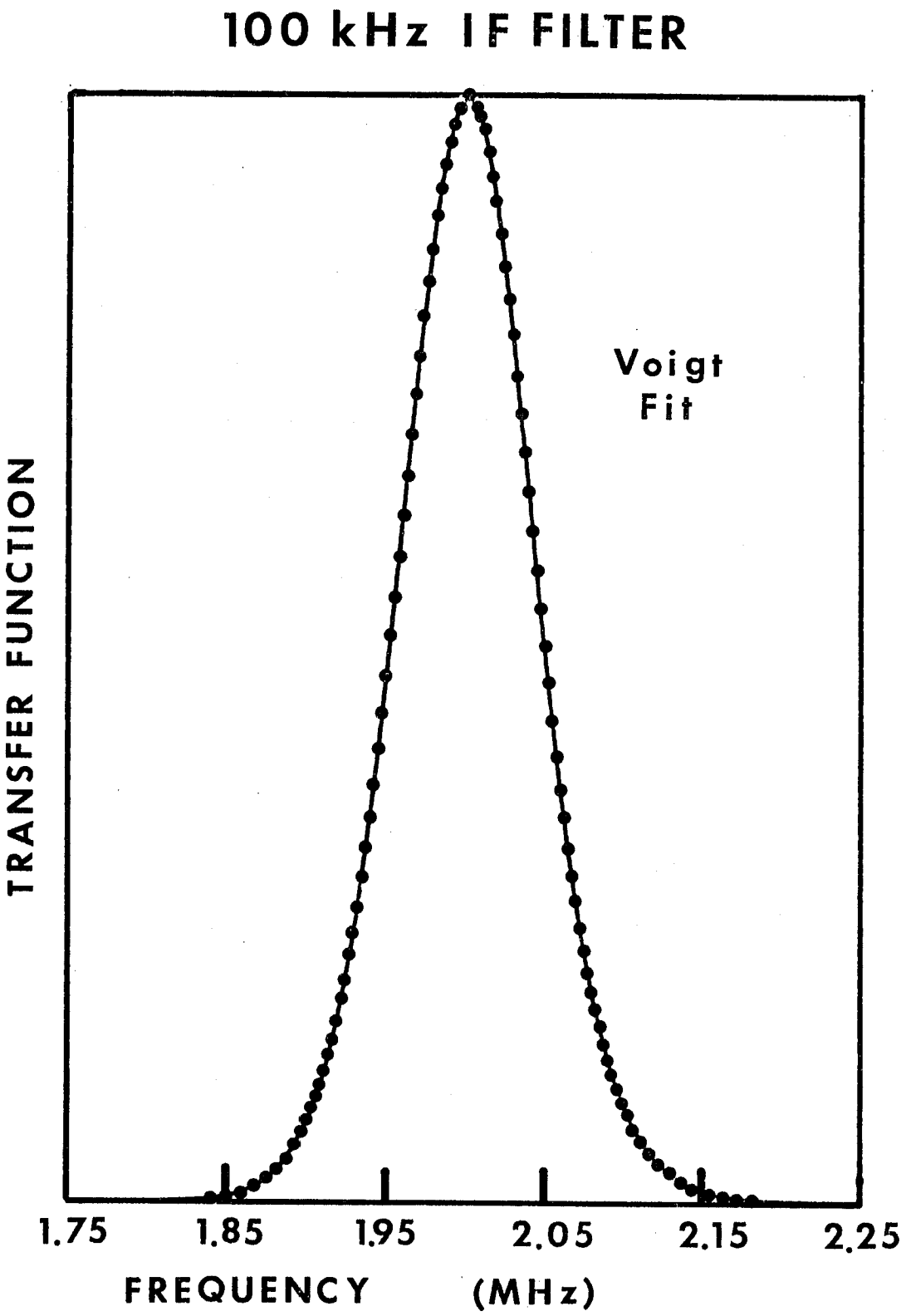
100 kHz IF FILTER
Voigt
Fit
TRANSFER FUNCTION
1.75
1.85
1.95
2.05
2.15
2.25
FREQUENCY (MHz)

C. Optical Instrumental Response

1. Aperture Broadening

Yeh considered the effect of a finite collection aperture on the spectrum of Brillouin scattered light. In rectangular coordinates, the momentum transfer vector $\vec{q}$ becomes:[19]

$$\vec{q} = k_o\left[(\sin\theta - \sin\delta\cos\psi)\hat{X} - \sin\delta\sin\psi\hat{Y} + (\cos\theta - \cos\delta)\hat{Z}\right]$$

where k_o is the incident wavevector.

The spectral function $S(q,\omega)$ must then be modified according to:

$$S(q,\omega) = \int^{\psi}\int^{\delta} S(\theta,\delta,\psi,\omega)\, d\delta\, d\psi$$

and was shown by Yeh to be distinctly non-Lorentzian. For a circular aperture, $0 \leq \psi \leq 2\pi$ and δ (half angular field of view) was fixed at 3°. The ratio of the calculated linewidth to the ideal Lorentzian width ($\delta = 0$) for several scattering angles θ was determined for typical parameter values. Even for $\theta = 90^\circ$, the error introduced was over 50% of the Lorentzian width.

For the geometry of the present experiment, there is an uncertainty in q due to the finite width of the slit (in θ direction) over the PMT, which was 39μ. The slit may be taken to be a rectangular function to good approximation:

$$R(\nu) = \begin{cases} 1 & |\nu| \leq \text{constant} \\ 0 & \text{otherwise} \end{cases} \qquad 4.10$$

The constant was determined from the simple geometry as

follows. The position of the detector is determined from :

$$\tan\theta = \frac{r}{f} \approx \theta \qquad 4.11$$

where r = radial distance from $\hat{z}$

f = focal length of lens

Then, simply, $\Delta\theta = \Delta r / f = W/f$ where W is the slit width. Now from $\omega = q\,v$ obtain:

$$\nu_B = (4\pi/\lambda)\sin\theta/2$$

$$\Delta\nu = ((\nu\cos\theta/2)/\sin\theta/2)\,\Delta\theta/2 \approx \nu\Delta\theta/\theta$$

$$\Delta\nu = \nu_B W/(f\theta) = \nu_B W/r \qquad 4.12$$

The constant in 4.10 is $\nu_B W/r$ where ν_B is the Brillouin line center frequency.

The convolution integral for this part of the instrumental response was done explicitly through numerical integration, and will be displayed in the final result for the observed spectrum.

2. Diffraction Broadening

The finite divergence of the laser beam itself introduces an uncertainty in the momentum transfer vector $\vec{q}$, which in turn induces an uncertainty in the determination of the Brillouin frequency. The importance of this effect has been discussed by Chu[20] and Swinney.[21]

For transverse modes of circular geometry, the electric field distribution of the $TEM_{p\ell q}$ mode is:[22]

$$E(r,\phi) = E_o\,(\sqrt{2}\,r/w(z))^{\ell}\;\; L_p^{\ell}\,(2r^2/w^2)\,\exp(-r^2/w^2(z)) \times \begin{pmatrix}\sin\ell\phi \\ \text{or} \\ \cos\ell\phi\end{pmatrix}$$

where L^{ℓ} = Laguerre polynomial

$w(z)$ = beam waist radius

Thus, for TEM_{00q}, the electric field becomes:

$$E(r, \phi) = E_o \exp(-r^2/w^2(z))$$

and

$$I(r) = |E_o|^2 \exp(-2r^2/w^2) = I_o \exp(-2r^2/w^2) \quad 4.13$$

The intensity radial distribution function I(r) of such a beam is Gaussian. The divergence of a Gaussian beam is:[23]

$$\theta_{Div} = \lambda/(w\pi) \quad \text{(half angle)} \quad 4.14$$

Now the distribution function in frequency space may be determined as follows. The Fourier transform of the intensity distribution function to the scattered wavevector space, q, is

$$I(q) = 1/(2\pi)\int_{-\infty}^{\infty} I(r) e^{-iqr}\, dr = \frac{I_o}{2\pi}\int_{-\infty}^{\infty} e^{-2r^2/w^2} e^{-iqr}\, dr$$

$$= I' \exp(-q^2w^2/8) \quad 4.15$$

This is another Gaussian distribution, as expected. In general, $\omega = 2\pi\nu = qv$; but, v will be determined from the Brillouin frequency which for fixed q is $v = 2\pi\nu_B/q$. Further, $q = \frac{4\pi}{\lambda} \sin\theta/2, \approx 2\pi\theta/\lambda$ for small angles. The beam waist radius is obtained from 4.14. Substituting these expressions into 4.15, obtain

$$I(\nu) = I' \exp(-(1/8)(2\theta\nu/(\theta_{DIV}\nu_B))^2) \quad 4.16$$

The HWHM of this distribution is:

$$\nu_{HWHM} = \sqrt{2\ln 2}\,(\theta_{DIV}/\theta)\,\nu_B \quad 4.17$$

To determine θ_{DIV}, a number of experiments were performed under conditions to maximize this diffraction broadening effect. To minimize the Lorentzian contribution to the observed width, data were taken at $\Delta T = 10^{o}K$ where the intrinsic Brillouin component was expected to be only 0.54 kHz (HWHM). Using an electronic bandwidth of ~ 3 kHz, which had only a 0.3 kHz Lorentzian component, the total expected Lorentzian HWHM was 0.84 kHz. This same electronic filter had a Gaussian HWHM of 1.82 kHz. From 4.17, the diffraction broadening is greatest at low θ, so data were collected at the smallest angle. Finally, an 18μ slit was used over the PMT to minimize aperture broadening. It was expected that the total observed width would be due to Gaussian diffraction broadening and the small Gaussian electronic component.

The mean HWHM of the diffraction broadening effect was determined to be 46.16 kHz at a frequency of 1.847 MHz. Solving 4.14 for θ_{DIV}, the half angle beam divergence was:

$$\theta_{DIV} = 1.237 \times 10^{-4} \text{ radian} \qquad 4.18$$

which corresponds to a scattering column of 1.26 mm in diameter from 4.14. This number was then taken to be constant for all subsequent experiments. The amount of diffraction broadening under other conditions was determined from the Brillouin frequency through 4.17.

3. Misalignment

Errors due to misalignment could be accounted for by taking spectra on opposite sides of the optic axis on the same annulus, under identical conditions (temperature, bandwidth, etc.). Note that the light scattered into the entire annulus

could not be collected and analyzed at once since this would destroy the coherence area requirement. The individual spectra were analyzed separately and the results for the linewidth and frequency shift averaged together.

D. Reduction Of Observed Spectrum

1. Convolution Integral

The complete observed spectrum may now be put together from the separate instrumental effects using equation 4.1. Recall that the spectra were partially reduced by normalizing them to the PMT electronic transfer function in section B.3.

Briefly, the remaining instrumental effects took on the following functional forms:

$$I(\text{optical}) = I(\text{Aperture}) * I(\text{Diffraction})$$

$$I(\text{Aperture}) = \text{rectangular} \qquad 4.10$$

$$I(\text{Diffraction}) = \text{Gaussian} \qquad 4.16$$

$$I(\text{Electronic}) = \text{Voigt} \qquad 4.3a$$

and

$$I(\text{Brillouin}) = \text{Lorentzian} \qquad 4.3c$$

Three useful convolution properties can simplify the analysis. First, the convolution operation is distributive: (24)

$$F * (G*H) = (F*G) * H$$

Second, the convolution of any number of Gaussians is another Gaussian whose total linewidth (HWHM) is: (10)

$$\beta_{\text{total}}(G) = \left(\sum_i (\beta(G)_i)^2\right)^{1/2}$$

Last, the convolution of any number of Lorentzians is another Lorentzian whose total linewidth (HWHM) is: (10)

$$\beta_{\text{total}}(L) = \sum_i (\beta(L)_i)$$

It was shown in 4c that the convolution of a Gaussian and Lorentzian was a Voigt function. Using these results, it is readily seen that the observed spectrum should be a Voigt function convolved with a rectangular function multiplied by an overall factor, Io, plus a background constant, B:

$$I(\text{Observed}) = I_0(I(\text{Voigt}) * I(\text{Rectangular})) + B \qquad 4.19a$$

where $I(\text{Voigt}) = I(\text{Brillouin}) * I(\text{Electronic}) * I(\text{Diffraction})$

$$\beta_{\text{total}}(L) = \beta_{\text{Elec.}}(L) + \beta_{\text{Brillouin}}(L) \qquad 4.19b$$

$$\beta_{\text{total}}(G) = (\beta_{\text{Elec.}}(G)^2 + \beta_{\text{Diffraction}}(G)^2)^{1/2} \qquad 4.19c$$

The total observed width is that of the function which is the convolution of the Voigt and rectangular functions, and for which there is no simple expression.

By definition, the convolution of the Voigt function, V, with the rectangular function, R is:[25]

$$C(\nu) = \int_{-\infty}^{\infty} V(\nu') R(\nu - \nu_B - \nu')\, d\nu'$$

where $$R(\nu - \nu_B - \nu') = \begin{cases} 1 & |\nu - \nu_B - \nu'| \le \nu_B W/r = A \\ 0 & \text{otherwise} \end{cases} \qquad 4.20$$

$V(\nu')$ = normalized Voigt lineshape

Rearranging the argument of R, it is seen that:

$$C(\nu) = \int_{\nu - \nu_B - A/2}^{\nu - \nu_B + A/2} V(\nu')\, d\nu'$$

Then the observed spectrum is, from 4.19 a:

$$I_{OBS}(\nu) = I_o \int_{\nu-\nu_B-A/2}^{\nu-\nu_B+A/2} V(\nu')\,d\nu' + B \qquad 4.21$$

This function has five free parameters:

β(G) = total Gaussian HWHM

β(L) = total Lorentzian HWHM

ν_B = Brillouin center frequency

I_o = overall multiplicative constant

B = overall additive constant

Note that A is determined from ν_B and the constants W and r per experiment. $V(\nu)$ is the lineshape function normalized so that:

$$\int_{-\infty}^{\infty} V(\nu)\,d\nu = 1$$

and was represented earlier by 4.3a.

If these parameters are determined through some fitting procedure, then the velocity is determined from:

$$V = 2\pi\nu_B/q\,, \quad q = 4\pi \sin\theta/2/\lambda \qquad 4.22$$

and the total amplitude attenuation (per unit wavelength) is:

$$\alpha_\lambda = \left(\beta(L) - \beta_{ELEC}(L)\right) 2\pi/\nu_B \qquad 4.23$$

where β(L) = total Lorentzian width.

2. Generating The Fitting Function

a. Voigt function algorithm

Kielkopf's approximant to the Voigt function was

found inadequate when used in the convolution expression for the fitting function, eqn 4.21. The range of the linewidth parameters which makes this an adequate approximant was not clearly defined by Kielkopf. It is known that the Voigt function is more easily and accurately generated for certain values of the ratio $\beta(L)/\beta(G)$ than for others.[26] In particular, in the limit that the Lorentzian linewidth approaches zero, the Lorentzian lineshape becomes a representation of the Dirac delta function.[27] Thus, for small $\beta(L)$, the Voigt function will be difficult to compute since one is attempting to deconvolve two functions near a singularity of one of the functions. Analytic continuation can be used to avoid this problem. These and other numerical problems were carefully considered by Armstrong[26] who gave an explicit algorithm for generating the Voigt function for all possible ranges of the parameters $\beta(L)$ and $\beta(G)$ and accurate to 1 part in 10^6. His Fortran program was used exactly as given for generation of the Voigt function for the convolution integral.

Armstrong's dimensionless Voigt function is given as:[26]

$$K(X,Y) = \frac{Y}{\pi}\int_{-\infty}^{\infty}\frac{e^{-t^2}\,dt}{Y^2+(X-t)^2} \qquad 4.24$$

$$\frac{1}{\pi^{1/2}}\int_{-\infty}^{\infty} K(X,Y) = 1$$

$$Y = \left(\beta(L)/\beta(G)\right)\sqrt{\ln 2}$$

$$X = \frac{\nu-\nu_B}{\beta(G)}\sqrt{\ln 2}$$

$\beta(G)$ = HWHM (not 1/e WIDTH)

The algorithm calculates K(x,y) by three different numerical methods depending on relative values of x and y. These are as follows:

1) $Y<1 \quad X<4 \quad \text{AND} \quad Y < 1.8/(X+1), \; X>4$

$$K(X,Y) = Re\left[W(Z)\right]$$

where

$$W(Z) = e^{-Z^2} + \frac{2i}{\sqrt{\pi}} F(Z)$$

$$K(X,Y) = Re\left[e^{-Z^2}\right] + \frac{2}{\sqrt{\pi}} Im\left[F(Z)\right]$$

$$F(Z) = e^{-Z^2}\int_0^Z e^{t^2}\,dt \qquad \text{DAWSON'S FUNCTION}$$

$$Im\left[F(Z)\right] = d_1 Y - d_3 Y^3 + d_5 Y^5 - \cdots$$

and the Taylor series coefficients dn are given by the relation

$$d_0 = F(X)$$

$$d_1 = 1 - 2X d_0$$

$$d_n = -\frac{2}{n}\left(X d_{n-1} + d_{n-2}\right) \qquad n \geq 2$$

if $Y<1$ or $Y < 1.8/(X+1)$ but $X>5$, then a Chebyshev expansion of Dawson's function, due to Clenshaw, is used.

2) $1.0 < Y \leq 2.5, \quad X \leq 4$

$$K(X,Y) = \frac{1}{\pi}\int_{-\infty}^{\infty} e^{-t^2}(4t^2-2)\left[(t-X)\,TAN^{-1}\left(\frac{t-X}{Y}\right) - \frac{Y}{2}\log\left(Y^2+(t-X)^2\right)\right]dt$$

this effects a smoothing of the delta function like behavior for small y. The factors in the expansion give a form which is integrable using a 20 term Gauss-Hermite quadrature.[28] The quadrature points are the roots of the Hermite polynomial.

3) $Y \geq 2.5,\ X<4 \quad or \quad Y > 1.8/(X+1),\ X>4$

$$K(X,Y)$$

is integrated directly using a 20 term Gauss Hermite quadrature

$$K(X,Y) = \int_{-\infty}^{\infty} e^{-t^2} F(X,Y,t)\, dt$$

where $$F(X,Y,t) = \frac{Y}{\pi} \frac{1}{Y^2 + (X-t)^2}$$

x,y are constants for this integration, F(x,y,t) is the kernal of the Hermite integral where e^{-t^2} is the weighting factor; the same coefficients (roots and weights) of region 2 are used here.

b. Trapezoidal Rule Integration

The integral over ν in 4.21

translates into an integral over x in Armstrong's notation as follows:

$$I_{OBS}(\nu) = I_o \int_{(\nu-\nu_B-A/2)\sqrt{\ln 2}/\beta(G)}^{(\nu-\nu_B+A/2)\sqrt{\ln 2}/\beta(G)} K(X,Y)\, dX + B \qquad 4.25$$

A simple trapezoidal rule approximation for this integral was adequate.[29] A test program was run using 10 and 100 points in the trapezoidal expansion. Assuming that the 100 point expansion gave greater accuracy, the 10 point expansion integral differed from the 100 point expansion by only $2 \times 10^{-3}\%$. Thereafter, the 10 point expansion was used. Equation 4.25 becomes, using the trapezoidal rule:

$$I_{OBS}(\nu) \approx \Delta X \left[\tfrac{1}{2} K(X_0, Y) + K(X_1, Y) + \cdots + K(X_9, Y) + \tfrac{1}{2} K(X_{10}, Y) \right]$$

$$\Delta X = \frac{A\sqrt{\ln 2}}{n\,\beta(G)}$$

$$X_n = (\nu - \nu_B - A/2)\frac{\sqrt{\ln 2}}{\beta(G)} + n\,\Delta X$$

$$n = 0, \cdots 10$$

3. Weighting Factor

The proper weighting factor must be obtained from a detailed consideration of all noise sources. Now the detection process is photo-electric and any discussion of error in the process must necessarily involve the probability distribution, p(n,T), of emission of n photoelectrons (from the photocathode) in a time T. Mandel[30] determined what p(n,T) should be, given the intensity $I(t) = E^*(t)E(t)$, where E(t) is the complex analytic signal. His result was:

$$p(n,T) = \int_0^\infty \frac{(\epsilon U)^n}{n!} e^{-(\epsilon U)} p(U)\, dU \qquad 4.27$$

$$U = \int_0^T I(t)\, dt$$

$p(U)$ = probability distribution for intensity $I(t)$

ϵ = overall heterodyne efficiency

A consequence of this was (by consideration of factorial moments):[31]

$$\sigma_n^2 = \langle n \rangle + \epsilon^2 \langle (\Delta U)^2 \rangle \qquad 4.28$$

This is the expression for the variance of the photoelectron count and is the quantity of interest. This shows that the error in the counting of photoelectrons depends on the statistics of the field ($\langle (\Delta U)^2 \rangle$) as well as the classical Poisson distribution result, $\langle n \rangle$.

The field incident on the photocathode consists of the Brillouin scattered light and two local oscillators: the elastically scattered laser light and the Rayleigh scattering from xenon. Now the laser is amplitude stabilized to 0.3%, so that the fluctuations for this source may be neglected. For the Rayleigh and Brillouin scattering, care must be given to the statistics of the physical process. For a liquid far from T_c, the light scattered follows the statistics of a Gaussian source (i.e. a Gaussian distributed random variable; a consequence of the central limit theorem).[32] Near T_c however, the statistics are expected to be non-Gaussian.[33] However, there is no clearly developed theory for the form of these statistics, and one would presumingly have to observe no more than a single coherence

length in the fluid to detect any departure from Gaussian. Therefore, Gaussian statistics will prevail for the fluid as a whole both near and far from T_c.

For a stationary Gaussian process,[34]

$$p(I) = \frac{1}{\langle I \rangle} \exp(-I/\langle I \rangle)$$

where p(I) is a probability function. The probability of interest is p(U), where U is the integrated intensity, and in general no simple expression for this exists. However, asymptotic relations for p(U) may be derived if the averaging time T is very large or very small compared to the coherence time of the source. For the present experiment, the coherence time of the source is approximately the reciprocal of the Rayleigh linewidth:

$$\tau_{coh} \approx 1/\Gamma_R$$

Now the Rayleigh linewidth changes as a function of the temperature. From the work of D. Henry[35],

$$\Gamma_R = 2.2 \times 10^5 \text{/sec} \qquad \text{for } \Delta T = 5.00^\circ$$

$$\Gamma_R = .34 \times 10^5 \text{/sec} \qquad \text{for } \Delta T = 0.05^\circ$$

The averaging time (per channel) T, was 10 ms so that,

$$T(=10 \text{ ms}) \gg \tau \sim (1/\Gamma_R) = \begin{cases} 4.6\,\mu s & \Delta T = 5^\circ \\ 29\,\mu s & \Delta T = .05^\circ \end{cases}$$

When $T \gg \tau$, p(U) may be represented approximately as:[36]

$$p(U) = \delta(U - \langle U \rangle)$$

and from eqn. 4.27 p(n,T) is given as:

$$p(n,T) = \frac{\langle n \rangle}{n} \exp(-\langle n \rangle)$$

and $\sigma_n^2 = \langle n \rangle$

Thus, one has the result that the statistics of the field results in a Poisson photoelectron emission probability where the error in the number of photoelectrons is simply $\sqrt{\langle n \rangle}$.

Next, consider the statistics of the PMT. The number of photoelectrons ejected from the photocathode, $\langle n_c \rangle$, is:[37]

$$\langle n_c \rangle = \epsilon \langle n_p \rangle$$

where ϵ is the heterodyne efficiency (which includes the quantum efficiency) and $\langle n_p \rangle$ is the average number of photons incident. For the PMT as a whole, the average number of electrons collected at the anode, $\langle n_a \rangle$, is:[37]

$$\langle n_a \rangle = \epsilon \langle n_p \rangle G$$

where G is the average gain of a k stage PMT having a gain per stage of δ . The variance is:[37]

$$\sigma_a^2 = \epsilon \langle n_p \rangle \delta^{2k} (1 + 1/(\delta - 1))$$

assuming equal gain per stage. Now the current out of the anode is:

$$i_a = \langle n_a \rangle e/T = eG\epsilon \langle n_p \rangle /T$$

e = electronic charge

Therefore,

$$\sigma_{i_a}^2 = i_a \delta^k (1 + 1/(\delta - 1))e/T$$

The photocurrent is developed as a voltage for the spectrum analyzer, so that the input voltage is simply $i_a R$, R the resistance. The output of the spectrum analyzer is swept into the FABRITEK as a voltage with some voltage gain g, so that the signal averager sees a voltage of:

$$V_i = g(i_a)_i R$$

per channel i. Note that the error in this voltage is simply:

$$\sigma_{V_i} = gR(\sigma_{i_a})_i$$

Now the quantity that is needed in the chi-squared minimization is the power, not the voltage, so that if y_i is the power, then:

$$y_i = V_i^2/R$$

The weighting factor in the expression for chi-squared must be modified as:

$$\sigma_{Y_i} = \left(\frac{\partial Y_i}{\partial V_i}\right) \sigma_{V_i} = (2 V_i/R)\sigma_{V_i}$$

$$\sigma_{Y_i}^2 = (4 Y_i/R)\sigma_{V_i}^2 = 4 Y_i g^2 R (\sigma_{i_a})_i^2$$

Since $V_i = (y_i R)^{1/2}$, then:

$$\sigma_{Y_i}^2 = 4gR^{1/2}(e/T)\delta^K(1+1/(\delta-1))Y_i^{3/2}$$

This is the desired result. The variance is expressed in terms of the quantity measured (y_i) and known constants. Finally, since the signal is averaged, the absolute value of the noise is increased above that of the single sweep noise by $\sqrt{M}$, where M is the number of sweeps. The final weighting factor expression is:

$$\sigma_{Y_i}^2 = M4gR^{1/2}\delta^K(1+1/(\delta-1))Y_i^{3/2}(e/T) \quad 4.29$$

where M = number of sweeps

g = voltage gain of spectrum analyzer

δ = current gain per stage, PMT

k = 10 stages

R = 25 ohms

T = .01 sec

e = 1.67×10^{-19} Coulombs

y_i = total number counts in channel i (after squaring) and $W_{y_i} = 1/\sigma^2_{y_i}$

4. Reduction Of Parameter Number

The method is now described by which the number of parameters left free to vary was reduced from five to three. Note that the Gaussian contribution to the observed width is entirely instrumental. The IF filter linewidths were measured accurately; the diffraction broadening effect could be calculated from the value assumed by the Brillouin frequency from equation 4.17. Thus, the parameter $\beta(G)$ was always determined from known constants and ν_B. This left four parameters free to vary. The frequency ν_B could be determined readily as follows.

An accurate plot of every power spectrum was made on a CALCOMP 565 plotter. From this, a good first estimate of the Brillouin frequency was made, accurate to $\sim 3\%$. Values for the remaining parameters, the intensity and background, were then assumed and the value for χ^2 for the particular choice of parameters calculated. A plot of the fitting function was made over the power spectrum using a Hewlett Packard 7202A XY plotter on line to the PDP 10. Using this plotter in conjunction with the calculated values of χ^2, the parameters were varied until a reasonably close fit was

obtained. The Brillouin frequency was then varied with the remaining parameters fixed until ν_B was determined to $\sim$ 0.1% by searching the changes in χ^2 for a minimum. Thereafter, ν_B was held fixed, and only the Lorentzian linewidth $\beta(L)$, background, and intensity left to vary.

As a check on the determination of ν_B, the initial guesses arrived at above were put into the fitting program that follows below. The predicted values for the intensity, background, and Lorentzian width were then used (to three significant figures) in the plotting program again and was then stepped off at increments of 1 kHz ($\sim$ 0.1%) and the changes in χ^2 noted. If a lower minimum value of χ^2 was obtained than previously, this value of ν was taken as the correct Brillouin shift. Generally, only one such corrective step was needed.

5. Marquardt's Algorithm - Optimization of Other Parameters

a. Mathematical Basis Of Algorithm

Marquardt's algorithm interpolates between a Newton-Raphson (or analytical) method and a gradient method and is more efficient than either. Consider for the moment any function $F(\vec{X})$, which may be nonlinear, and expand it in a Taylor series to first order terms. The quantity $\vec{X}$ contains both variables x_i and parameters, P_j. The extrema in the parameters are found by taking the partial derivatives of $F(\vec{X})$ and setting the result equal to zero:[38]

$$\frac{\partial}{\partial P_i} F(\vec{X})\Big|_{\vec{X}=\vec{P}_0} + \sum_j \frac{\partial^2}{\partial P_i \partial P_j} F(\vec{X})\Big|_{\vec{X}=\vec{P}_0} \delta\vec{P} + O(\delta^2) = 0 \qquad 4.30$$

where $\vec{P}_0$ are the given initial values of the parameters of $F(\vec{X})$. This equation may be written in matrix form as:

$$\vec{g} + G\,\delta\vec{P} + O(\delta^2) = 0 \qquad 4.31$$

where

$$\vec{g} = \frac{\partial}{\partial x_i} F(\vec{X})\Big|_{\vec{X}=\vec{P}} \qquad \text{(gradient)} \quad 4.32$$

$$G_{ij} = \frac{\partial^2}{\partial x_i \partial x_j} F(\vec{X})\Big|_{\vec{X}=\vec{P}} \qquad \text{(curvature)} \quad 4.33$$

Solving for the changes in the parameters $\delta\vec{P}$:

$$\delta\vec{P} = -G^{-1}(\vec{g} + O(\delta^2))$$

so that the n^{th} iteration for the parameters $\vec{P}$ should be given by:

$$\vec{P}^{(n+1)} = \vec{P}^{(n)} - G^{-1}\vec{g}^{(n)} \qquad 4.34$$

Now this scheme of successive iteration of the parameters $\vec{P}$, based on a Taylor series expansion of the function to first order about the current approximation, is called a Newton-Raphson method. Its advantages are that convergence is ultimately quadratic, and that it is invariant under linear transformation of its variables. The disadvantages are that convergence cannot be forced from a poor initial approximation, the second derivatives of the function must exist and must be computed, and if G is singular, the scheme breaks down.

Usually, because of poor initial guesses, only a fraction, λ, of the predicted change in the parameter is

used for the next iteration:

$$\vec{p}^{(n+1)} = \vec{p}^{(n)} - \lambda G^{-1} \vec{g}^{(n)} \qquad 4.35$$

Now if the matrix G is taken to be the identity matrix then one obtains the gradient method:

$$\vec{p}^{(n+1)} = \vec{p}^{(n)} - \lambda \vec{g}^{(n)} \qquad 4.36$$

because $\vec{g}$ is the gradient vector. The direction which the correction follows is the direction of steepest descent, which is opposed to the gradient. Advantages to this method are that second derivatives are not needed, and that it will converge (generally) from a poor approximation. The disadvantages are that convergence can be extremely slow (or not at all) and that the scheme depends on the metric (scaling of the variables).

These two methods have been widely used for optimization problems, including optimization of χ^2. But for χ^2 certain advantages result since it is the result of a sum of squares. Write χ^2 as follows (neglecting for the moment the weighting factors W):

$$\chi^2 = \chi^2(y_K, F(\nu_K, P_j)) = \sum (y_K - F(\nu_K, P_K))^2$$

$$\chi^2 = \sum f_K^2 \qquad 4.37$$

where (ν_K, y_K) = data pair, k = 1-195

ν = frequency, y = power spectral density

P_j = parameters

and $F(\nu_K, P_j)$ = fitting function, convolution integral of eqn. 4.25.

Now substituting χ^2 into eqn. 4.30 obtain:

$$\sum_K \frac{\partial f_K}{\partial P_i} f_K + \sum_j \left(\sum_K \frac{\partial f_K}{\partial P_i} \frac{\partial f_K}{\partial P_j} + f_K \frac{\partial^2 f_K}{\partial P_i \partial P_j} \right) \delta P_j + O(\delta^2) = 0$$

In the immediate neighborhood of a minimum, $f_K(\vec{P} + \delta \vec{P}) = 0$, and f_K is of the order of $\delta \vec{P}$ and $\frac{\partial^2 f_K}{\partial P_i \partial P_j}$ may be absorbed into $0(\delta^2)$. If $f_K(\vec{P} + \delta \vec{P}) \neq 0$, then quadratic convergence is lost if $\partial^2 f_K / \partial P_i \partial P_j$ is neglected, but there is a substantial gain in computation since second derivatives are not needed.

Rewriting terms for matrix notation:

$$G_{ij} = 2 \sum_K \frac{\partial f_K}{\partial P_i} \frac{\partial f_K}{\partial P_j}$$

$$\vec{g} = \sum_K \frac{\partial f_K}{\partial P_i} f_K$$

so that

$$\vec{g} + G \delta \vec{P} + O(\delta^2) = 0$$

and

$$\vec{P}^{(n+1)} = \vec{P}^{(n)} - \lambda G^{-1} \vec{g}^{(n)}$$

The advantages here for χ^2 are that second derivatives are not needed, and since G is usually positive definite, the correction to $\vec{P}^{(n)}$ is in the direction of descent in the space of the variables.

Now Marquardt's variation of this method is:[39]

$$\vec{p}^{(n+1)} = \vec{p}^{(n)} - (G + \lambda I)^{-1} \vec{g}^{(n)} \qquad 4.38$$

$$\text{i.e.} \quad \delta\vec{p}^{(n+1)} = -(G + \lambda I)^{-1} \vec{g}^{(n)} \qquad 4.39$$

In three theorems, Marquardt proved:

1) for $\lambda \geq 0$, $\delta\vec{P}$ is the radius vector of a sphere in parameter space such that $\chi^2(\delta\vec{P})$ is a minimum

2) $\delta\vec{P} = \delta\vec{P}(\lambda)$ i.e., $\delta\vec{P}$ is a continuous decreasing function of λ such that as $\lambda \to \infty$ $|\delta\vec{P}(\lambda)| \to 0$.

3) if γ is the angle between $\delta\vec{P}$ obtained by Marquardt's method and $\delta\vec{P}$ obtained using the gradient method (eqn. 4.36), then γ is a monotonically decreasing function of λ such that as $\lambda \to \infty$, $\gamma \to 0$.

The implications of this method are that by choosing λ properly, one interpolates between the gradient and analytical methods. For large λ, the $(G + \lambda I)$ matrix is dominated by the diagonal elements, λI. Then as $\lambda \to \infty$, $\delta\vec{P} \longrightarrow \vec{g}/\lambda$, so that $\delta\vec{P}$ and $\vec{g}$ become proportional and the angle between them approaches zero. On the other hand, if $\lambda \to 0$, $\delta\vec{P}$ and $\vec{g}$ meet at some finite angle γ such that as $\lambda \to \infty$, $\gamma \to 0$. Marquardt monitored γ for different problems and found that, usually, $80^\circ < \gamma < 90^\circ$. That is, the correction vectors predicted using the gradient and analytical methods are almost always 90° apart. Thus, Marquardt's method inherits the advantage of the other two methods while not picking up the disadvantages. However, the choice for λ is unclear, and a change of scale is necessary because the algorithm is

gradient-like.

Since the gradient is not scale invariant, the parameter space must be scaled and a suitable choice is units of standard deviations of the derivatives: $\partial f_K / \partial P_j$. Then G is transformed into the matrix of simple correlation coefficients among $\partial f_K / \partial P_j$:

$$G_{scaled_{jj'}} = \frac{G_{jj'}}{\sqrt{G_{jj} G_{j'j'}}} \qquad g_{j_{scaled}} = \frac{g_j}{\sqrt{G_{jj}}} \qquad \delta P_{j_{scaled}} = \delta P_j / \sqrt{G_{jj}}$$

Regarding the choice of λ, a sufficiently large λ always exists such that a lower value of χ^2 could be found. But, one should not choose λ larger than necessary since the method would then inherit the disadvantages of the gradient method: good initial minimization followed by progressively slower progress. As one approaches the true minimum, the Taylor series becomes more appropriate in describing the behavior of the nonlinear function, and λ should be made smaller to take advantage of the analytical method of solution where the series converges nicely.

b. The Algorithm

The explicit algorithm is as follows:

1) Assume a value for ϵ and λ
2) Compute χ_1^2 from initial guesses for parameters, $\vec{P}$
3) Calculate the gradient vector $\vec{g}$
4) Calculate the matrix G, and scale
5) Add λ to the diagonal elements: ($G_{scale} + \lambda$ I)
6) Invert ($G_{scale} + \lambda$ I)
7) Compute the correction to the parameters, $\delta\vec{P}$, from: $\dfrac{(G_{scale} + \lambda \text{ I})^{-1}\vec{g}}{\sqrt{G_{jj} \; G_{jj}}}$

8) Compute the new values of the parameters $\vec{P}^{(n+1)} = \vec{P}^{(n)} + \delta\vec{P}$ and new value of Chi-squared, χ_2^2

9) Compare χ_2^2 with χ_1^2:

if $\chi_1^2 \geq \chi_2^2$ go to step 10

if $\chi_1^2 < \chi_2^2$ $\lambda^{(n+1)} = \lambda^{(n)} \times 10$

if $\lambda^{(n+1)} > 10^{10}$ stop

if $\lambda^{(n+1)} \not> 10^{10}$ go to step 5

10) replace the parameters with the corrected values and output $\vec{P}$, λ, and current χ^2

if $\left|\frac{\chi_1^2 - \chi_2^2}{\chi_2^2}\right| \leq \epsilon$ and if $\lambda < 10^{-8}$

then convergence achieved

if $\left|\frac{\chi_1^2 - \chi_2^2}{\chi_2^2}\right| > \epsilon$ or $\lambda > 10^{-8}$

then

$\chi_1^2 = \chi_2^2$

$\chi_2^2 = 0$

$\lambda^{(n+1)} = \lambda^{(n)}/10$

go to step 3

c. Discussion of Algorithm

The algorithm is efficient. Note that if $\chi_2^2 \not< \chi_1^2$ in step 9, a new gradient vector and new G matrix need not be computed, only the new value of λ added to the diagonal elements of G, step 5. Also, only a value of χ^2 smaller than the previous value is sought, not a turning point, so that only two successive values of χ^2 and not three are needed. The derivatives for the gradient in step 3 were

computed numerically from Sterling's central difference formula:[40]

$$\frac{\partial f}{\partial \vec{P}} \approx \frac{f(\vec{P}+\Delta\vec{P}) - f(\vec{P}-\Delta\vec{P})}{2\,\Delta\vec{P}}$$

where $\Delta\vec{P}$ = step size guessed from current value of parameters $\vec{P}$. This method is more accurate than either a forward or backward difference formula. In practice, the step size for the derivative was a constant percentage of the current value of the parameter: 25% of the Lorentzian width, 20% of the intensity, and 20% of the background. The matrix inversion for step 6 was accomplished using the program MINV of the IBM Scientific Subroutine Package[7] to single precision arithmetic.

A nominal initial value of $\lambda = .001$ was assumed. The added test in step 9 which stops execution if λ becomes large was found to be better than having the parameters assume unreasonable values. If λ became too large, the algorithm became too much like the gradient method, and convergence thereafter was slow. When λ exceeded 10^{10}, new initial values for the parameters were guessed and the program rerun. The change of λ by a factor of 10 was found to be reasonable (as suggested by Bevington), neither too large nor too small. Finally, the convergence criterion of step 10 sought a small relative change in successive χ^2 values, but only if $\lambda \leq 10^{-8}$. For these small values of λ, it is assured that the algorithm behaved more like an analytic

solution as it should when close to the minimum. ϵ was chosen rather small, 0.01%, but this was necessary to give the precision required in determining the linewidth, as will be discussed further.

It should be recalled that only three parameters were varied using this algorithm: the Lorentzian width, intensity, and background.

d. Usage of Program

In principle, a single run of the program on any spectrum should determine the optimum values of all parameters by finding the absolute minimum value for χ^2. In practice, one run is inadequate. The initial guesses for the parameters may be far from their respective optimum values, the parameters may cluster about a local extremum, and the convergence criterion may be met well before the absolute minimum for χ^2 is reached.

A method which avoids this difficulty and assures the algorithm is functioning properly is the following. χ^2 as a function of a single parameter will assume a parabolic form when near the minimum.[41] This is certainly true for linear problems, and is the basis for the algorithm used in fitting the IF filters in section B.4e. For nonlinear problems, in the region where the analytic (Taylor series) method is expected to adequately represent the fitting function, χ^2 as a function of a single parameter should again assume a parabolic form. Of the parameters varied in the program, the Lorentzian linewidth is the quantity of interest, the multiplicative and additive constants contain no useful information. For every spectrum, the program was rerun with different initial guesses for the three parameters and the changes in χ^2 as a function of the Lorentzian width were monitored. When far from the true minimum, all the parameters were varied erratically, i.e. there were large variations both above and below the optimum values for each parameter. This was the gradient-like portion of the algorithm at work.

When these large deviations averaged out, the program acted analytically, the parameters were optimized more uniformly, λ was reduced monotonically at each iteration, and χ^2_{MIN}, as a function of the Lorentzian width, was approached from only one direction. When the value for χ^2 finally converged within ϵ, the program was again rerun, this time with an initial guess for the Lorentzian width above or below that of the previous guess, depending on the direction the minimization took during the analytic part of the previous search. By this procedure, one is attempting to generate χ^2 versus $\Gamma(L)$ over a range large enough so that it is seen that an extremum is reached for a reasonable value of the width.

Examples of this procedure are illustrated by figures 4.5 and 4.6. Both are plots of the percentage change in χ^2, relative to respective minimum values for χ^2, versus the Lorentzian linewidth, in kHz. The curves were generated from a large number of calculated χ^2 values as the parameters were optimized in small steps en route to their best values. Figure 4.5 is for a spectrum having a very narrow linewidth, $\Gamma(L) = 6.60$ kHz, taken at the highest temperature ($\Delta T = 10^{o}$) and second smallest scattering angle. Figure 4.6 is for a spectrum at the other extreme conditions, having a broad width, $\Gamma(L) = 689$ kHz, taken at the lowest temperature ($\Delta T = 0.05^{o}$) and largest scattering angle. The fact that the curves are parabolic indicates the algorithm is working properly. Similar curves are expected for χ^2 versus the additive or multiplicative constant. For figure 4.6, a 2%

Figure 4.5: Relative change in chi-squared for spectrum at $\Delta T = 10^{o}K$, $\Theta = 0.7^{o}$. Figs. 4.7, 4.9 refer to the same spectrum as this figure.

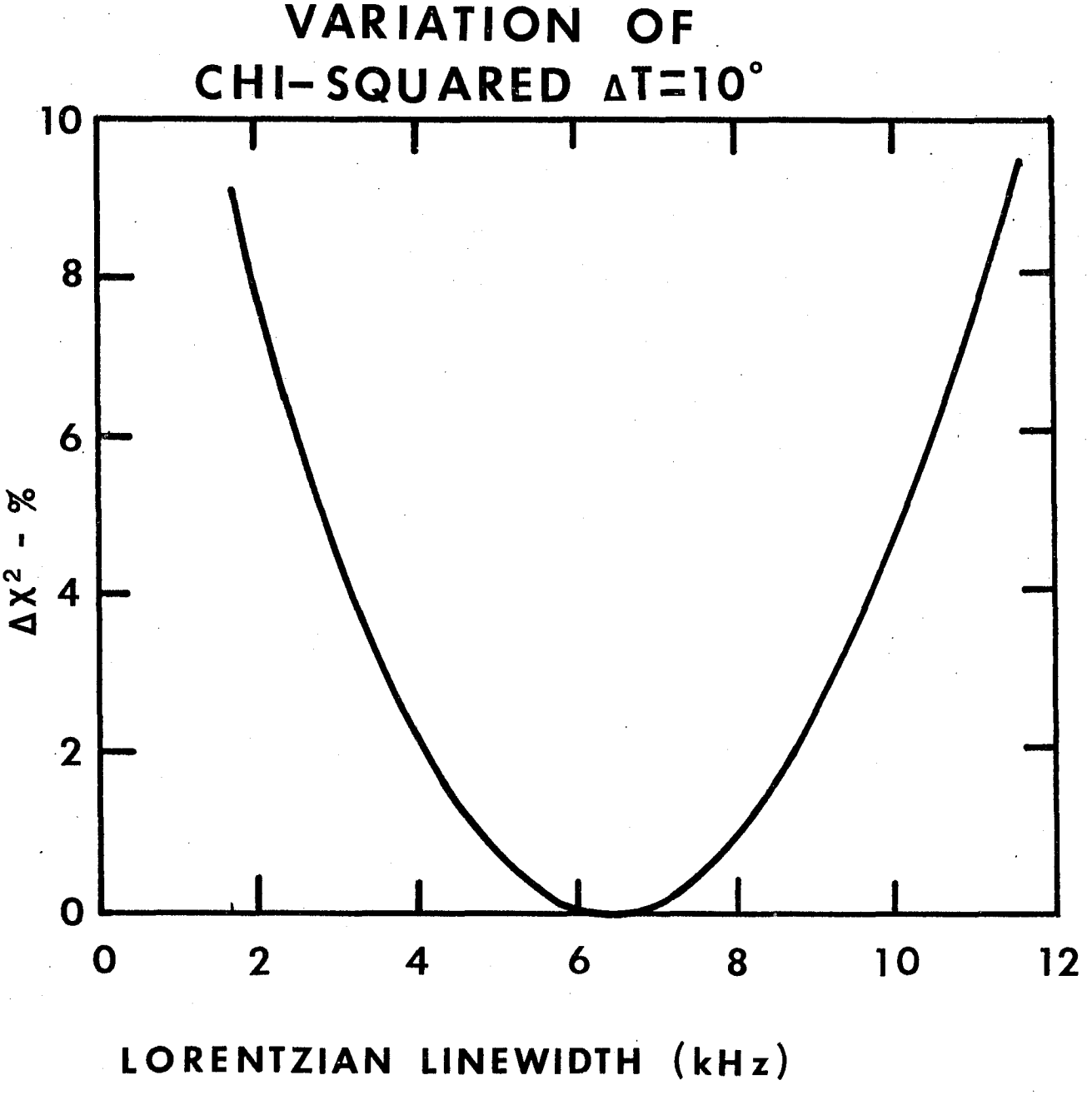
VARIATION OF
CHI-SQUARED ΔT=10°
10
8
6
4
2
0
ΔX² - %
0
2
4
6
8
10
12
LORENTZIAN LINEWIDTH (kHz)

Figure 4.6: Relative change in chi-squared for spectrum at $\Delta T = 0.05^{o}K$, $\theta = 2.7^{o}$. Figs. 4.8, 4.10 refer to the same spectrum as this figure.

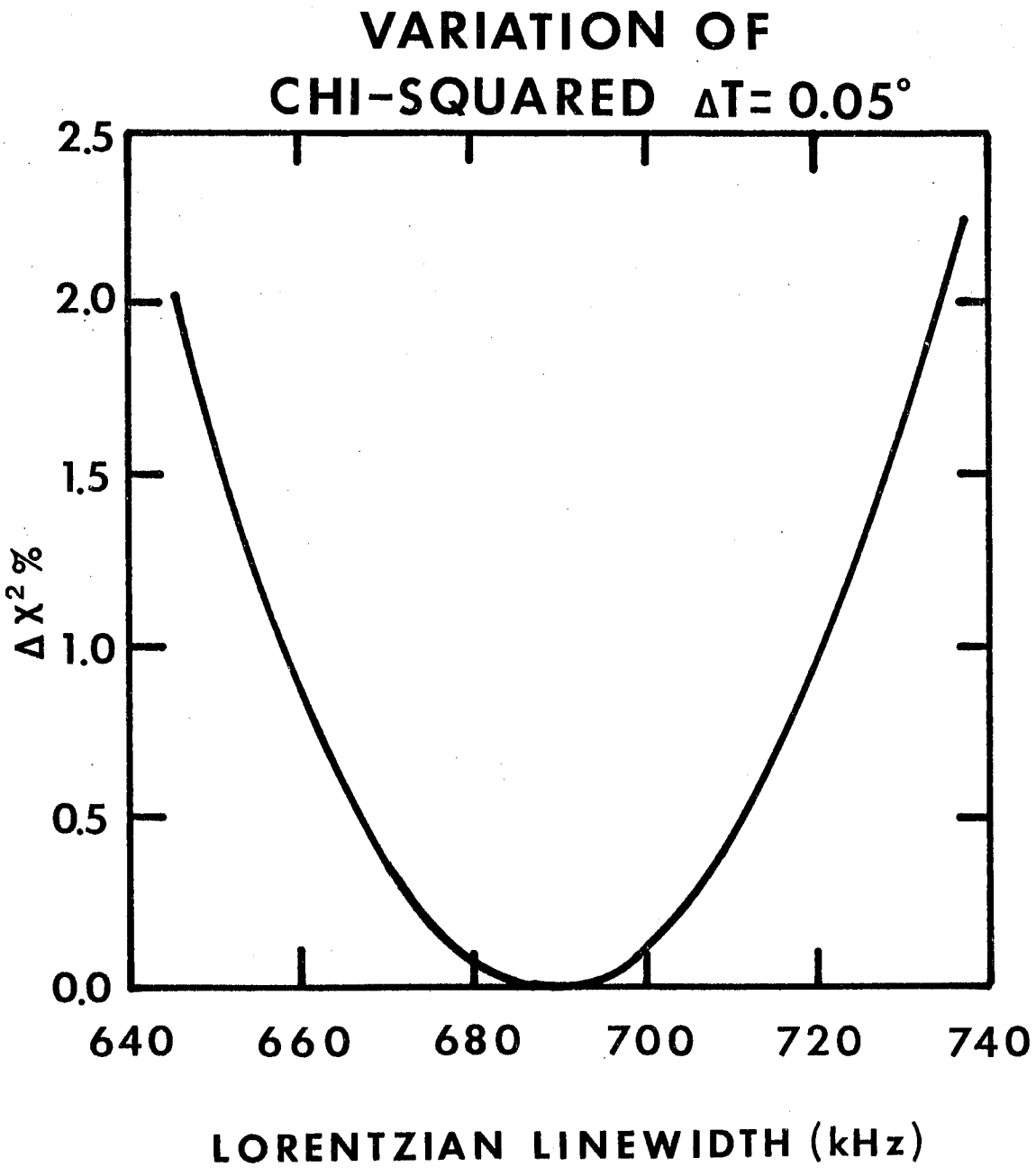
VARIATION OF
CHI-SQUARED ΔT= 0.05°
2.5
2.0
1.5
1.0
0.5
0.0
Δ X² %
640
660
680
700
720
740
LORENTZIAN LINEWIDTH (kHz)

change in χ^2 results in a change of $\sim$ 13% in frequency space, but for figure 4.5, a 2% change in χ^2 results in $\sim$ 69% total change in frequency. Thus, at the narrow linewidths, χ^2 changes rapidly and the convergence criterion is easily met. At the broad widths, the fitting procedure becomes quite tedious, requiring many runs of the program to determine the minimum. For all spectra, guessing the value of the multiplicative constant, given a linewidth, was very difficult as the two were related in a nonlinear way. The background constant could generally be estimated to three significant figures from the CALCOMP plots, and did not change much ($<\pm.1\%$) during the optimization.

Figures 4.7 and 4.8 show deviation plots for the same two spectra. The percentage deviation is:

$$\% \text{ deviation}_i = \frac{(y_i - I_{OBS}(\nu_i))}{I_{OBS}(\nu_i)} \times 100$$

A datum point is (ν_i, y_i) where ν_i = frequency, y_i = power spectral density. $I_{OBS}(\nu_i)$ is the convolution integral expression, eqn. 421 with the best fit values for the parameters evaluated at the datum point ν_i. The goodness of the fit is indicated by the small deviations of the data from the theoretical function. For figure 4.8, the maximum deviations are +0.4% and -0.6%, or 1% total. For figure 4.7, the maximum deviations are +4.9% and -2,4%, or 7.3% total deviation from the best fit values (0% line). The measured spectra are shown in figures 4.9 and 4.10 by jagged lines, and

Figure 4.7: Deviation plot for spectrum at $\Delta T = 10^{o}K$, $\Theta = 0.7^{o}$. Spectrum is shown in fig. 4.9. The zero per cent line is the best fit convolution integral, eqn. 4.21.

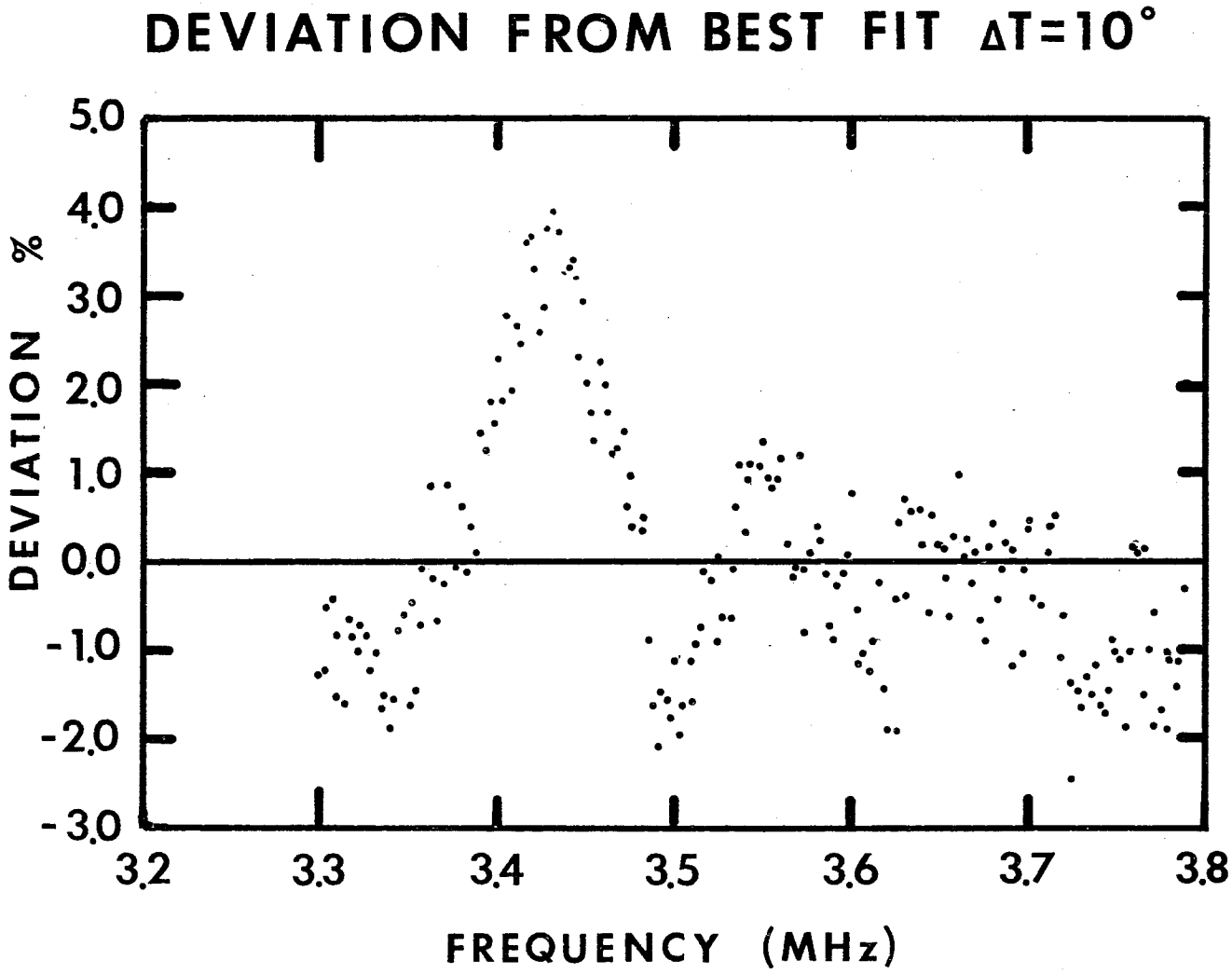
DEVIATION FROM BEST FIT ΔT=10°
DEVIATION %
5.0
4.0
3.0
2.0
1.0
0.0
-1.0
-2.0
-3.0
3.2
3.3
3.4
3.5
3.6
3.7
3.8
FREQUENCY (MHz)

Figure 4.8: Deviation plot for spectrum at $\Delta T = 0.05^{o}K$, $\Theta = 2.7^{o}$. Spectrum is shown in fig. 4.10. The zero per cent line is the best fit convolution integral, eqn. 4.21.

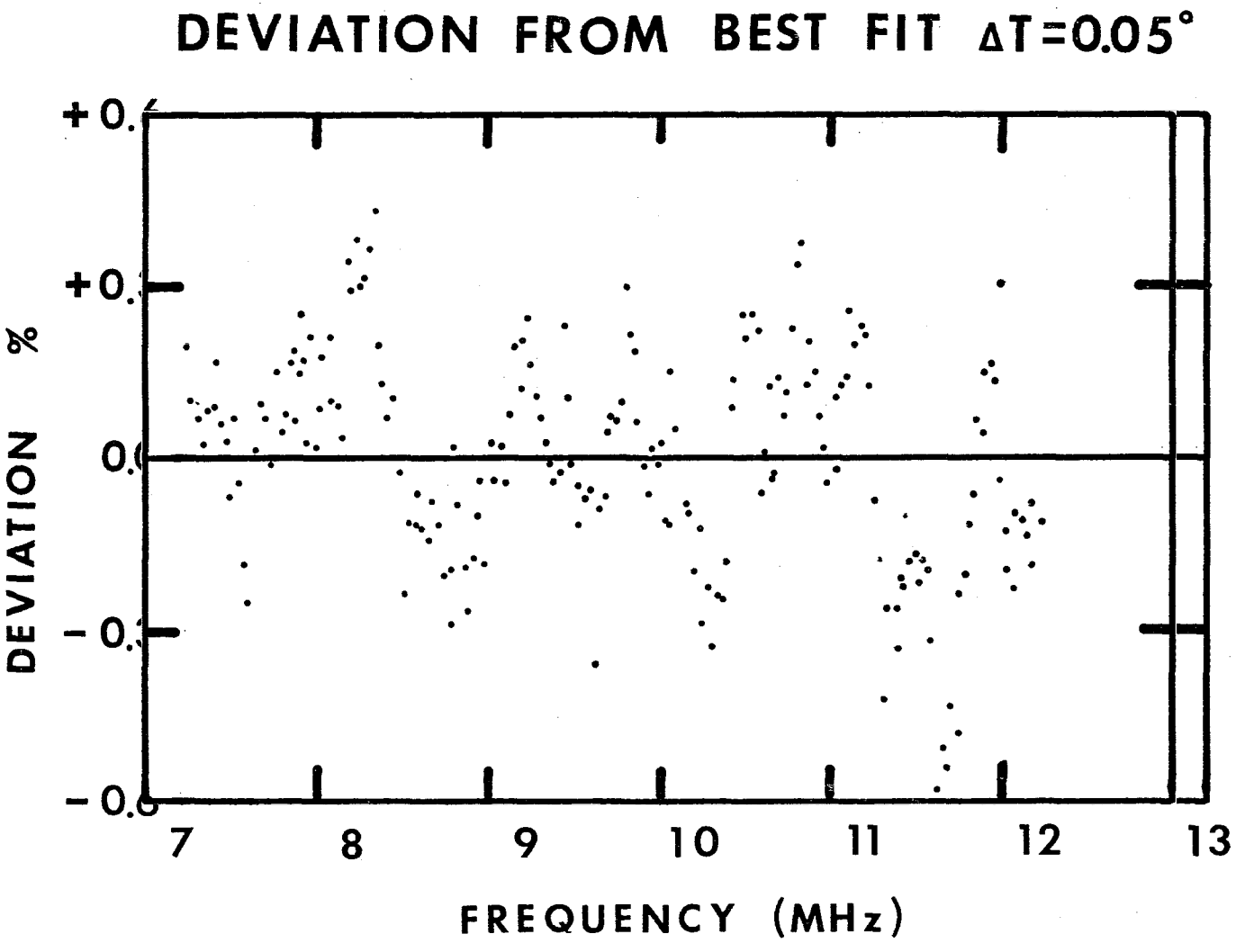
DEVIATION FROM BEST FIT ΔT=0.05°
+0.
+0.
0.
-0.
-0.
DEVIATION %
7
8
9
10
11
12
13
FREQUENCY (MHz)

Figure 4.9: Power spectrum at $\Delta T = 10^{o}K$, $\theta = 0.7^{o}$. Jagged line is measured spectrum, smooth curve is best fit to convolution integral, eqn. 4.21. ν_B is the best fit Brillouin shift. Γ_B is the best fit Brillouin linewidth. See figs. 4.5, 4.7.

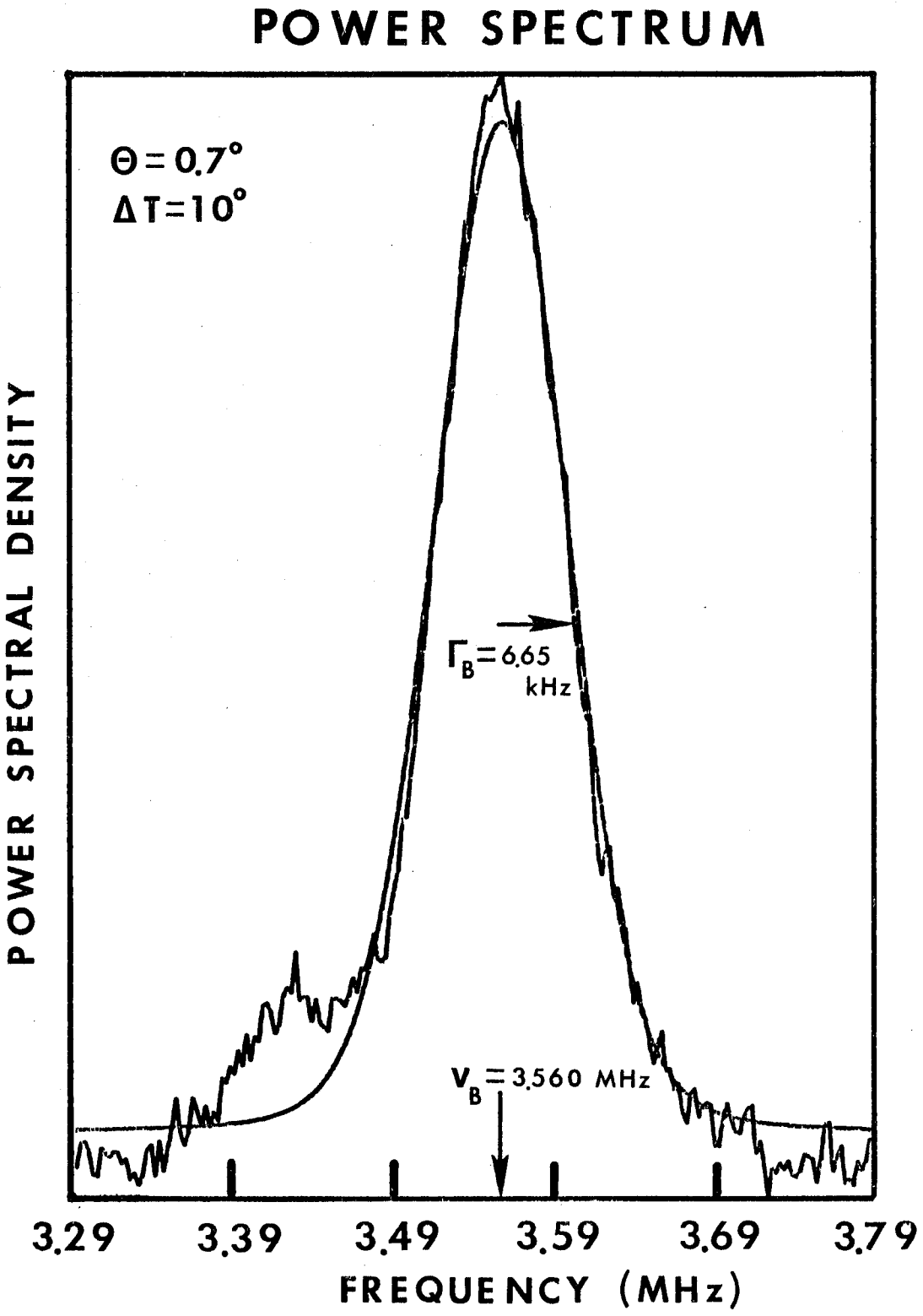
POWER SPECTRUM
Θ = 0.7°
ΔT = 10°
Γ_B = 6.65 kHz
V_B = 3.560 MHz
POWER SPECTRAL DENSITY
3.29
3.39
3.49
3.59
3.69
3.79
FREQUENCY (MHz)

Figure 4.10: Power spectrum at $\Delta T = 0.05^{o}K, \theta = 2.7^{o}$. Jagged line is measured spectrum, smooth curve is best fit to convolution integral, eqn. 4.21. ν_B is the best fit Brillouin shift. Γ_B is the best fit Brillouin linewidth. The complete data reduction procedure is given step by step by viewing figs. 4.2, 4.3, 4.6, 4.8, and this figure.

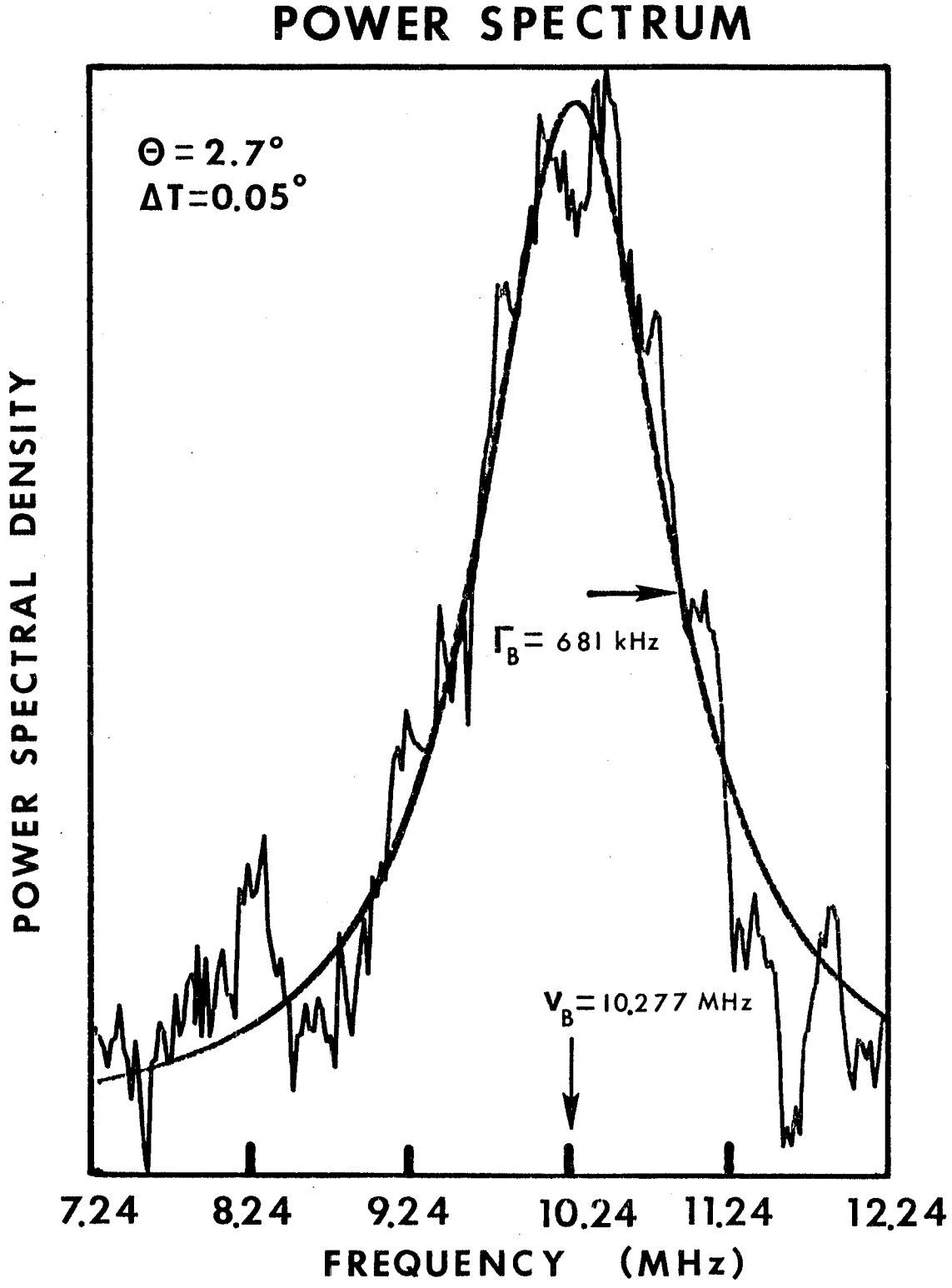
POWER SPECTRUM
Θ = 2.7°
ΔT=0.05°
Γ_B = 681 kHz
V_B = 10.277 MHz
POWER SPECTRAL DENSITY
7.24
8.24
9.24
10.24
11.24
12.24
FREQUENCY (MHz)

the respective best fits to the assumed functional form as smooth solid lines.

E Results

Appendix B lists in tabular form all the data obtained organized by scattering angle, then temperature. The best fit Brillouin frequency shift and Brillouin HWHM linewidth are given, along with the derived velocity and attenuation. The tables list the critical part of the attenuation and the background attenuation separately, the latter obtained from a calculation to be described in the following chapter. Note that in the theories of Kawasaki and Mistura, only the critical part of the attenuation is used, obtained by subtracting the background attenuation from the total attenuation. The sound velocity and total attenuation were obtained from the frequency and linewidth respectively, according to equations 4.22 and 4.23.

Figure 4.11 shows the spectrum taken at $\Delta T = 2^{o}$ at a scattering angle of 0.718^{o} (in air). The jagged line is the measured spectrum, the solid curve the best fit convolution integral. In figure 4.12 the various effects that contribute to the total observed spectrum of figure 4.11 are displayed. The lineshapes have been normalized to unit amplitude. For this example, note how the diffraction broadening is nearly as large as the Brillouin linewidth, and is the major instrumental effect.

Regarding instrumental effects, the electronic bandwidths were of course constant, the aperture broadening and

Figure 4.11: Power spectrum at $\Delta T = 2^{o}K$, $\Theta = 0.7^{o}$. Jagged line is measured spectrum, smooth curve is best fit to convolution integral, eqn. 4.21. ν_B, Γ_B, are the best fit Brillouin shift and Brillouin linewidth, respectively.

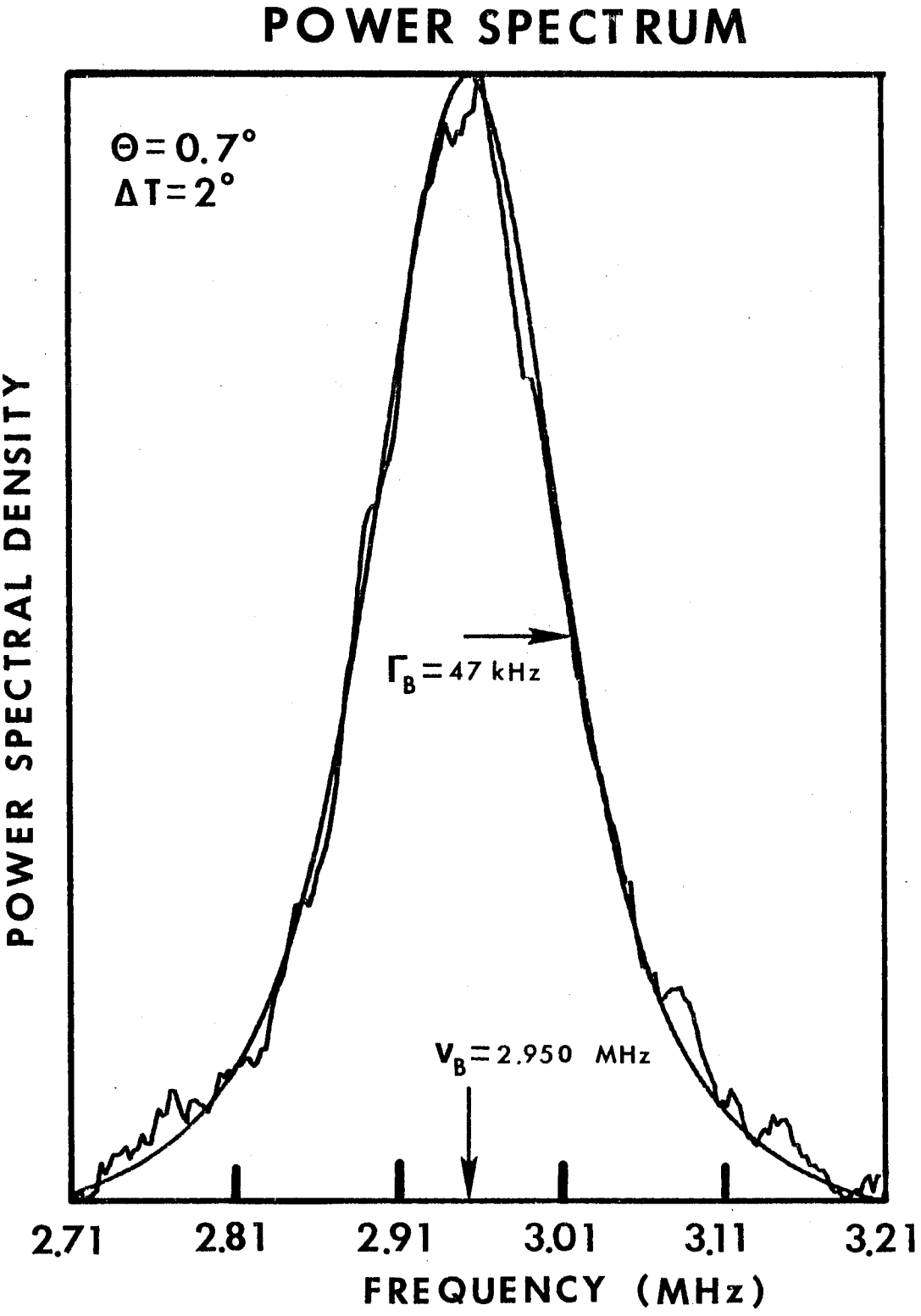
POWER SPECTRUM
Θ = 0.7°
ΔT = 2°
Γ_B = 47 kHz
V_B = 2.950 MHz
POWER SPECTRAL DENSITY
2.71
2.81
2.91
3.01
3.11
3.21
FREQUENCY (MHz)

Figure 4.12: Instrumental effects. The total observed spectrum is that of fig. 4.11. The composite effects are as follows.

Source	Lineshape	HWHM(kHz)
1 IF Filter	Voigt	$\Gamma_1(G)=4.44$
		$\Gamma_1(L)=1.00$
2 Diffraction	Gaussian	$\Gamma_2(G)=36.77$
3 Brillouin	Lorentzian	$\Gamma_3(L)=47.44$
4 Slit	Rectangular	$\Gamma_4 =7.06$
5 Total Observed	Convolution of 1,2,3,4	$\Gamma_5 =67.13$

Total Gaussian component $=(\Gamma_1^2(G) + \Gamma_2^2(G))^{\frac{1}{2}}$

$= 37.03$ kHz

Total Lorentzian component $=\Gamma_1(L) + \Gamma_3(L)$

$= 48.44$ kHz.

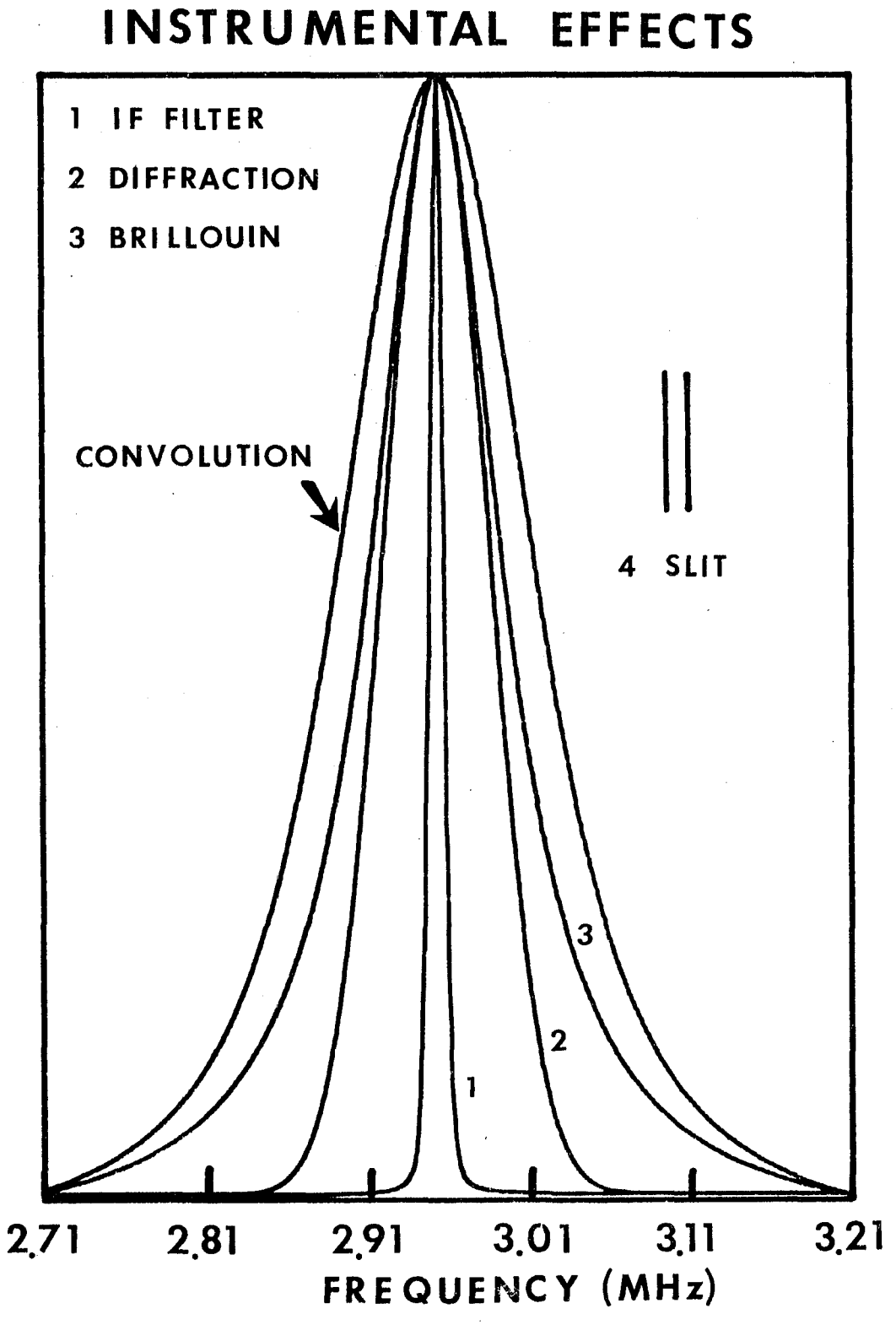
INSTRUMENTAL EFFECTS
1 IF FILTER
2 DIFFRACTION
3 BRILLOUIN
CONVOLUTION
4 SLIT
1
2
3
2.71
2.81
2.91
3.01
3.11
3.21
FREQUENCY (MHz)

diffraction broadening varied with angle and frequency shift. The range of variation of slit and diffraction broadening for each angle was as follows (HWHM):

0^{o} (air)	Slit (kHz) max	min	Diffraction (kHz) max	min
.36	6.9	4.4	35.8	23.2
.72	8.9	4.9	46.1	25.3
1.44	8.8	6.1	45.7	31.6
2.69	8.6	6.4	45.3	33.3

Figure 4.13 summarizes the experiment. The three spectra were taken at different temperatures, but at the same scattering angle and same slit width. The spectra have been normalized to the background constant (taken to be unity) of the spectrum at $\Delta T = 10^{o}$. Since the background constant is the shot noise, the spectra were adjusted for differences in initial laser intensity and averaging time. There are four things to note from the figure. As ΔT decreases, the Brillouin line shift decreases. As ΔT decreases, the total linewidth space increases, reflecting the increase in attenuation. The shot noise level increases sharply as $\Delta T \rightarrow 0$, because the Rayleigh line intensity, acting as local oscillator, increases due to the divergence of the compressibility. At $\Delta T = 2^{o}$, the shot noise level is 21 times greater than at $\Delta T = 10^{o}$, and at $\Delta T = .05^{o}$, is 32 times greater. The Brillouin intensity increases at $\Delta T \rightarrow 0$; note the $\Delta T = 10^{o}$ spectrum has been expanded vertically by a factor of five. However, the increase is slight compared to the Rayleigh

Figure 4.13: Summary of Brillouin scattering experiment. The spectra are the total observed spectra including all instrumental effects, but normalized to the shot noise level of the spectrum at $\Delta T = 10^0 K$. Note that the vertical scale of the spectrum at $\Delta T = 10^oK$ has been expanded by a factor of 5. See text for description.

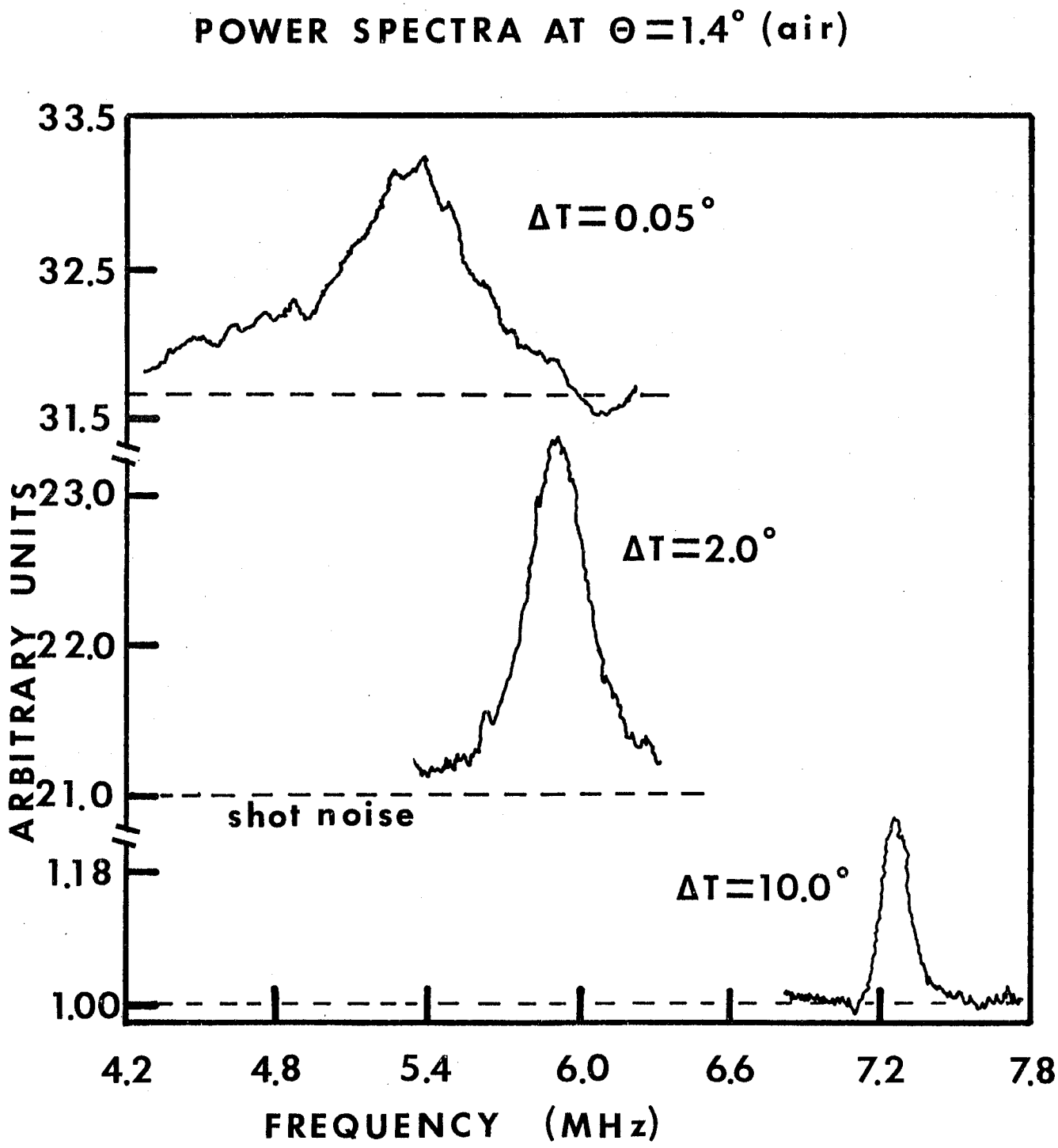
POWER SPECTRA AT Θ=1.4° (air)
33.5
32.5
31.5
23.0
22.0
21.0
1.18
1.00
ARBITRARY UNITS
ΔT=0.05°
ΔT=2.0°
ΔT=10.0°
shot noise
4.2
4.8
5.4
6.0
6.6
7.2
7.8
FREQUENCY (MHz)

intensity change, and this is reflected in the peak Brillouin intensity to shot noise level. For $\Delta T = 10^{o}$, this ratio is 0.24, for $\Delta T = 2^{o}$, 0.11, and for $\Delta T = .05^{o}$ it is 0.05. There is greater difficulty in obtaining spectra as $\Delta T \rightarrow 0$ because of the smallness of this ratio. The Brillouin peak is harder to discern because it is spread out in frequency space, and the fluctuations in the background easily overcome the weak Brillouin line so that averaging times must be longer.

References for Chapter IV

1. H.Z.Cummins and H.L.Swinney, in Progress in Optics Vol.VIII (North Holland,Amsterdam,1970), p.188.

2. E.Magrab and D.Blomquist, Measurement of Time Varying Phenomena, p.69 (Wiley,New York,1971).

3. P.R.Bevington, Data Reduction and Error Analysis for the Physical Sciences, p.251 (McGraw-Hill,New York,1969).

4. R.Hamming, Introduction to Applied Numerical Methods, p.153 (McGraw-Hill,New York,1971).

5. Ref. 4,p.147.

6. Ref. 4,p.149.

7. IBM Scientific Subroutine Package Program MINV: matrix inversion.

8. Ref. 2,p.52-53.

9. Ref. 3,p.204-207.

10. J.Kielkopf, J.Opt. Soc. Am. 63, 987 (1973).

11. Ref. 3,p.45.

12. Ref. 3,p.182.

13. M.J.D.Powell, Comp. J. 7,155 (1964).

14. M.J. Box, D. Davies and W. Swann, Nonlinear Optimization Techniques (Oliver & Boyd Ltd., Edinburgh, 1969).

15. Ref. 3,sec. 11-2.

16. S.Jacoby, J.Kowalik and J.Pizzo, Iterative Methods for Nonlinear Optimization Problems (Prentice Hall,Englewood Cliffs, 1972).

17. Ref. 3,p.245.

18. P. Jacquinot, Rep. Prog. Physics 23, 275 (1960).

19. Y. Yeh, Appl. Opt. 8, 1254 (1969).

20. B. Chu, Laser Light Scattering, p.155 (Academic Press, New York, 1974).

21. H.Swinney, in Photon Correlation and Light Beating Spectroscopy, ed. by H.Z.Cummins and E.R.Pike (Plenum, New York,1974), p.331.

22. H.Weichel, Electro Optics System Design 8, 22 (1976).

23. O. Svelto, Principles of Lasers, p.264 (Plenum, New York, 1976).

24. P.Ritger and N.Rose, Differential Equations with Applications, p.287 (McGraw-Hill, New York,1968).

25. J.Mathews and R.Walker, Mathematical Methods of Physics 2nd Ed.,p.113 (Benjamin, New York,1970).

26. B.H.Armstrong, J.Quant. Spect. Rad. Trans. 7,61 (1967).

27. B.Roos, Analytic Functions and Distributions in Physics and Engineering, p.302 (Wiley, New York,1969).

28. V.I.Krylov, Approximate Calculation of Integrals, p.129 (MacMillan, New York,1962).

29. A.Ralston, A First Course in Numerical Analysis, p.118 (McGraw-Hill,New York,1965).

30. L.Mandel, E.Sudarshan and E.Wolf, Proc. Phys.Soc. (London) 84, 435 (1964).

31. M. Bertolotti, in Ref. 21, p.46.

32. W.T.Eadie, D.Dryard, F.James, M.Roos, B.Sadoulet, Statistical Methods in Experimental Physics, p.40 (North Holland, Amsterdam, 1971).

33. B.Crosignani, P.Di Porto, M.Bertollotti, Statistical Properties of Scattered Light, p.151-154 (Academic Press,New York, 1975).

34. Ref. 31,p.48.

35. D.Henry, Ph. D. Thesis, Johns Hopkins Univ.,1970 (unpublished).

36. Ref. 31,p.50.

37. RCA Photomultiplier Tube Manual, p.65 (RCA, Lancaster, PA.,1970).

38. The concepts in this section are reviewed by M.J.D. Powell, in Numerical Analysis, ed. by J.Walsh (Thompson Book Co., Washington , D.C., 1966) p. 143.

39. D. Marquardt, J. Soc. Ind. Appl. Math. 11, 431 (1963).

40. Ref. 16, p.242.

41. Ref. 3, p.208-211.

CHAPTER V

COMPARISON OF RESULTS WITH THEORY

A Systematic Error

After all spectra were collected, a systematic error was found. The output lens of the spatial filter was slightly mispositioned causing the emerging beam to be focussed rather than collimated. Since the annular aperture was positioned at the focal point of the collection lens assuming collimated light at the input to this lens, the focussing caused the aperture to be positioned at a point less than the true focal length. From the spectra at all angles at $\Delta T = 10^{\circ}K$, the velocity was determined and compared to the ultrasonic velocity of Mueller et al[1] at the same temperature. This far from T_c there is no measurable dispersion, and the Brillouin and ultrasonic measurements should all give the same velocity. From the difference in velocities, a new effective focal length was determined, and the four scattering angles were corrected. Appendix A tabulates the corrected scattering angles.

B Background Attenuation

The classical, or background attenuation must be subtracted from the total measured attenuation before comparison with critical fluid theories.[2] It is:

$$\alpha_{\lambda}^{B} = \frac{\pi\omega}{V_o^2}\left[\frac{(4/3)\eta + \zeta^{B}}{\rho} + \frac{\lambda}{\rho}\left(1/c_v - 1/c_p\right)\right]$$

where $\omega = 2\pi\nu_B$

$V_o = v(\omega=0)$ = zero frequency sound velocity

η = shear viscosity

ζ^B = bulk viscosity (background)

ρ = density

λ = total thermal conductivity

C_p, C_v = constant pressure, volume specific heats

The terms in brackets are all temperature dependent; thus, $\alpha_\lambda^B = \alpha_\lambda^B(T, \theta)$. The temperature dependent terms have been tabulated by Swinney and Henry[3] for xenon at the critical density. For a derivation of the explicit terms used to calculate the thermodynamic quantities, refer to Appendix C. Note that the conductivity is the total conductivity, the sum of the critical and background parts: $\lambda^{total} = \lambda^c + \lambda^B$. One should look at the original calculations of Kawasaki and note that the viscosity was to be determined by measurement, so that λ must be the total conductivity. For a discussion of this point, see Swinney.[4]

The value of the zero frequency sound velocity used in the calculation of α_λ^B was determined through quadratic interpolation of the reported values of Garland & Williams[5] for $\Delta T \leq 2^oK$. In their analysis, Garland & Williams mention that their 1 kHz data agree with the 1 MHz results obtained earlier by Mueller, et al[1] at $\Delta T = 4.78^oK$. Therefore, the tabulated velocities measured at 1 MHz by Mueller

were used for interpolation for $\Delta T \geq 2^{o}K$ (note: there is no detectable dispersion in the 1 MHz velocities compared to the 0.55 MHz data of the same table for $2^{o} \leq \Delta T \leq 10^{o}K$). The temperature values of the present experiment were $\Delta T = 10^{o}$, 5^{o}, 2^{o}, 1^{o}, 0.5^{o}, 0.2^{o}, 0.1^{o}, $0.05^{o}K$, and the values of v_0 obtained by interpolation are presented in Appendix D. The tables of data in Appendix B list both the critical and background parts of the total measured attenuation.

C Velocity & Attenuation Results

All sound velocity data are plotted as a function of ΔT in figure 5.1. For $\Delta T = 10^{o}$ and $5^{o}K$, little or no dispersion is evident, the data at all angles are clustered about the zero frequency sound velocity. The average of all the data at $\Delta T = 10^{o}$ indicates a standard deviation of $\pm$ 1.2% in the velocity (ratio of error in mean to mean).

For the range of angles studied, some dispersion is expected starting at $\Delta T = 2^{o}K$.[6] For this experiment, the dispersion at $\Delta T = 2^{o}K$ cannot be distinguished from the experimental error, the averaged dispersions at all angles being less than $\pm$ 1.0%.

All data for the lowest scattering angle are erratic, showing the greatest scatter, and do not follow the expected trend of less dispersion for lower Brillouin frequencies. Since the error in angular alignment is approaching the scattering angle itself at this angle ($\sim 0.36^{o}$) these data are not expected to be reliable.

Figure 5.1: Sound velocity - all data.

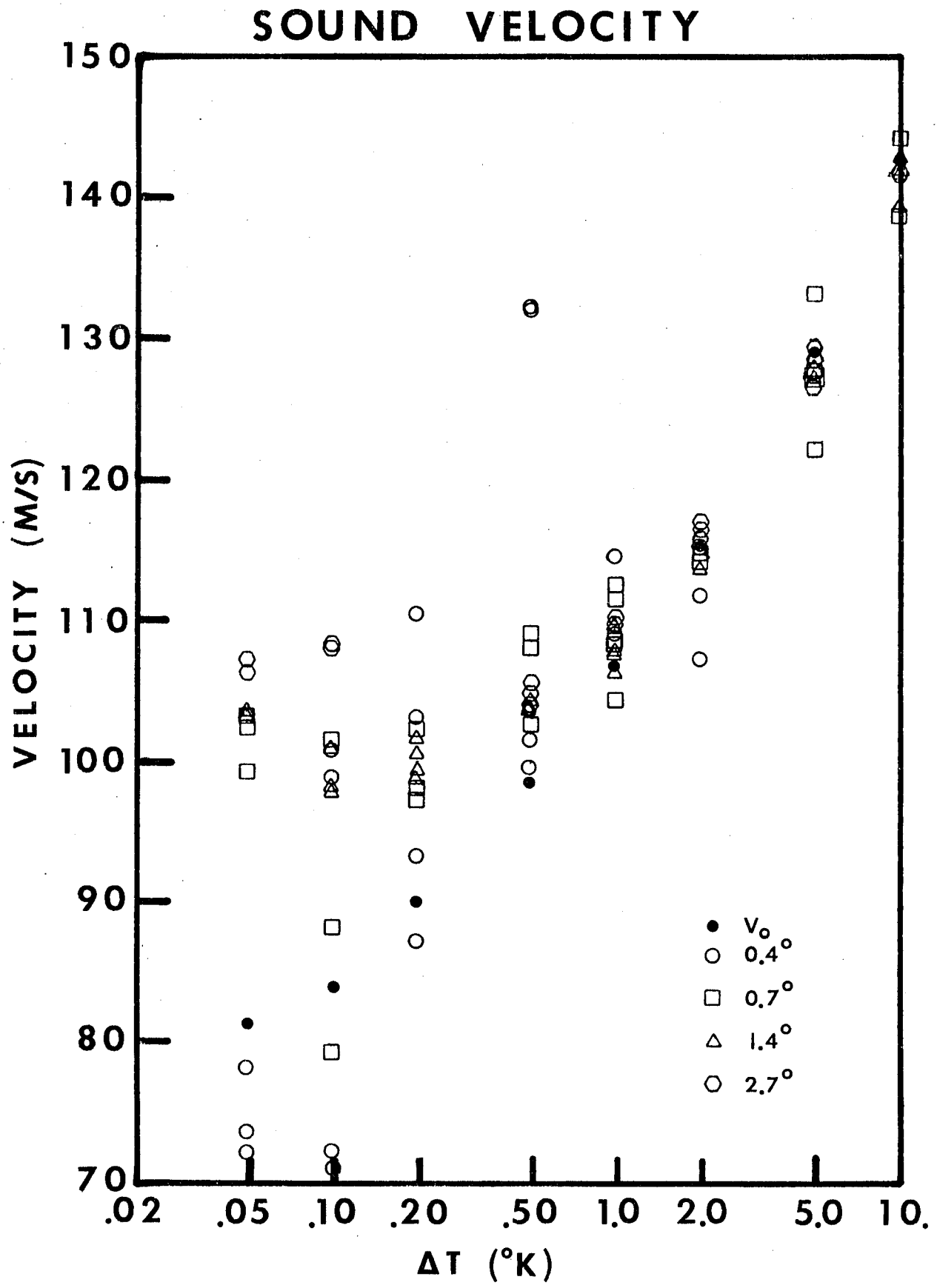
SOUND VELOCITY
VELOCITY (M/S)
150
140
130
120
110
100
90
80
70
.02
.05
.10
.20
.50
1.0
2.0
5.0
10.
ΔT (°K)
V_o
0.4°
0.7°
1.4°
2.7°

For the largest scattering angles, dispersion is clearly seen for all $\Delta T \leq 1^{o}$, the velocities lying above the + 1.2% error. The averaged percentage dispersions for these angles are:

Table 5.1: Average Dispersion

θ =	2.7^{o}	1.4^{o}	0.7^{o}
$\Delta T = 1^{o}$	2.49	1.31	2.36
0.5^{o}	5.55	5.21	7.75
0.2^{o}		11.09	10.00
0.1^{o}	28.76	17.84	20.88
0.05^{o}	31.12	27.09	24.90

All attenuation data are plotted as a function of ΔT in figure 5.2. The smallest angle data, while showing the trend of increased attenuation as $\Delta T \rightarrow 0$, are again not expected to be accurate. For $\Delta T \leq 0.5^{o}$ at this angle, the attenuations exceed those at the larger angles for the same temperatures. For this reason, they should be neglected.

The averaged attenuations at the other angles show the expected trends of increased attenuation as $\Delta T \rightarrow 0$, and increased attenuation at higher Brillouin frequencies, within rather large experimental errors. The percentage errors in the angle-averaged attenuations reflect the difficulties in deconvolving instrumental effects. At the lowest temperature $\Delta T = 0.05^{o}$, the standard deviation was actually smallest ($\sim$6%). Here, the Brillouin widths are largest. The largest errors were at $\Delta T = 0.1^{o}$, $\sim$ 70%, then decreased to $\sim$10% near $\Delta T = 2^{o}$. Beyond $\Delta T = 2^{o}$, the standard deviation increased to $\sim$ 26% at

Figure 5.2: Sound attenuation - all data.

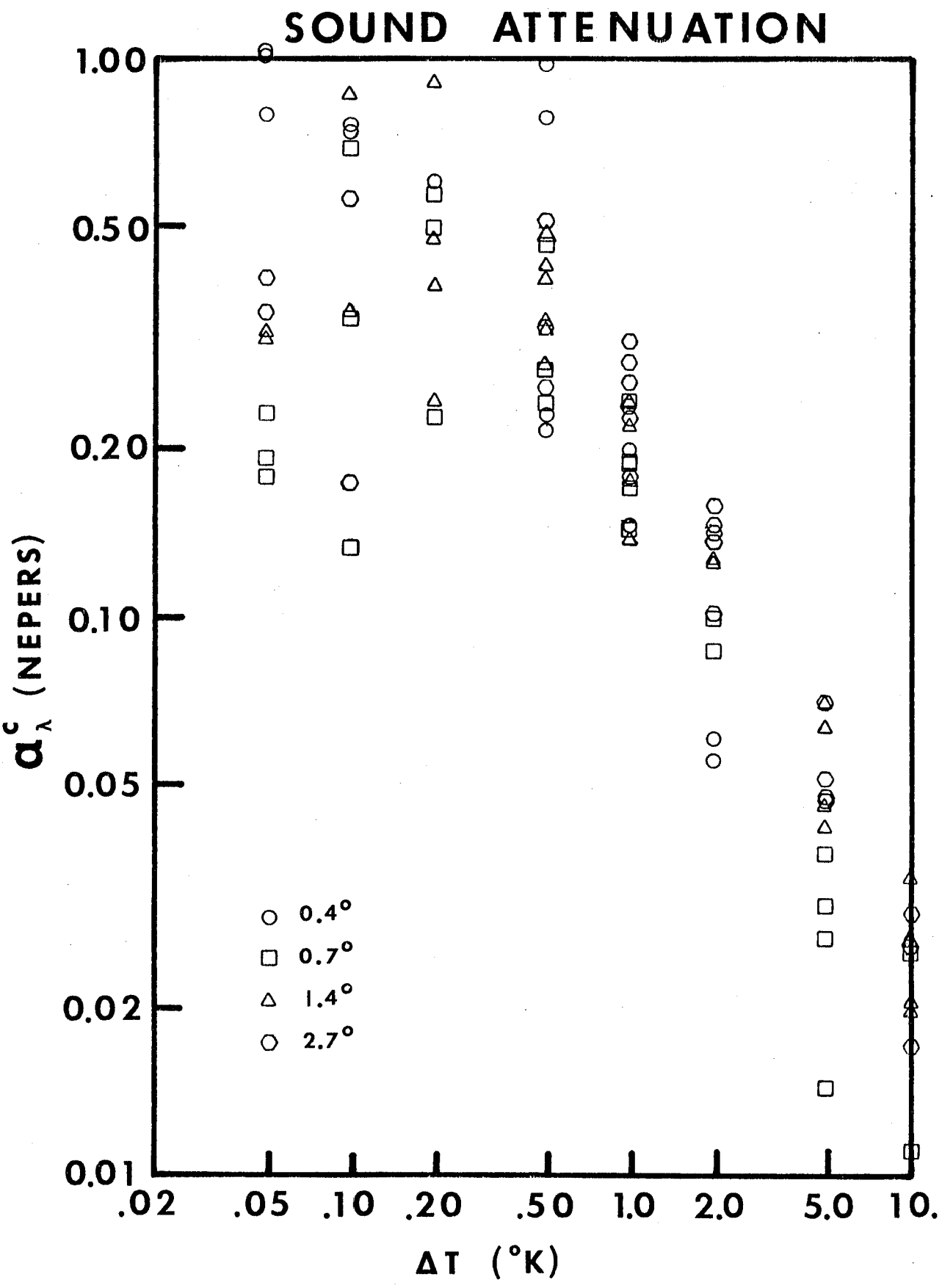
SOUND ATTENUATION
1.00
0.50
0.20
0.10
0.05
0.02
0.01
α_λ^c (NEPERS)
.02
.05
.10
.20
.50
1.0
2.0
5.0
10.
ΔT (°K)
0.4°
0.7°
1.4°
2.7°

$\Delta T = 10^{o}K$. Here, the widths are at the limits of experimental detection, exceedingly narrow.

D Reduced Dispersion, Reduced Attenuation

A comparison of the experimental results with critical liquid theories is facilitated by defining a reduced dispersion, D, and reduced attenuation, A, as follows:[7]

$$D \equiv (v(\omega) - v_o)/(v_o F(T)) \qquad 5.1$$

$$A \equiv \alpha_\lambda^c(\omega)/(2\pi F(T)) \qquad 5.2$$

$$F(T) = \frac{k_B T^2}{2\pi^2 \rho C_V \xi}\left(1 - \frac{C_V}{C_P}\right)\left(\frac{\partial \xi^{-1}}{\partial T}\right)_S^2 \qquad 5.3$$

Then, D and A are related to the integrals J and I as follows:

$$D = J(\omega^*, \lambda^B/\lambda) \qquad 5.4$$

$$A = I(\omega^*, \lambda^B/\lambda) \qquad 5.5$$

where ω^* is the reduced frequency:

$$\omega^* = \omega/(2\omega_R) \qquad \omega_R = \lambda/(\rho C_P \xi^2) \qquad 5.6$$

The factor F(T) contains all the weakly temperature dependent quantities needed for direct comparison to theory, and if these are all known, then an analysis may be carried out with no adjustment of parameters. A compilation of these thermodynamic parameters for xenon on the critical isochore is again found in the tables of Swinney & Henry,[3] all of which were used previously in determining α_λ^B. Refer to Appendix C for the quantities needed to compute F(T) and ω^*.

The Kawasaki-Mistura integrals may be written as follows, assuming the Ornstein-Zernike form for the correlation function:[7]

$$J(\omega^*, \lambda^B/\lambda) = \int_0^\infty \frac{x^2\, dx}{(1+x^2)^2\left(1+(2T_R'/\omega)^2\right)}$$

$$I(\omega^*, \lambda^B/\lambda) = \int_0^\infty \frac{(2T_R'/\omega)\, x^2\, dx}{(1+x^2)^2\left(1+(2T_R'/\omega)^2\right)}$$

$$2T_R'/\omega = \left[K_0(x) + (\lambda^B/\lambda)\left[x^2(1+x^2) - K_0(x)\right]\right]\frac{1}{\omega^*}$$

$$K_0(x) = .75\left(1 + x^2 + (x^3 - 1/x)\,\mathrm{TAN}^{-1}x\right)$$

These include the dependence on the background thermal conductivity, λ^B, which is non-negligible over the temperature range of measurements (most analyses have taken $\lambda^B = 0$ for comparison of theory and experiment), and once again, the discussion of Swinney[2] on this point should be noted.

If $\lambda^B = 0$, then these integrals may be written in a form which displays the correlation function dependence:[8]

$$J(\omega^*) = \int_0^\infty \frac{x^2 g^2(x)\, \omega^{*2}\, dx}{K_0^2(x) + \omega^{*2}} \qquad 5.7$$

$$I(\omega^*) = \int_0^\infty \frac{x^2 g^2(x)\, \omega^* K_0(x)\, dx}{K_0^2(x) + \omega^{*2}} \qquad 5.8$$

where g(x) is the (dimensionless) form for the correlation function. The tabulation of Tartaglia and Thoen[8] for g(x) is as follows:

$\frac{1}{1+x^2}$	Ornstein-Zernike OZ
$\frac{\frac{1}{2}(1-\eta)\quad(1+x\cot((1-\eta)\tan^{-1}x))}{1+x^2}$	exact Fourier Transform FT
$1 - \frac{\frac{1}{2}\eta}{1+(\phi x)^2} - \frac{(1+\frac{1}{2}\eta\phi^2)x^2}{1+(1+\frac{1}{2}\eta\phi^2)x^2}$	Fisher-Burford FB

$$\frac{p D_1 X^{-P} + (D_2/\nu) X^{-1/\nu}}{2(1 - D_1 X^{-P} - D_2 X^{-1/\nu})} \qquad \text{Fisher-Langer}$$

$$p = (1-\alpha)/\nu \qquad \text{FL}$$

The dimensionless parameter x is equal to $q\xi$ in all forms. The second form is the exact Fourier transform of the asymptotic limit of the net correlation function $G(r) = g(r) - 1$ which includes the Fisher[9] correction:

$$G(r) = \text{constant} \quad \exp(-r/\xi)/r^{1+\eta}$$

The correction, η, in the exact as well as the FB form is expected to be 0.056.[10] ϕ is expected to be 0.15.[10] The FL form involves many adjustable parameters.[11] In the analysis that follows, the FL form will not be compared to the data of the present experiment. From the work of Tartaglia and Thoen[8], it is seen that the FL form, as a function of ω^*, will lie between the FT and OZ cases, depending on the parameter p. Therefore, only the OZ, FT, and FB forms will be treated.

For the calculation of these integrals, the transformation, $x = \tan\theta/4$, was used. Then the integrals become periodic functions over the range $[0, 2\pi]$ as follows:

$$J(\omega^*) = \int_0^{2\pi} \frac{(1/4)\,TAN^2\theta/4\;SEC^2\theta/4\;g^2(\theta)\,d\theta}{1 + (K_0(\theta)/\omega^*)^2}$$

$$I(\omega^*) = \int_0^{2\pi} \frac{(1/4)\,TAN^2\theta/4\;SEC^2\theta/4\;(K_0(\theta)/\omega^*)\,g^2(\theta)\,d\theta}{1 + (K_0(\theta)/\omega^*)^2}$$

These are easily integrated numerically by the following quadrature formula:[12]

$$\int_0^{2\pi} t(y)\,dy \approx \frac{2\pi}{N} \sum_{k=1}^{N} t\left(a + (k-1)\frac{2\pi}{N}\right)$$

$k = 0, 1, 2, \cdots N-1$ $\qquad$ a = constant offset from origin

The coefficients of the quadrature sum are all constant and simply $2\pi/N$. The nodes are $a + (k-1)2\pi/N$. Assuming greater accuracy for larger N, a 100 point summation of the J and I integrals differed from a 1000 point summation by 1 PPM.

Figure 5.3 displays the reduced dispersion, D, as a function of ω^* for the averaged data of the present experiment. The curves are $J(\omega^*)$ with $\lambda^\beta = 0$ for the FT, OZ, and FB forms for g(x). Ideally, D should be non-negative since the velocity cannot be less than the zero frequency sound velocity. Experimental error is reflected in the scatter of the data, particularly at the lowest scattering angle, and in the negative dispersion. If the data at the lowest angle are ignored, the remaining data indicate a departure from $J(\omega^*)$ to higher values for all ω^* greater than about 10, and for all $g(x)$. In particular, at $\omega^* \sim 900$, D is about 3 times greater than J (for FT), and at ω^* 100, D is about 2 times greater.

For the reduced attenuation, A, averaged data are plotted in figure 5.4 as a function of ω^*. The curves are $I(\omega^*)$ for FT, OZ, and FB, with $\lambda^\beta = 0$. All values of A are larger than I for all g(x), and over the entire range of ω^*, with marked departure starting at $\omega^* \sim 2$. The largest departure is near $\omega^* = 100$, with the measured attenuation A as much as a factor of ten greater than the closest theoretical values (for FT). For $\omega^* > 100$, A decreases again: at $\omega^* = 900$, A is only a factor of five larger than the theoretical attenuation (for FT).

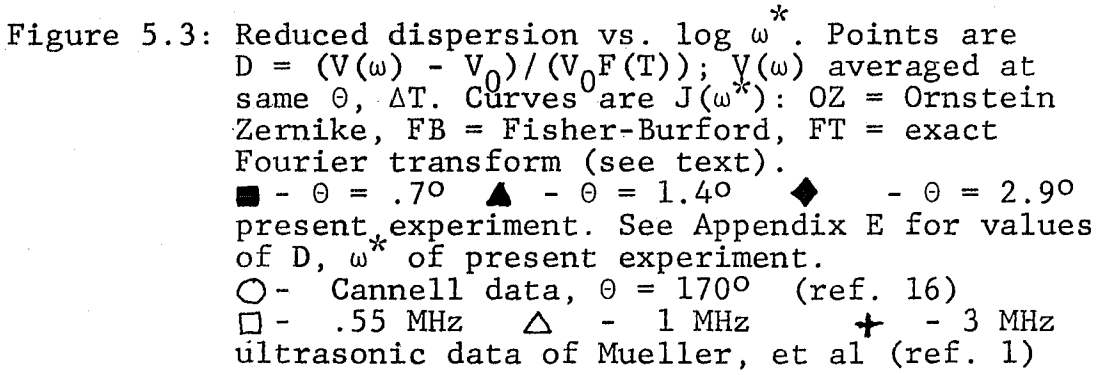

Figure 5.3: Reduced dispersion vs. log ω^*. Points are $D = (V(\omega) - V_0)/(V_0 F(T))$; $V(\omega)$ averaged at same θ, ΔT. Curves are $J(\omega^*)$: OZ = Ornstein Zernike, FB = Fisher-Burford, FT = exact Fourier transform (see text).
■ - $\theta = .7^o$ ▲ - $\theta = 1.4^o$ ◆ - $\theta = 2.9^o$ present experiment. See Appendix E for values of D, ω^* of present experiment.
○ - Cannell data, $\theta = 170^o$ (ref. 16)
□ - .55 MHz △ - 1 MHz + - 3 MHz ultrasonic data of Mueller, et al (ref. 1)

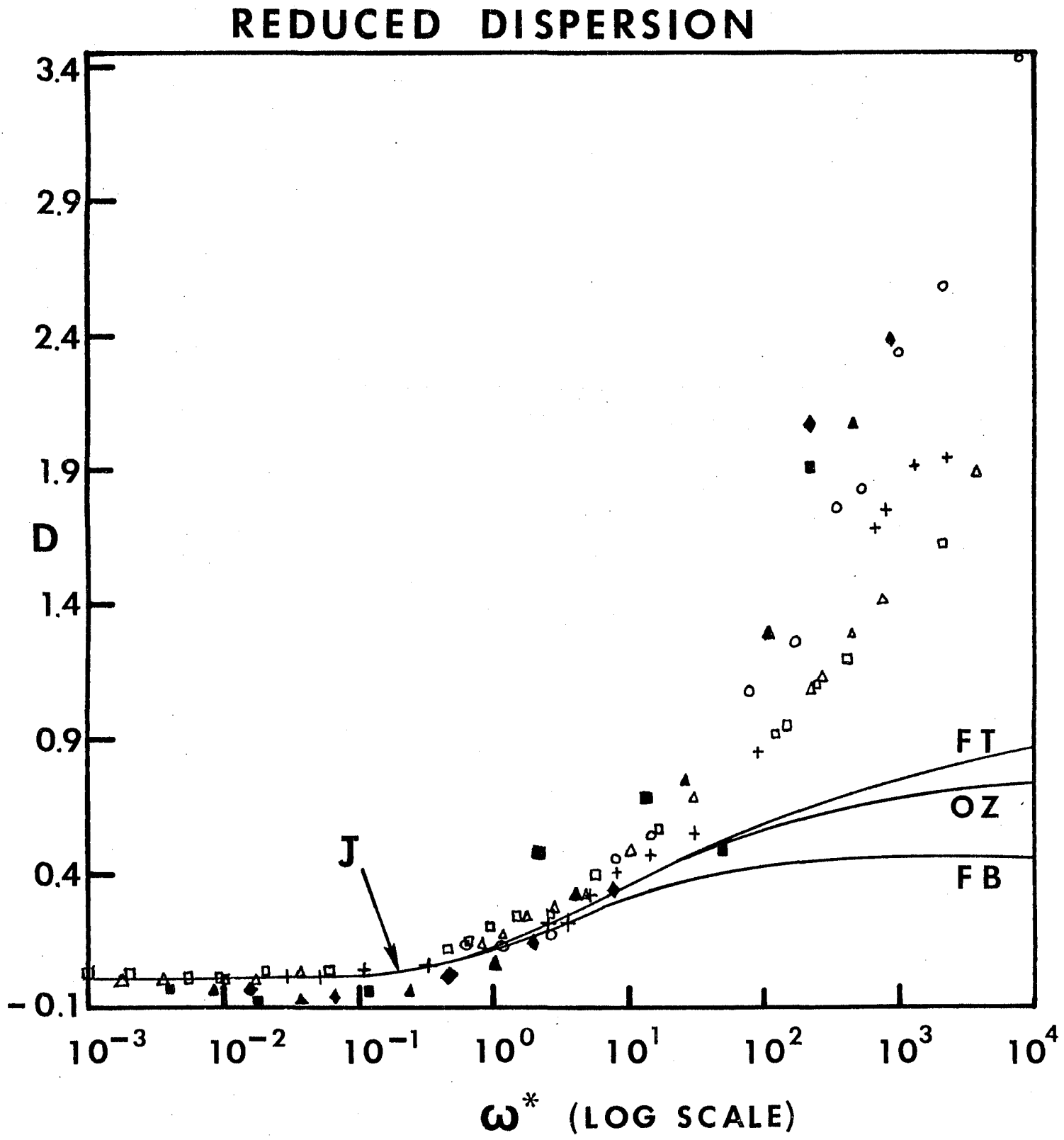
REDUCED DISPERSION
3.4
2.9
2.4
1.9
D
1.4
0.9
0.4
-0.1
FT
OZ
FB
J
10^{-3}
10^{-2}
10^{-1}
10^{0}
10^{1}
10^{2}
10^{3}
10^{4}
ω^* (LOG SCALE)

Figure 5.4: Reduced attenuation vs. log ω^*. Points are $A = \alpha_\lambda^c/(2\pi F(T))$; α_λ^c averaged at same Θ, ΔT. Curves are $I(\omega^*)$. Symbols same as fig. 5.3. See Appendix E for values of A, ω^* of present experiment.

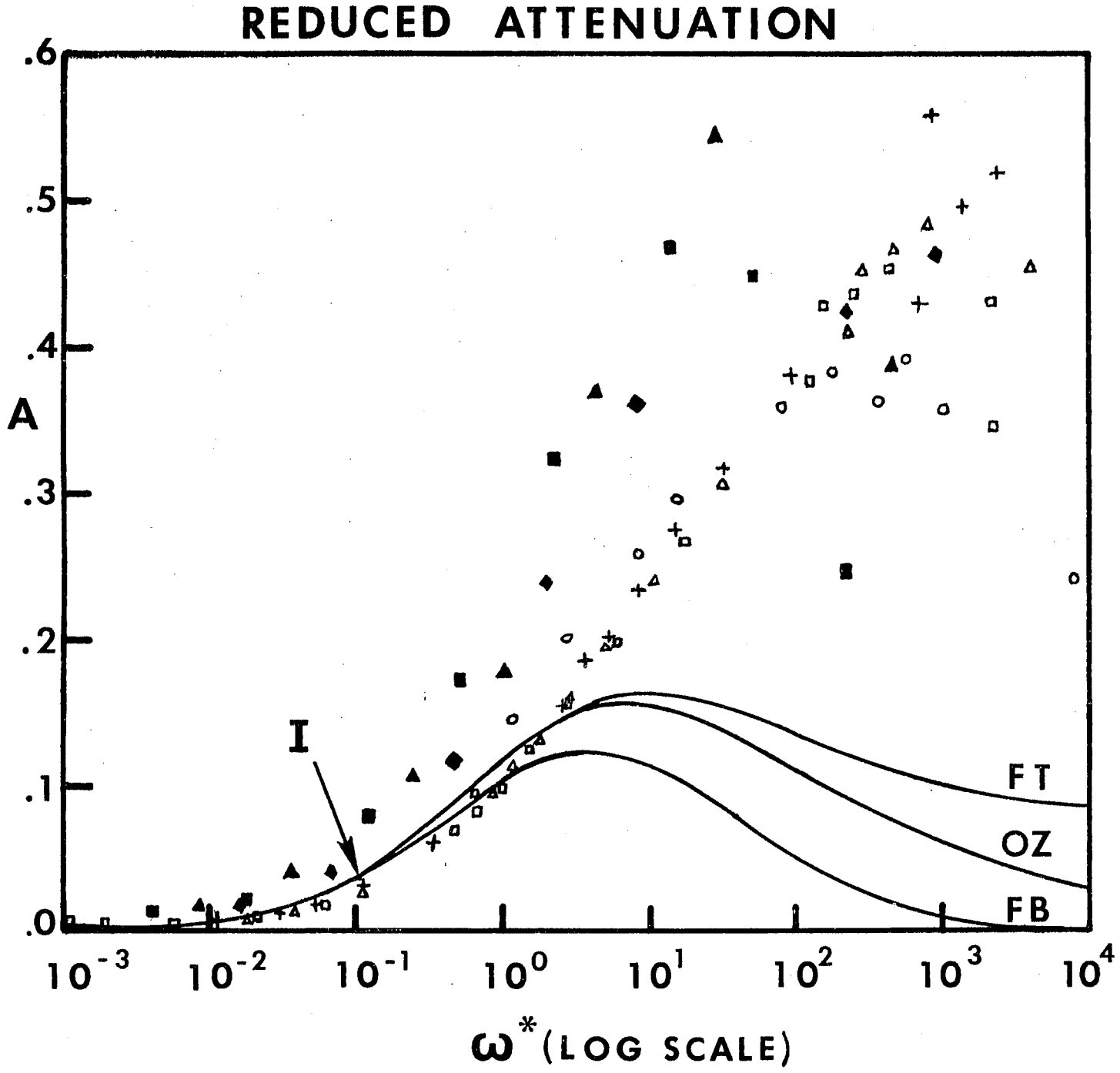
REDUCED ATTENUATION
.6
.5
.4
.3
.2
.1
.0
A
I
FT
OZ
FB
10^{-3}
10^{-2}
10^{-1}
10^{0}
10^{1}
10^{2}
10^{3}
10^{4}
ω^* (LOG SCALE)

These results should be compared with the analysis of Tartaglia & Thoen[8]. Using previously reported results[13,14,15] representing almost all the ultrasonic data to date, and including the Brillouin data of Cannell[16], a comparison was made with the integrals I and J. The following points should be noted. Tartaglia-Thoen's analysis of the data is similar to Thoen-Garland's[15]. One difference is in the calculation of J and I for different g(x). Since the present work used the g(x) and associated parameters based on Tartaglia-Thoen, no difference in results can be attributed to the calculation of J and I. Regarding the data, is should be noted that the density was measured concurrently with the velocity and attenuation along the coexistence curve for the ultrasonic experiments. The linear model equation of state[17] was used to calculate v_0 and C_v with the parameters in the model derived from a least squares fit of the 1 kHz and MHz results. Thus ω_R (in ω^*) was calculated for different thermodynamic paths, the coexistence curve and critical isochore, with parameters obtained by least squares fitting to a power law dependence over the different paths. Additionally, a quantity a(T) (= $F(T)/v_0^2$) was assumed to be given by $a(T) = \alpha \epsilon^{\beta}$ and the parameters α and β were obtained from a least squares fit of the attenuation and velocity data to the equation:

$$\alpha_\lambda^c / V^2(\omega) = 2\pi a(T) I(\omega^*)$$

and then a(T) used in the comparison of dispersion results with $J(\omega^*)$. All fits were carried out on data for $10^{-2} \leq \omega^* \leq 10$, so that it is not surprising that there is good agreement between theory and experiment in this region. Since

obtaining a(T) in this manner is equivalent to accepting the validity of $I(\omega^*)$, this analysis was not an absolute comparison of data and theory as is the present work, where no parameters were adjusted.

These comments noted, Tartaglia-Thoen found agreement between the reduced dispersion and J up to $\omega^* \sim 200$. Departure for $\omega^* > 200$ occurred, but the data do not predominately follow either g(x) tested, FL or OZ. For the reduced attenuation, there is agreement up to $\omega^* \sim 10$. For $\omega^* > 50$, the data are systematically greater than I for FL or OZ. Since the FL form produces larger values of I, it agrees with the data slightly better.

Regarding the only other heterodyne experiment performed, Eden & Swinney[18] examined the vapor phase of the coexistence curve below T_c over a narrow range: $.01 \leq \omega^* \leq 2.0$. The dispersion results agree well with J (for OZ), and again some negative dispersion is indicative of the experimental error involved in measurements at small scattering angles. For the attenuation, A agrees with I (for OZ) up to $\omega^* \sim 2$, thereafter, A becomes less dropping to 77% of I at $\omega^* = 2.0$. However, it should be noted that this is also an absolute comparison with theory with no parameter adjustment, but F(T) for the coexistence curve is not well known. The linear model equation of state was used to determine v_o and the compressibility. The correlation length was determined from $\xi^2 = \rho k_B \, TR^2 K_T$, and in view of the large uncertainties involved in these expressions, the fit is quite good.

E Ratio Test of Critical Theories

Sarid & Cannell attempted to discriminate between the Kawasaki and Mistura formulations using the following approach. In Kawasaki's formulation, the real and imaginary parts of the critical complex viscosity, $b_c(\omega) = (4/3\ \eta(\omega) + \zeta(\omega))/\rho$, are related to $I(\omega^*)$ and $J(\omega^*)$ as follows:[19]

$$\omega\, Re[b_c(\omega)] = D(T)\, I(\omega^*) \qquad 5.9$$

$$\omega\, Im[b_c(\omega)] = D(T)\, J(\omega^*) \qquad 5.10$$

$$D(T) = 2 V_0^2 F(T) \qquad 5.11$$

If the ratio,

$$\frac{Im[b_c(\omega)]}{Re[b_c(\omega)]} = \frac{J(\omega^*)}{I(\omega^*)} \qquad 5.12$$

is formed, then the factor D(T) drops out. D(T) contains all the thermodynamic quantities needed for a complete comparison of data and theory, and it also contains a good deal of experimental error (in particular, ξ_0 and γ in the correlation length expression are difficult to determine). Cannell and Sarid used the (approximate) solutions for $Re[b_c(\omega)]$ and $Im[b_c(\omega)]$[19]:

$$\omega\, Im[b_c(\omega)] = V^2(\omega)\ \frac{1-(\bar{\alpha}_\lambda^c)^2}{1+(\bar{\alpha}_\lambda^c)^2} - V_0^2 \qquad 5.13$$

$$\bar{\alpha}_\lambda^c = \alpha_\lambda^c/(2\pi) \qquad \omega\, Re[b_c(\omega)] = 2\bar{\alpha}_\lambda^c V^2(\omega)/(1+(\bar{\alpha}_\lambda^c)^2)^2 \qquad 5.14$$

to test Kawasaki's formulation. Thus, only quantities directly obtainable from Brillouin scattering are used in this test, and compared with the principal results of the theory, the integrals $J(\omega^*)$ and $I(\omega^*)$. No other auxiliary parameters, other than the very accurate zero frequency sound velocity measurements, are needed.

$$\frac{J(\omega^*)}{I(\omega^*)} = \frac{1-(\bar{\alpha}_\lambda^c)^2}{2\bar{\alpha}_\lambda^c} - \left(\frac{V_0}{V(\omega)}\right)^2 \frac{(1+(\bar{\alpha}_\lambda^c)^2)^2}{2\bar{\alpha}_\lambda^c} = R_K \quad 5.15$$

Similarly, in terms of Mistura's complex specific heat, $\Delta(\omega)$,[19]

$$(1-1/\gamma)\, V_0^2\, Re[\Delta(\omega)]/C_V = -D(T)\, J(\omega^*) \quad 5.16$$

$$(1-1/\gamma)\, V_0^2\, Im[\Delta(\omega)]/C_V = D(T)\, I(\omega^*) \quad 5.17$$

the following ratio may be formed:

$$-\frac{J(\omega^*)}{I(\omega^*)} = \frac{Re[\Delta(\omega)]}{Im[\Delta(\omega)]} \quad 5.18$$

Using the (approximate) solutions:[19]

$$Im[\Delta(\omega)]/C_V = \frac{2\bar{\alpha}_\lambda^c V_0^2 V^2(\omega)(1-1/\gamma)}{(V^2(\omega)-V_0^2/\gamma)^2} \quad 5.19$$

$$Re[\Delta(\omega)]/C_V = \frac{V_0^2 - V^2(\omega)}{V^2(\omega)-V_0^2/\gamma} \qquad \gamma = \frac{C_p}{C_V} \quad 5.20$$

obtain:

$$-\frac{J(\omega^*)}{I(\omega^*)} = \left(\frac{1}{V^2(\omega)} - \frac{1}{V_0^2}\right) \frac{V^2(\omega)-V_0^2/\gamma}{2\bar{\alpha}_\lambda^c (1-1/\gamma)} = R_M \quad 5.21$$

Mistura's formulation is not quite as convenient to test since the heat ratio is an extra parameter, but γ is very well known from a variety of sources.[3] Note that for $\lambda^\beta = 0$, different forms for the correlation function may be used for the ratio J/I as before.

The results of this analysis applied to the present data are shown in figs. 5.5 and 5.6. For R_M, γ was determined from the quantities in Appendix C. There is little difference between the Kawasaki and Mistura forms on the basis of this ratio test; both are equally bad descriptions. R_M, R_K are mostly between -3 and +5 (negative dispersion is responsible

Figure 5.5: Ratio test - complex viscosity. R_K vs. $\log \omega^*$.
Data are plotted as $R_K = \frac{1-(\alpha_\lambda)^2}{2\alpha_\lambda} - \left(\frac{V_o}{V(\omega)}\right)^2 \frac{2((1+(\alpha_\lambda^c)^2)^2}{2\alpha_\lambda^c}$.
Curves are $J(\omega^*)/I(\omega^*)$. Symbols same as fig. 5.3.

RATIO TEST: COMPLEX VISCOSITY

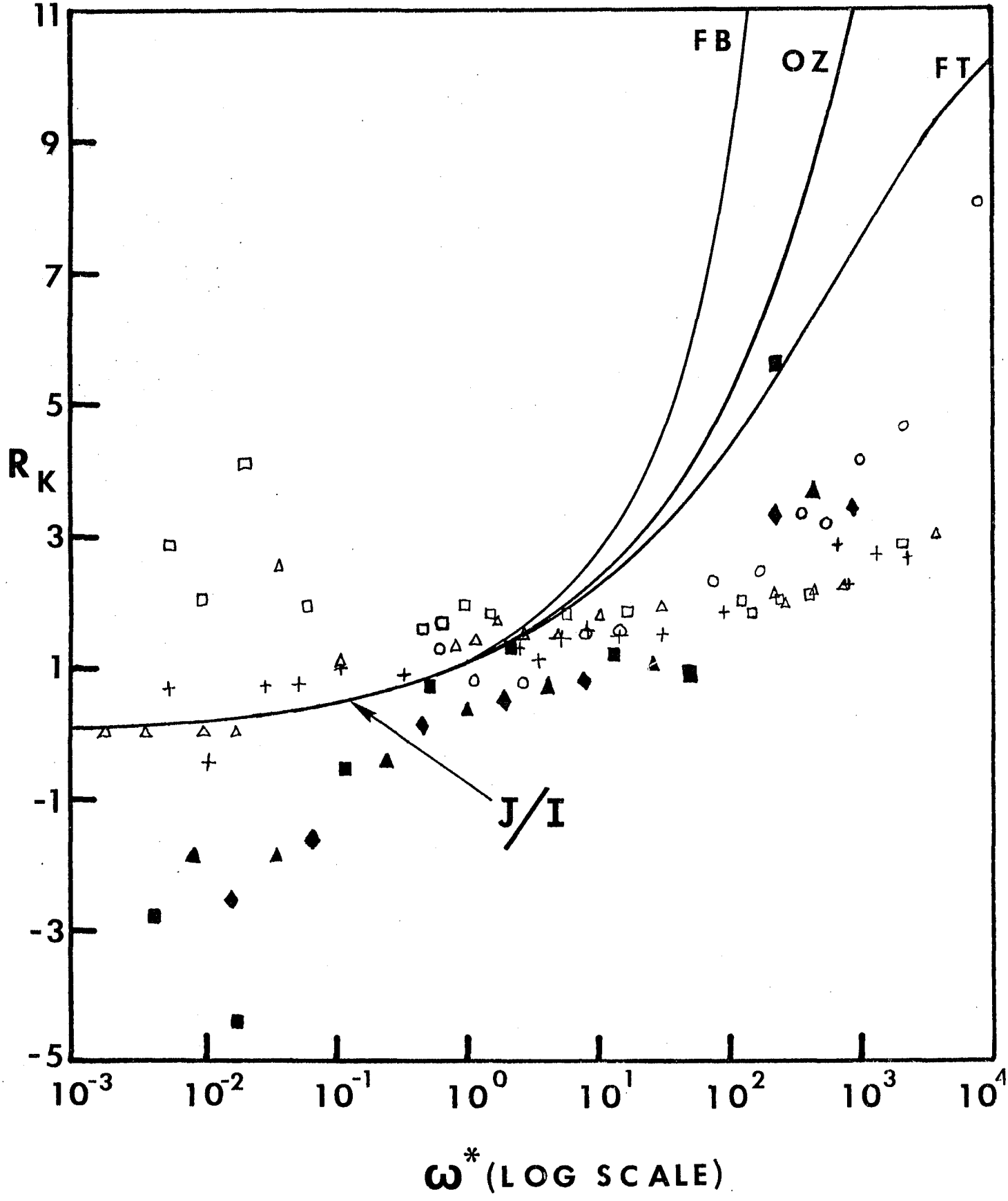

Figure 5.6: Ratio test - complex heat ratio. R_M vs. $\log \omega^*$.
Data are plotted as $R_M = -\left(\frac{1}{V^2(\omega)} - \frac{1}{V_0^2}\right) \frac{V^2(\omega) - V_0^2/\gamma^1}{2\alpha_\lambda^c (1 - 1/\gamma)}$.
Curves are $J(\omega^*)/I(\omega^*)$. Symbols same as fig.5.3.

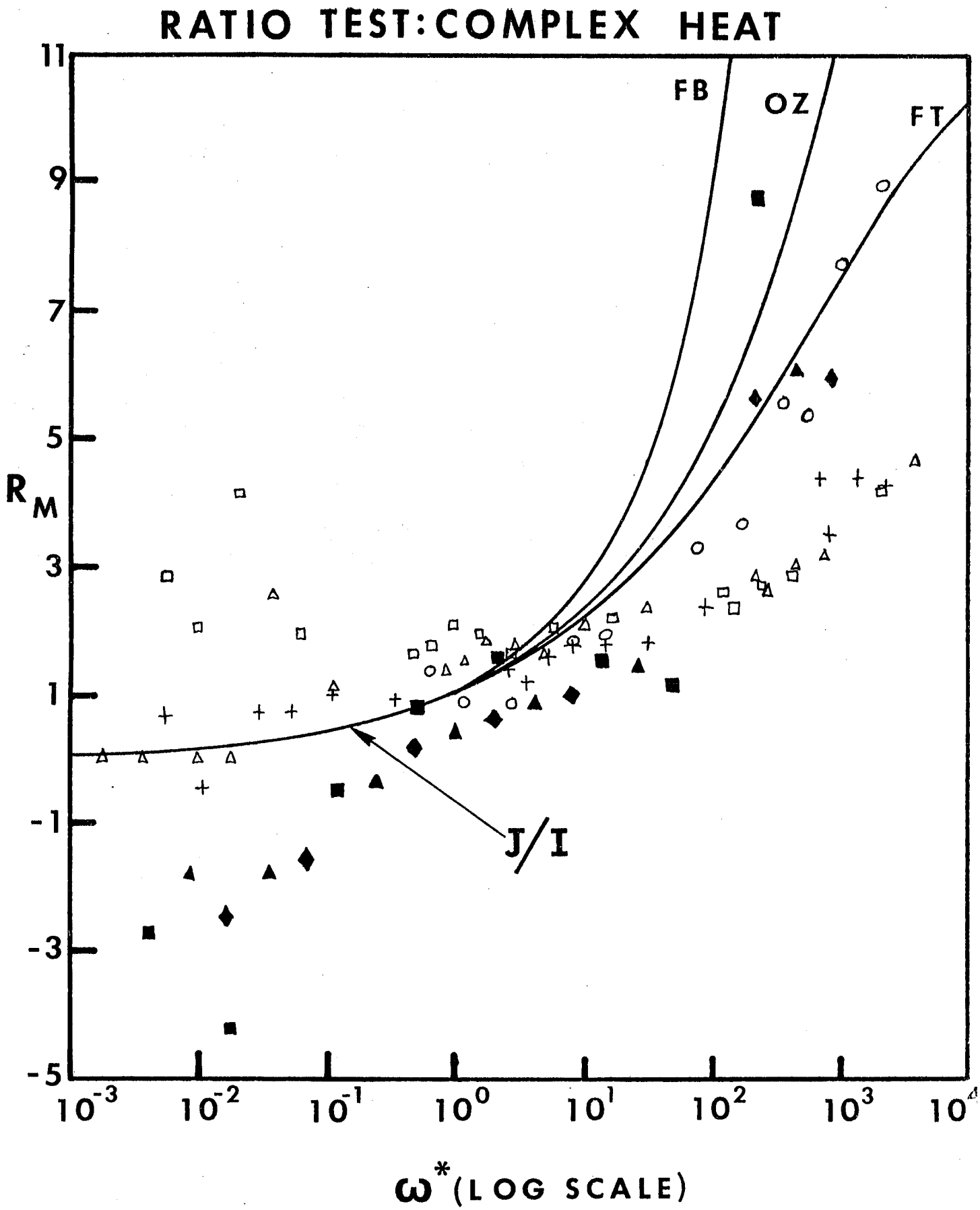
RATIO TEST: COMPLEX HEAT
FB
OZ
FT
J/I
R_M
11
9
7
5
3
1
-1
-3
-5
10^{-3}
10^{-2}
10^{-1}
10^{0}
10^{1}
10^{2}
10^{3}
ω^* (LOG SCALE)

for negative ratios). Overall, J/I does not agree with either R_M or R_K for any g(x); all J/I monotonically increase rapidly away from the data for $\omega^*>10$. The best agreement is near $\omega^*\sim 1$. Note that three high ω^* points of the present experiment lie closer to J/I for FT. For these three, the per cent differences between J/I and (R_M, R_K), relative to J/I, are: $\omega^*=228$ (-4.7%, 38%), $\omega^*=466$ (4.7%, 42%), $\omega^*=900$ (19%, 54%). Cannell's data also agree better for R_M (FT) in the region $\omega^*>200$.

Sarid & Cannell found that neither OZ nor FL agreed with the data when analyzed in terms of the viscosity ratio, but concluded from the heat ratio that the data were well fitted by FL. On the basis of these ratio tests compared to the present data, it must be concluded that neither the Kawasaki nor Mistura formulations describe the data at all well for any form of g(x). Contrary to Sarid & Cannell's conclusion, Mistura's formulation is not noticeably better than Kawasaki's. Though they made this conclusion on the basis of FL, and FL is not explicitly displayed here, FL will fall between the OZ and FT results depending on the many parameters involved in it.

In addition, Sarid & Cannell tested the dispersion and attenuation data separately for both a complex viscosity and complex heat, using for D(T) the same parameters used in the present experiment for F(T). They concluded that neither Kawasaki's nor Mistura's formulations described the reduced attenuation and reduced dispersion. The results of the present experiment agree with these conclusions, especially if the lowest scattering angle data are ignored.

For the reduced attenuation, all data lie above $I(\omega^*)$ for FT, OZ, and FB even for ω^* as small as 0.01, and great departure is shown for $\omega^* \geq 1$. For the reduced dispersion, the data agree with the theories up to $\omega^* \sim 1$ - 10 but show systematic departure for $\omega^* \geq 10$. In Sarid & Cannell's analyses, even though the Kawasaki and Mistura formulations are treated as being distinct and analyzed separately, the same departures are shown at about the same values of ω^* in the separate comparisons. They also show that there is good agreement between ultrasonic data at 1 and 3 MHz, and Brillouin data at 500 MHz, so that the differences in experimental methods do not seem relevant.

One might argue the validity of the approximations used in determining equations 5.15 and 5.21. In 5.15, the thermal diffusivity a ($=\lambda / \rho C_V$) was neglected compared to $b(\omega)$ in the dispersion equation:[19]

$$\omega^2/q^2 = V_0^2 + a\,b(\omega)\,q^2 - i\omega\left(a + b(\omega) - V_0^2\, a\, q^2/\gamma\omega^2\right)$$

This approximation is certainly true for the experiments in question. In obtaining 5.21, the dispersion equation:[19]

$$\frac{\omega^2}{q^2} = V_0^2 \left(\frac{1 + \Delta/C_\rho}{1 + \Delta/C_V} \right)$$

was used with the assumptions of $\gamma \neq 1$ and $(\bar{\alpha}_\lambda^c)^2 < 1$, also valid. It should be noted that $(\bar{\alpha}_\lambda^c)^2 < 1$, and $v(\omega) = v_o$ used in the Sarid-Cannell expressions for $J(\omega^*)$ and $I(\omega^*)$ reduce their equations to the same expressions given by Kawasaki, and Mistura, Garland, et al (indeed, these same approximations are used by the latter). Additionally, these

approximations should become better as T_c is approached, which for this experiment means higher ω^*; but, the largest departures from theory occur at high ω^*. Thus, it must be concluded that the approximations used are self consistent and adequate over the range of parameters studied.

F Summary & Conclusions

Brillouin sound propagation data in xenon on the critical isochore were compared to the critical fluid theories of Kawasaki and Mistura. The reduced dispersion, D, and reduced attenuation, A, were compared to the integrals J (ω^*) and I(ω^*) respectively, which included the dependence of these expressions on the form of the density-density correlation function, g(x). The Ornstein-Zernike, Fisher-Burford, and exact Fourier transform forms were considered for g(x).

It was found that the dispersion D is described well by J(ω^*) for $10^{-3} < \omega^* < 10^1$. For $\omega^* > 10$, D is systematically larger than J for all forms of g considered. In the high frequency regime, $100 < \omega^* < 1000$, D is 2-3 times larger than J. The attenuation, A, is described fairly well by I(ω^*) for $10^{-3} < \omega^* < 2$, but A is always larger than I even at these low frequencies. Beginning at $\omega^* \sim 2$, there is marked departure, with a maximum in A occurring near $\omega^* \sim 100$ followed by a decrease in A in the region $100 < \omega^* < 1000$. A is as much as 5 to 10 times larger than I in the high frequency region for all g.

In all previous tests, except that of Sarid & Cannell, departures of D and A at large ω^* were thought to be due to

1) experimental inaccuracies in the thermodynamic quantities in F(T) which appears as a scale factor in both J and I, and

2) the expected failure of the Ornstein-Zernike form to describe the correlation function near T_c . These previous tests allowed various forms for g, but the inaccuracy in F(T) was treated by least squares fitting of low ω^* data to adjust the parameters in F(T), and scaling the high frequency data accordingly. This procedure implicitly assumes the correctness of the theory in the low frequency regime. Agreement between theory and experiment was found, not surprisingly, in the low ω^* region, but the data departed to higher values than expected in the high frequency regime when the OZ correlation function was used. This departure was attributed to the inadequacy of OZ and workers found better agreement when the Fisher-Langer function was used.

The present experiment made use of the existing experimental values for the quantities in F(T) without parameter adjustment. These parameters, from a variety of sources, are known better for xenon on the critical isochore than for any other critical system at the present time. It is believed here that a fair comparison with theory can be made. It was found, in agreement with these previous tests, that J and I described D and A well in the low frequency regime, but that departures occur beginning at slightly lower ω^* and are much larger than thought previously. More importantly,

departure is independent of the correlation function form; no form tested was adequate. Since the data fall on a single (unknown) curve, it must be concluded that the dependence of sound propagation on the single relaxation frequency ω_R is correct.

Two additional tests were made. The ratio J/I for various g was compared to the ratios: Im $b(\omega)$/Re $b(\omega)$ for the Kawasaki formulation, and Re $\Delta(\omega)$/Im $\Delta(\omega)$ for the Mistura formulation. This test was used by Sarid & Cannell and they attempted to distinguish differences between the formulations as well as possible dependence on g. From these tests, neither the Kawasaki nor Mistura formulation agrees with the ratio of the respective data for any g over the whole range $10^{-3} < \omega^* < 10^4$. As a function of ω^*, the ratios are erratic, both at high and low ω^*, while J/I monotonically increases away from the data to higher values for all g. When analyzed in this manner, it must be concluded that neither formulation is correct and that the form of g does not improve the fit. The failure of the theory in this test is quite dramatic when it is noted that the factor F(T) is eliminated by taking the ratio J/I, and that the data ratio involves only directly measureable quantities in the experiment in the Kawasaki formulation, and direct experimental values and accurately known v_0 and γ' in the Mistura formulation. These results agree with Sarid & Cannell with the exception that Mistura's formulation is not substantially better than Kawasaki's for any g considered.

It should be noted that the ratio test alone is not a strictly fair comparison. If either J or I is incorrect, then so is their ratio. But, in conjunction with the testing of J and I separately, the ratio test supports the view that there is a more fundamental inadequacy of the theory than thought previously, and that this inadequacy cannot simply be attributed to a failure in the Ornstein Zernike formulation for the correlation function.

References for Chapter V

1. P.E.Mueller, D.Eden, C.W. Garland and R.C. Williamson, Phys. Rev. A 6, 2272

2. H.L.Swinney, in Photon Correlation and Light Beating Spectroscopy, ed. by H.Z.Cummins and E.R.Pike (Plenum, New York,1974), p.366.

3. H.L.Swinney and D.L.Henry, Phys. Rev.A 8, 2586 (1973).

4. Ref. 2, p.368.

5. C.Garland and R.Williams, Phys. Rev. A 10,1328 (1974).

6. H.Z.Cummins and H.L.Swinney, Phys. Rev.Lett. 25,1165 (1970).

7. Ref. 2,p.367-368.

8. P.Tartaglia and J.Thoen, Phys. Rev. A 11, 2061 (1975).

9. M.E.Fisher, J.Math. Phys. 5,944 (1964).

10. M.E.Fisher and R.J.Burford, Phys. Rev.156,583 (1967). M.E.Fisher and D.S.Ritchie, Phys. Rev.B 5, 2668 (1972).

11. M.E.Fisher and J.S.Langer, Phys. Rev. Lett. 20,665 (1968).

12. V.I.Krylov, Approximate Calculation of Integrals, p.129 (MacMillan, New York, 1962).

13. C.Garland, D.Eden and L.Mistura, Phys. Rev. Lett.25, 1161 (1970).

14. D.Eden, C.Garland and J.Thoen, Phys. Rev. Lett. 28,726 (1972).

15. J. Thoen and C. Garland, Phys. Rev. A 10, 1311 (1974).

16. D.S.Cannell and G.B.Benedek, Phys. Rev. Lett. 25, 1157 (1978).

17. P. Schofield, J.D.Litster and J.T.Ho, Phys.Rev.Lett. 23,1098 (1969).

18. D. Eden and H.L.Swinney, Opt. Commun. 10,191 (1974).

19. D.Sarid and D.S.Cannell, Phys. Rev. A 15, 735 (1977).

APPENDIX A

CORRECTED SCATTERING ANGLES

Angle (air)	Angle (xenon)	Radius (cm)
.36011°	.31672°	.408305
.71851°	.63193°	.814704
1.43512°	1.26216°	1.627500
2.68797°	2.36389°	3.049905

angle (air) = TAN^{-1}(Radius/EFL) EFL = 649.6 mm

angle (xenon) = SIN^{-1}(SIN(angle, air)/n(xenon))

n(xenon) = 1.1366 @ 4880 Å

APPENDIX B

DATA

$\Theta = 0.36011^{o}$

$\Delta T(^{o}K)$	ν_B(MHz)	Γ_B(kHz)	V(m/s)	α_λ^{Crit}	α_λ^{Back}
.05	0.945	119.95	73.37	.7966	.0010
	1.005	166.69	78.03	1.0411	.0010
	0.926	149.98	71.90	1.0167	.0009
.10	1.296	-	100.62	-	-
	1.270	-	98.60	-	-
	0.928	113.09	72.05	.7649	.0008
	0.912	107.85	70.81	.7423	.0008
.20	1.198	-	93.01	-	-
	1.120	109.81	86.96	.6024	.0003
	1.326	-	102.95	-	-
	1.420	-	110.25	-	-
.50	1.701	58.76	132.07	.2162	.0008
	1.702	62.88	132.15	.2313	.0008
	1.304	204.20	101.24	.9833	.0006
	1.279	160.59	99.30	.7883	.0006
1.00	1.472	46.73	114.29	.1989	.0006
	1.402	32.69	108.85	.1459	.0006
2.00	1.438	13.96	111.65	.0605	.0005
	1.378	12.14	106.99	.0549	.0005

$\Theta = 0.71851^{o}$

$\Delta T(^{o}K)$	ν_B(MHz)	Γ_B(kHz)	V(m/s)	α_λ^{Crit}	α_λ^{Back}
.05	2.544	73.06	99.02	.1779	.0026
	2.649	83.05	103.09	.1943	.0027
	2.625	98.48	102.15	.2331	.0027
.10	2.262	250.19	88.03	.6931	.0019
	2.031	112.17	79.04	.3453	.0017
	2.603	56.31	101.30	.1338	.0022
.20	2.623	239.43	102.07	.5718	.0017
	2.515	92.01	97.87	.2282	.0016
	2.492	198.59	96.98	.4991	.0016
.50	2.773	107.22	107.91	.2416	.0013
	2.798	124.21	108.89	.2776	.0014
	2.631	195.97	102.39	.4667	.0013
1.00	2.792	85.62	108.65	.1916	.0011
	2.773	108.36	107.91	.2444	.0011
	2.884	79.16	112.23	.1713	.0011
	2.859	90.05	111.26	.1904	.0011
	2.678	90.80	104.22	.1994	.0011
2.00	2.950	47.44	114.80	.1001	.0010
	2.927	40.96	113.91	.0870	.0010
5.00	3.418	8.31	133.01	.0144	.0009
	3.135	13.59	122.00	.0264	.0008
	3.257	16.24	126.75	.0305	.0008
	3.274	20.08	127.41	.0377	.0008
10.00	3.560	6.65	138.54	.0110	.0008
	3.703	15.41	144.11	.0254	.0008

$\Theta = 1.43512^{o}$

$\Delta T(^{o}K)$	ν_B(MHz)	Γ_B(kHz)	V(m/s)	α_λ^{Crit}	α_λ^{Back}
.05	5.307	279.20	103.40	.3252	.0054
	5.286	269.45	102.99	.3149	.0053
.10	5.029	695.07	97.98	.8642	.0042
	5.167	293.82	100.67	.3530	.0043
	5.009	884.57	97.59	1.1054	.0042
.20	5.210	206.73	101.51	.2459	.0034
	5.066	318.28	98.71	.3915	.0033
	5.093	742.42	99.23	.9126	.0033
	5.151	393.92	100.36	.4772	.0033
.50	5.347	241.87	104.18	.2816	.0026
	5.321	279.63	103.67	.3276	.0026
	5.341	346.93	104.06	.4056	.0026
	5.314	290.88	103.54	.3414	.0026
	5.324	364.50	103.73	.4276	.0026
	5.342	412.98	104.08	.4832	.0026
1.00	5.528	216.66	107.71	.2441	.0022
	5.447	192.53	106.13	.2200	.0022
	5.605	157.81	109.21	.1747	.0022
	5.538	124.00	107.90	.1385	.0022
2.00	5.826	119.54	113.51	.1270	.0019
	5.920	121.32	115.34	.1269	.0019
5.00	6.547	49.61	127.56	.0460	.0017
	6.562	46.64	127.85	.0422	.0017
	6.515	67.64	126.94	.0636	.0017
	6.579	75.49	128.18	.0704	.0017
10.00	7.291	25.49	142.06	.0204	.0016
	7.261	24.63	141.47	.0198	.0016
	7.151	31.90	139.33	.0265	.0016
	7.331	42.26	142.84	.0340	.0016

$\Theta = 2.68797^{o}$

$\Delta T(^{o}K)$	ν_B(MHz)	Γ_B(kHz)	V(m/s)	α_λ^{Crit}	α_λ^{Back}
.05	10.277	681.30	106.92	.4062	.0104
	10.190	589.69	106.01	.3533	.0103
.10	10.380	944.75	107.99	.5633	.0086
	10.360	302.97	107.78	.1751	.0086
.50	10.120	534.30	105.28	.3269	.0048
	10.041	421.80	104.46	.2591	.0048
	9.892	816.24	102.91	.5137	.0048
1.00	10.494	407.59	109.18	.2399	.0041
	10.363	402.22	107.81	.2398	.0041
	10.559	388.97	109.85	.2273	.0042
	10.363	521.35	107.81	.3120	.0041
	10.515	486.52	109.39	.2866	.0041
	10.565	450.07	109.91	.2635	.0042
2.00	11.116	265.63	115.65	.1465	.0036
	11.040	285.34	114.85	.1588	.0036
	11.228	187.74	116.81	.1014	.0036
	11.164	249.15	116.15	.1366	.0036
	11.033	255.89	114.78	.1422	.0036
5.00	12.414	106.69	129.15	.0509	.0032
	12.163	97.60	126.54	.0473	.0031
	12.334	98.21	128.32	.0469	.0031
	12.308	99.38	128.05	.0476	.0031
	12.293	142.95	127.89	.0700	.0031
10.00	13.588	70.14	141.36	.0295	.0029
	13.575	61.80	141.23	.0257	.0029
	13.595	43.00	141.44	.0170	.0029

APPENDIX C

AUXILIARY THERMODYNAMIC QUANTITIES FOR α_λ^B, F(T), ω^*

$$\alpha_\lambda^B = \frac{\pi\omega}{V_o^2}\left[\frac{4/3\eta_s+\zeta}{\rho} + \frac{\lambda}{\rho}(1/C_v - 1/C_p)\right]$$

$$F(T) = \frac{k_B T^2}{2\pi^2 \rho C_v \xi}(1 - C_v/C_p)(\partial \xi^{-1}/\partial T)_s^2$$

$$\omega^* = \omega/(2\omega_R) \qquad \omega_R = \lambda/(\rho C_p \xi^2)$$

With $\zeta^B \approx \eta_s^B$, α_λ^B may be written as:

$$\alpha_\lambda^B = \frac{\pi\omega}{V_o^2}\left[\frac{7/3\,\eta_s^B}{\rho} + \frac{\lambda^B+\lambda^c}{\rho\, c_p}\left(c_p/c_v - 1\right)\right]$$

Now the terms involving the specific heats are:

$$\rho C_p = \rho C_v + T(\partial P/\partial T)^2 K_T$$

with

$$K_T = (\Gamma_T/P_c)\epsilon^{-\gamma} \qquad \epsilon = (T - T_c)/T_c$$

and

$$(P - P_c)/P_c = c_1\epsilon + P_1^+\epsilon^{2-\alpha} + \rho_c H_2^+ \epsilon^{3-2\alpha-2\beta}$$

Therefore,

$$(\partial P/\partial T)^2_{\rho=\rho_c} = (P_c/T_c)^2 (c_1 + P_1^+(2-\alpha)\epsilon^{1-\alpha} + \rho_c H_2^+(3-2\alpha-2\beta) \times \epsilon^{2(1-\alpha-\beta)}).$$

Now

$$\rho_c C_v = (2.2922\,\epsilon^{-.146} - 1.6928) \times 10^6 \text{ erg cm}^{-3} \text{ K}^{-1}$$

and

$$\Gamma_T = 0.06778$$

$$P_c = 58.402 \times 10^6 \text{ dyne cm}^{-2}$$

$$\gamma = 1.21$$

so that $K_T = 1.160577 \times 10^{-9}\ ^{-1.21}$ cm^{2}dyne^{-1}.

The constants in the pressure derivative term are:

$$c_1 = 5.925384$$

$$P_1^+ = 2.635562$$

$$\rho_c H_2^+ = -2.616886$$

$$\alpha = 0.08$$

$$\beta = 0.35$$

$$T_c = 289.77^{\circ}K \text{ (measured, present experiment).}$$

Therefore,

$$(\partial P/\partial T)^2_{\rho=\rho_c} = (5.925384 + 5.060279\,\epsilon^{.92} - 5.600136\,\epsilon^{1.14})^2 \times 4.062081 \times 10^{10} \text{ dyne}^2 \text{ cm}^{-4} \text{ K}^{-2}$$

and

$$\rho_c C_p = \rho_c C_v + T\epsilon^{-1.21}(47.1436)(5.925384 + 5.060279\epsilon^{.92} - 5.600136\epsilon^{1.14})^2 \text{ erg cm}^{-3} \text{ K}^{-1}.$$

Examining now the conductivity,

$$\lambda^B = \lambda(0,T) + \tilde{\lambda}(\rho)$$

$$\lambda(0,T) = (544 + 522\epsilon) \text{ erg cm}^{-1} \text{ s}^{-1} \text{ K}^{-1}$$

$$\tilde{\lambda}(\rho) = 590.5 + 381.7\rho^2 - 107\rho^3 + 50.04\rho^4$$

$$\tilde{\lambda}(\rho=\rho_c) = 1.069038 \times 10^3 \text{ erg cm}^{-1} \text{ s}^{-1} \text{ K}^{-1}$$

Therefore,

$$\lambda^{\beta} = (1.613038 \times 10^3 + 522\epsilon) \text{ erg cm}^{-1} \text{ s}^{-1} \text{ K}^{-1}.$$

$$\lambda^c = k_B T/(6\pi\eta_s q^2 \xi^3)\, K_0(q\xi)\rho_c C_p^c$$

$$K_0(x) = .75(1 + x^2 + (x^3 - 1/x)\text{Tan}^{-1}x)$$

$$\xi = \xi_0\, \epsilon^{-\nu} = 2 \times 10^{-8} \epsilon^{-.63} \text{ cm}$$

$$C_p^c = 4.321016 \times 10^5 \epsilon^{-1.21} \text{ erg cm}^{-1} \text{ K}^{-1}$$

$$\eta_s = \eta_s^B + \eta_s^C$$

$$\eta_s^B = (525 + 219\epsilon) \times 10^{-6} \text{ Poise}$$

$$\eta_s^C = -(16.35 \ln\epsilon + 68.66) \times 10^{-6} \text{ Poise}$$

$$k_B = 1.381 \times 10^{-16} \text{ erg K}^{-1}$$

$\rho_c = 1.11$ gm cm^{-3}

$q = (4\pi n \sin(\theta/2))/\lambda_o$

$\lambda_o = 4880 \times 10^{-8}$ cm

$n = 1.137$ @ 4880 Å

The values of V_0 are found in the following appendix.

In F(T), the correlation length derivative term is:

$(\partial \xi^{-1}/\partial T)_s^2 = ((\nu/(\xi_o T_c))\epsilon^{\nu-1})^2$ cm^{-2} K^{-2}.

In ω^*, $\lambda = \lambda^c + \lambda^B$, and the terms are given above.

The values for the above quantities were taken from Table III of the paper of Swinney and Henry.*

* H.L Swinney and D.L. Henry, Phys. Rev. A 8, 2586 (1973).

Figure C.1: Thermodynamic factor F(T).

$$F(T) = \frac{k_B T^2}{2\pi^2 \rho C_v \xi} (1 - C_v/C_p) (\partial \xi^{-1}/\partial T)_s^2$$

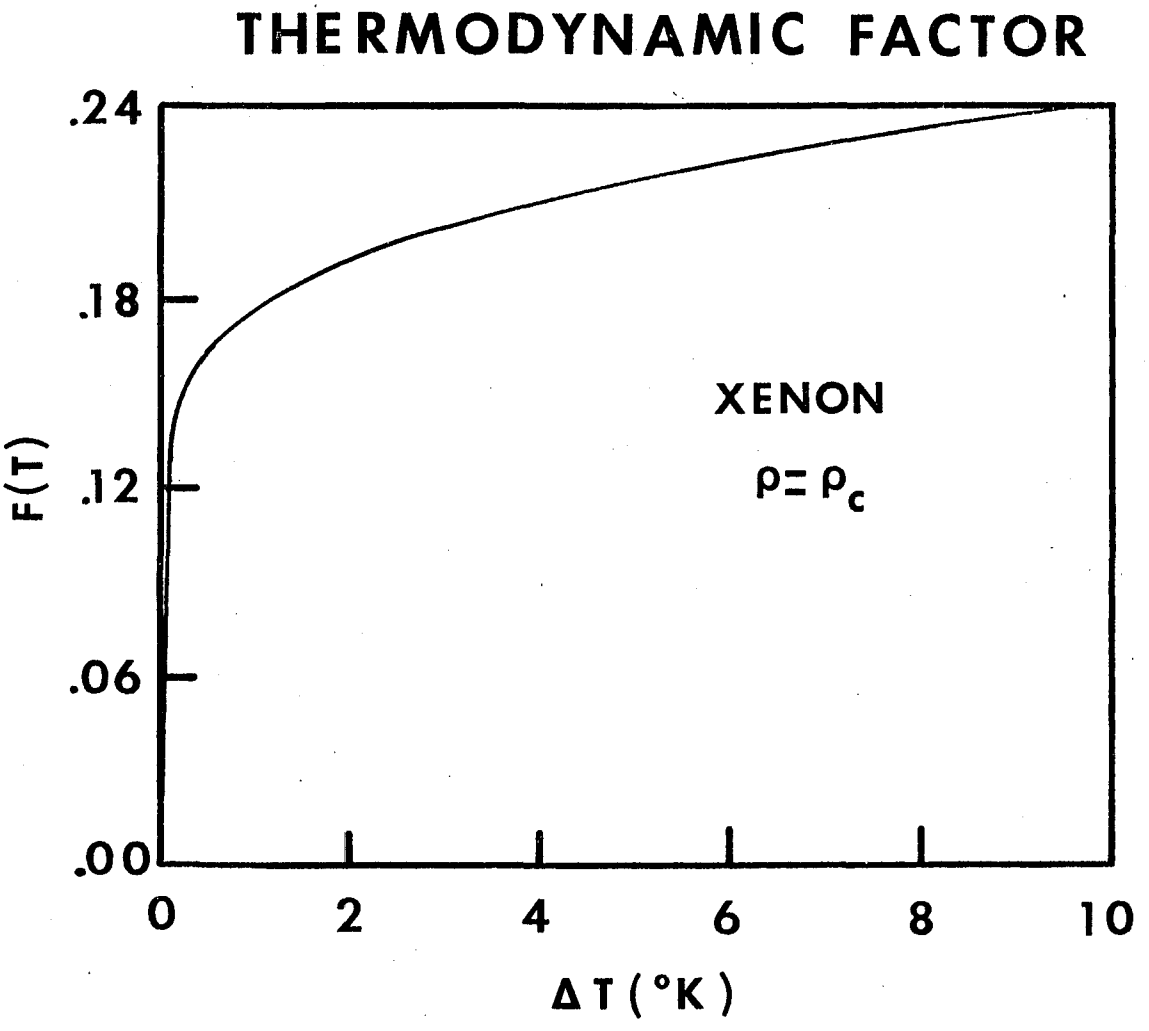
THERMODYNAMIC FACTOR
.24
.18
.12
.06
.00
F(T)
XENON
ρ= ρc
0
2
4
6
8
10
ΔT (°K)

APPENDIX D

ZERO FREQUENCY SOUND VELOCITY

The zero frequency sound velocity was determined from ultrasonic measurements by quadratic interpolation of three values of ΔT nearest to those of the present experiment. For $\Delta T = 2^{o}$, 1^{o}, 0.5^{o}, 0.2^{o}, 0.1^{o} and $0.05^{o}K$, the 1 kHz graphical presentation of the data of Garland and Williams* was used, and for $\Delta T = 10^{o}$ and $5^{o}K$, the 1 MHz data of Mueller et al** were used.

* C. Garland and R. Williams, Phys. Rev. A 10, 1328 (1974).

** P.E. Mueller, D. Eden, C.W. Garland and R.C. Williamson, Phys. Rev. A 6, 2272 (1972).

Ultrasonic Data

ΔT (^{o}K)	V(m/s)
14.782	151.48
9.782	141.99
7.282	136.15
7.282	136.15
4.782	128.95
3.782	125.17
2.23	116.8
2.08	115.8
1.91	114.7
1.17	108.2
1.10	107.5
0.95	105.7
0.56	100.0
0.52	99.2
0.45	97.4
0.25	92.3
0.22	90.8
0.18	89.3

Interpolated Values for Brillouin Experiment

ΔT (^{o}K)	V_0(m/s)
10	142.47
5	129.71
2	115.28
1	106.35
0.5	98.74
0.2	89.98
0.1	83.8
0.05	81.2

APPENDIX E

REDUCED DISPERSION, REDUCED ATTENUATION, ω^*

$\Delta T(^oK)$	Θ (deg.)	ω^*	D	A
0.05	0.72	229.2	1.904	.2456
	1.44	465.8	2.072	.3896
	2.69	899.8	2.380	.4622
0.10	0.72	50.56	0.481	.4481
	1.44	111.5	1.285	.8878
	2.69	228.1	2.071	.4234
0.20	0.72	13.72	.6760	.4660
	1.44	27.71	.7493	.5454
0.50	0.72	2.221	.4785	.3228
	1.44	4.336	.3220	.3711
	2.69	8.148	.3425	.3601
1.00	0.72	.5221	.1353	.1715
	1.44	1.041	.0751	.1770
	2.69	1.973	.1427	.2382
2.00	0.72	.1237	-.0423	.0784
	1.44	.2484	-.0389	.1064
	2.69	.4707	.0168	.1149
5.00	0.72	.0182	-.0865	.0202
	1.44	.0372	-.0743	.0411
	2.69	.0698	-.0616	.0389
10.00	0.72	.0042	-.0334	.0120
	1.44	.0089	-.0305	.0167
	2.69	.0167	-.0328	.0160